DYNAMICS AND CONTROL OF RIDER-BICYCLE SYSTEMS

By

PENGCHENG WANG

A dissertation submitted to the

School of Graduate Studies

Rutgers, The State University of New Jersey

in partial fulfillment of the requirements

For the degree of

Doctor of Philosophy

Graduate Program in Mechanical and Aerospace Engineering

Written under the direction of

Dr. Jingang Yi

And approved by

_____

_____

_____

_____

New Brunswick, New Jersey

October, 2018

ABSTRACT OF THE DISSERTATION

Dynamics and Control of Rider-Bicycle Systems

By PENGCHENG WANG

Dissertation Director:

Dr. Jingang Yi

How can an autonomous bicycle robot system keep balance and track a path? How does a human rider ride a bicycle? And how can we enhance human riding safety and efficiency? Answers of these questions can provide guidance for autonomous single-track vehicle control system design, understanding human riding skills and vehicle assistive design. Furthermore, riding a bicycle is an unstable physical human-machine interaction (upHMI). Riding skills analysis is a good example about understanding human control mechanism, including human body movement control and human neuro-control. The bicycle assisted balancing system also provides the inspiration for designing other human-robot cooperation system. This dissertation has three objectives: the first one is to design control system for autonomous bicycle for balancing and tracking; the second one is to model and analyze the human riding skills of balancing and tracking; and the last one is to design tuning method for human riding balancing skills.

The first part of this dissertation focuses on the autonomous bicycle control system design for balancing and path following. The bikebot, an autonomous bicycle system, is

designed for these control mechanism implementation. The gyro-balancer control law and steering motion control law are designed for balancing the bikebot system in the stationary and moving stages, respectively. Using these two control laws, a switching control strategy is proposed for a stationary-moving transition process. The control performances are demonstrated by the experimental results for a complete maneuver.

For the trajectory tracking tasks, the external/internal convertible (EIC) structure-based control strategies are proposed and implemented. The EIC-based control takes the advantages of the non-minimum phase underactuated dynamics structure. We first analyze and demonstrate the EIC-based motion tracking controller. An auxiliary gyro subsystem control law is then designed to enhance the tracking performance of the EIC-based controller. The errors dynamics and control properties are discussed and analyzed. Finally, the control strategies are implemented on the bikebot system. The experiments results confirm and demonstrate the controllers effectiveness.

The second part of the dissertation focuses on the analysis of human riding skills, including the balance control and the tracking skills. For the motion tracking with balancing motor skills, using the EIC structure, a balance equilibrium manifold (BEM) concept is proposed for analyzing the human trajectory tracking behaviors and balancing properties. The contributions of steering and upper-body motion are analyzed quantitatively. Finally, performance metrics are introduced to quantify the balance motor skills using the BEM concept. These analysis and discussions are demonstrated and validated by extensive human riding experiments. Comparison between the EIC-based control and human control is also presented and demonstrated.

For the balance skill studies, we first present the control models of human steering angle and upper-body leaning torque. These models are inspired by the human stance balance studies and built on several groups of human riding experiments. The parameters sensitivity analyses are also discussed with experiment validation. Using the time-delayed system stability analysis, the quantitative influences of the model parameters on closed-loop stability are also demonstrated and experimentally verified.

Based on aforementioned results, actively tuning the rider-bikebot interaction is the aim of the last part of the dissertation. First, from the rider-bikebot interaction dynamics, the stiffness and damping effect for balancing are analyzed. The control of the rider-bikebot interactions is designed to tune the stiffness and damping effects by reshaping the rider steering motion. From experiments observation, the rider balancing performances are significantly improved under the tuned interaction dynamics. Furthermore, under a special tuned stiffness and damping effect, the rider-bikebot system can be balanced autonomously without considering the rider steering input. This property is also theoretically proven and also verified by the experiments.

The outcomes of this dissertation not only advances the understanding the human rider balance motor skills but also provides the guidance for the autonomous bicycle control design, and the human balancing performance tuning method through rider-bikebot interactions. At the end of this dissertation, future work directions are also discussed and presented.

Acknowledgments

First of all, I would like to thank my Ph.D. advisor, Dr. Jingang Yi, for his valuable guidance through my entire Ph.D. study and research. Dr. Yi is a perfect example of a scholar and an engineer. It is him who leads me into the robotics field, shapes my skills for the future career path. Without his support, and guidance, I would not complete this dissertation.

Next I would like to express my sincere appreciation to Dr. Xiaoli Bai, Dr. Elizabeth Torres, and Dr. Qingze Zou for being my dissertation committee members and offering their constructive comments and suggestions for improvement of my research work.

Special acknowledgement goes to Prof. Yongchun Fang for introducing me to Rutgers, and his encouragement and guidance. Additionally, my appreciation goes to my group members and visiting scholars at Robotics, Automation and Mechatronics laboratory, including Yizhai Zhang, Kuo Chen, Yongbin Gong, Chaoke Guo, Fei Liu, Mitja Trkov, Kaiyan Yu, Haijun Han, Juanjuan Sun, Merrill Edmonds, Siyu Chen, Shanqiang Wu, Yingshu Liu, Hongbiao Xiang, and Lei Sun. I also would like to thank my friends and fellow students, Jiangbo Liu, Xiaodong Xia, Fei Ge, Zhong Chen, Hanxiong Wang, Wuhan Yuan, and Xiaobing Zhang. Their support, suggestion, and encouragement help me to complete my Ph.D. study.

Dedication

I dedicate my dissertation to my parents, Guoli Wang and Yanhui Liu.

Table of Contents

Abstract ii

Acknowledgments v

Dedication vi

List of Tables xi

List of Figures xii

1. Introduction 1

1.1. Motivation 1

1.2. Background 2

1.2.1. Autonomous bicycle systems 2

1.2.2. Human control mechanisms modeling and analysis 4

1.3. Dissertation outline and contributions 5

2. System Dynamics and Experiment System 10

2.1. Introduction 10

2.2. Bikebot system dynamics 11

2.3. Rider-bicycle system dynamics 14

2.4. Bikebot experiments system 16

2.5. Conclusion 18

3. Bikebot Autonomous Balancing Control 19

3.1. Introduction 19
3.2. Stationary balancing by gyro-balancer 22
3.2.1. Orbits construction 22
3.2.2. Orbital regulation controller design 25
3.3. Balancing control by steering actuation 26
3.4. Balance switching control laws 27
3.4.1. Balancing actuation capacity comparison 28
3.4.2. DOA Estimates 29
3.4.3. Switching Strategy 34
3.5. Experiments results 35
3.6. Conclusion 40

4. Bikebot Autonomous Tracking Control 41
4.1. Introduction 41
4.2. EIC-based controller design 43
4.3. Stability analysis 48
4.4. Experiments 51
4.4.1. Path following control 51
4.4.2. Trajectory tracking control 54
4.4.3. Gyro-balancer assistive control 56
4.5. Conclusion 59

5. Control Analysis for Human Tracking Riding 60
5.1. Introduction 60
5.2. Dynamics structure and BEM 63
5.3. Balancing by body movement and steering 65
5.4. Riding balance performance metrics 68
5.4.1. Stability analysis for EIC design 68

5.4.2. Riding performance metrics 70
5.5. Experiments 71
5.6. Conclusion 76

6. Control Analysis for Human Balancing Riding 77
6.1. Introduction 77
6.2. Human balance control models and stability analysis 80
6.2.1. Human balance control models 80
6.2.2. Rider-bicycle system stability 84
6.3. Experiments 85
6.3.1. Riding experiments design 85
6.3.2. Riding Performance Metrics 87
6.4. Results 88
6.4.1. Model validation results 88
6.4.2. Control models parameters analysis 91
6.4.3. Stability results 95
6.5. Discussions 97
6.6. Balancing stability under zero speed 103
6.7. Conclusion 106

7. Balance Performance Tuning of Rider-Bikebot Interactions 107
7.1. Introduction 107
7.2. Rider-bikebot interactions model 109
7.3. Control of rider-bikebot interactions 110
7.3.1. Controller design 110
7.3.2. Performance metrics and evaluation 113
7.4. Experimental results 114
7.4.1. Experiment setup 114

7.4.2. Experimental results 115
7.5. Conclusion 119

8. Conclusions and Future Work 120
8.1. Conclusions 120
8.2. Future work 123

References 125

List of Tables

4.1. The mean and standard deviation of $|e_p|_{ave}$(m) and $|e_\alpha|_{ave}$(deg) for the path following performances. 53

6.1. The mean and standard deviation of the human steering and upper-body movement model parameters. 90

6.2. Identified human upper-body movement and steering control time delays. . 91

7.1. Parameters configuration of interaction model 115

7.2. F-test for the balancing metrics under controllers $\mathcal{C}$ and $\mathcal{C}_a$ ($F_{0.05(1,4)} = 7.71$) 117

List of Figures

2.1. (a) The Rutgers bikebot system. (b) A kinematic schematic of the gyro-balanced bikebot system. 12

2.2. (a) Human riding experiment. (b) A kinematic schematic of the rider-bicycle system. 15

2.3. The Rutgers bikebot. 16

2.4. (a) Bikebot data onboard control system. (b) 6-DoFs IMU. 17

2.5. (a) Gyro-balancer part. (b) Autonomous steering part. 17

3.1. Gyro-balancer orbital regulation results. (a) Bikebot rolling trajectory on φ_b-$\dot{\varphi}_b$ phase plan. (b) Flywheel pivoting trajectory on φ_w-$\dot{\varphi}_w$ phase plan. (c) Bikebot roll angle φ_b trajectory. (d) Flywheel pivoting angle φ_w trajectory. 35

3.2. The DOA plots of the gyro-balancer and steering balance controls. (a) The DOA plots under gyro-balancer orbital regulation control u_w with initial condition $\varphi_{w0} = 0$ and various parameters. Blue: $m_b = 55$ kg, $\omega_s = 1500$ rpm, $h_b = 0.64$ m; Green: $m_b = 42$ kg, $\omega_s = 1500$ rpm, $h_b = 0.64$ m; Red: $m_b = 55$ kg, $\omega_s = 1200$ rpm, $h_b = 0.64$ m; Black: $m_b = 55$ kg, $\omega_s = 1200$ rpm, $h_b = 0.48$ m. (b) The DOA plots of the gyro-balancer control u_w and steering control u_s. (c) Plots of $\mathbf{\Omega}_w$ and $\mathbf{\Omega}_s$. Blue: boundary of $\mathbf{\Omega}_w$ at $m_b = 55$ kg and $\omega_s = 1500$ rpm; Green, red and black: boundaries of $\mathbf{\Omega}_s$ under $v_r = 0.75$ m/s, $v_r = 1.00$ m/s and $v_r = 1.50$ m/s. 36

3.3. Switched balance control results. (a) Bikebot roll angle φ_b and target roll angle φ_{be}. (Top-figure: blue and red curves under u_w and green curve under u_s; Bottom-figure: blue and red curves are the roll angle $\varphi_b(t)$ and the desired $\varphi_{be}(t)$, respectively. The solid and dash lines portion represent the only balancing and balancing-tracking,respectively. (b) Flywheel pivoting angle φ_w and steering angle ϕ. Blue and red portion under u_w control and the green portion under u_s control.) (c) Bikebot planar position (X, Y). Purple dash, blue solid, and black square portions are under u_w, u_s, and EIC-based velocity-steering control (u_v, u_s), respectively. The red dash line is the target path. (d) Bikebot velocity v_r and path following error e_P. For the top-figure, blue and red portion are under u_w and u_s controls, respectively. (e) State variable $(\varphi_b(t_{s2}), \dot{\varphi}_b(t_{s2}))$ on the φ_b-$\dot{\varphi}_b$ plane. Blue squares, red circles, red crosses marks are for the success, failure with $|I_I + I_D| \leq I_C$, failure with $|I_I + I_D| > I_C$ cases, respectively. The black lines are the boundary of $\mathbf{\Omega}_w$. (f) Running conditions in the I_I-I_D plane. Blue squares, red circles, and red crosses are for the success, failure with $|I_I + I_D| \leq I_C$, failure with $|I_I + I_D| > I_C$ cases, respectively. The black line represents $I_I + I_D = I_C$. 37

4.1. A nearly external/internal convertible system. 44

4.2. Bikebot path following results. (a), (b) and (c) Horizontal position results of Straight line, circle and '8'-figure. (Blue lines are the bikebot horizontal position, Red lines are the target paths.) (d), (e) and (f) Roll angle tracking results of Straight line, circle and '8'-figure. (Blue lines are the measured bikebot roll angle φ_b, Red lines are the target φ_{be} trajectories.) 52

4.3. Tracking results comparison between the regular EIC controller and modified EIC controller. (a) Position trajectories. (black dash, blue solid and red solid lines are the target trajectory, real trajectory under modified EIC control and real trajectory under regular EIC control.) (b) Position tracking error. (c) Position Tracking errors in X- and Y- directions. (d) Bikebot real velocities under these two controllers. (e) time suspension rate in modified EIC control. (f) Roll angle tracking results. (Upper figure is for the modified EIC control, lower figure is for the original EIC control)) 55

4.4. Performance comparison of the two controllers $\mathcal{C}$ and $\overline{\mathcal{C}}$ to follow a straight-line. (The solid circular dot indicates the starting location.) 57

4.5. Performance comparison of the two controllers $\mathcal{C}$ and $\overline{\mathcal{C}}$ to follow a straight-line. (a) Tracking errors. (b) Balancing roll angles. 57

4.6. Performance comparison of the two controllers $\mathcal{C}$ and $\overline{\mathcal{C}}$ to follow a straight-line. (a) Controller inputs under $\overline{\mathcal{C}}$. (b) Controller inputs under $\mathcal{C}$. 57

4.7. Performance comparison of the two controllers $\mathcal{C}$ and $\overline{\mathcal{C}}$ to follow a circular trajectory. (a) The tracking trajectory under $\overline{\mathcal{C}}$. (b) The tracking trajectory under $\mathcal{C}$. The solid circular dots indicate the starting locations in (a) and (b). 58

4.8. Performance comparison of the two controllers $\mathcal{C}$ and $\overline{\mathcal{C}}$ to follow a circular trajectory. (a) Tracking errors under $\overline{\mathcal{C}}$. (b) Controller inputs under $\mathcal{C}$. 58

4.9. Performance comparison of the two controllers $\mathcal{C}$ and $\overline{\mathcal{C}}$ to follow a circular trajectory. (a) Balancing roll angles and position errors under $\overline{\mathcal{C}}$. (b) Balancing roll angles and position errors under $\mathcal{C}$. 58

5.1. (a) Sensitivity factor λ_{φ_h} with varying yaw rate $\dot{\psi}$. (b) Sensitivity factor λ_ϕ with varying bikebot velocity v_r. 67

5.2. Position errors and balancing errors (means and standard derivations) for rider performance: (a) Straight line, middle speed; (b) $R = 6$ m circle, middle speed; (c) $R = 6$ m '8'-figure, middle speed. 72

5.3. Horizontal positions (means and standard derivations) for rider performance:(a) Circle, middle speed; (b) $R = 6$m '8'-figure, middle speed; (c) $R = 4$m '8'-figure, middle speed. 73

5.4. Balancing Metrics (means and standard derivations) for rider performance: (a) Balancing states φ_b and φ_h; (b) Control outputs steering angle ϕ and leaning torque τ_h; (c) BM_1; (d) BM_2. (For (a) and (b), Blue solid lines are real measurements, and Red dash lines are calculation results based on EIC-based control structure. For (d), Blue, green and red lines are BM_{21}, BM_{22} and BM_2 respectively.) 74

5.5. Path following comparison of bikebot and human rider (an example of '8'-figure path): (a) horizontal position, (b) steering angle ϕ and rolling angle φ_b. 74

5.6. Means and standard derivations of performance metrics: (a,d) BM_1, (b,e) BM_{21} and (c,f) BM_{22}. ((a-c): bikebot autonomous riding, (d-f): human rider riding; blue: straight line; red: 6 m radius circle; green: 4 m radius circle; purple: 6 m radius '8'-figure; black: 4 m radius '8'-figure.) 75

6.1. A rider's upper-body balance control model [1]. 81

6.2. (a) Handlebar and front wheel steering angle sensors and front wheel steering actuator. (b) Visual blocking glasses and mirror glasses. 87

6.3. Experimental results for rider-bikebot dynamics models validation. (a) Balancing torques in the first equation of rider-bikebot dynamics. (b) Balancing torques in the second equation of rider-bikebot dynamics. 89

6.4. Rider steering and upper-body movement model validation results. (a) Rider upper-body and bikebot roll angle profiles (top plot) and bikebot position trajectory (bottom plot). (b) Validation results for the rider steering control model ϕ in (6.2) (top plot) and the upper-body movement torque model τ_h in (6.1) (bottom plot). 90

6.5. Model parameter and time delay variations in experiments with five subjects under different visual conditions. (a) Parameter k_{b1}. (c) Time delay τ_3. (c) Time delay τ_4. 91

6.6. Control model parameters and human steering time delays under varying steering actuation delay τ_s. (a) Human steering control gain k_{b1}. (b) Total steering delay τ_{s3}. (c) Total steering delay τ_{s4}. (d) Human upper-body control gain k_{b1}. (e) Human steering control delay τ_3. (f) Human steering control delay τ_4. 92

6.7. Mean values and standard deviations across all subjects with respect to experiments conditions. 95

6.8. Balance metric BM (mean and standard deviation) for five subjects under (a) varying steering actuation delay t_s and (b) visual conditions. 95

6.9. Stable region in the k_{b1}-k_{b2} plane at different steering actuation delays. (a) $\tau_{s3} = 200$ ms. (b) $\tau_{s3} = 300$ ms. (c) $\tau_{s3} = 350$ ms. Red solid curve indicates the stable region calculated by the mean values of the control model parameters, green dot and blue dash curves indicate the stable regions calculated by the one standard deviation below and above the mean values of all model parameters, respectively. The different area generated by lower and upper boundary are the bright green region. The point in grey region belongs to one of the areas generated by mean, lower and upper boundaries. Individual dot represents each subject experiment test. "$\times$", "$\square$","$\star$", "$\circ$" and "$\diamond$" marks indicate subjects A to E, respectively. Blue and red marks indicate the stable and unstable parameters point respectively. 98

6.10. Stable region in the τ_{s4}-τ_{s3} plane at different steering actuation delays. (a) $\tau_{s3} \in [160, 240)$ ms. (b) $\tau_{s3} \in [240, 320)$ ms. (c) $\tau_{s3} \in [320, 400]$ ms. Grey area indicates the stable region calculated by the mean values of the control model parameters. (All experiments trails are divided into 3 sets corresponding these τ_{s3} intervals. In every group, the average value of the upper-body time delays and all the control gains generate the grey areas.) In the figures, individual dot represents each subject experiment test. "$\times$", "$\square$","$\star$", "$\circ$" and "$\diamond$" marks indicate subjects A to E, respectively. Blue and red marks indicate the stable and unstable parameters point respectively. 99

6.11. Stability regions under different model parameters and delays. $Re(\lambda_0)$ values under varying (a) τ_{s3} and τ_{s4}. (b) k_{b1} and t_{s3}. (c) τ_1 and τ_2. Stability regions under varying (d) τ_{s3} and τ_{s4}. (e) k_{b1} and τ_{s3}. (f) τ_1 and τ_2. In (d)-(f), stable regions are marked with $Re(\lambda_0) < 0$. 100

6.12. $Re(\lambda_0)$ values under varying k_{h1} and k_{h2} with (a) $\tau_{s3} = 200$ ms and $\tau_{s4} = 160$ ms and (b) $\tau_{s3} = 350$ ms and $\tau_{s4} = 310$ ms. 101

6.13. Stability regions under under varying τ_1 and τ_2 with different delays τ_{s3} and τ_{s4}. The stable region is marked with $Re(\lambda_0) < 0$. Blue "$\square$", green "$\times$", red "$\diamond$", and black "$\circ$" marks indicate the estimated mean values of (τ_1, τ_2) for each subject under these four pairs of time delay combinations τ_{s3}/τ_{s4}, respectively. 102

6.14. Stability regions under different model parameters in zero speed case. $Re(\lambda_0)$ values under varying (a) τ_3 and τ_4. (b) τ_1 and τ_2. (c) k_{b1} and k_{b2}. (d) k_{h1} and k_{h2}. In (e)-(h), stable regions are marked with $Re(\lambda_0) < 0$. 105

7.1. Comparison of experimental results under three controllers for one subject. The first column is under normal riding control, the second and the third column plots are under $\mathcal{C}$ and $\mathcal{C}_a$, respectively. In (a)-(c), the top plots are the handlebar steering angle ϕ_h and actual steering angle ϕ. The bottom plots are the human upper-body torque τ_h. In (d)-(f), the top plots are the bikebot roll angle φ_b and rider upper-body roll angle φ_h. The bottom plots are the applied disturbance torque τ_g. 116

7.2. Mean values and standard variance across all subjects with respect to experiments conditions: (a). Balancing metric BM_1 and BM_2. (b). Control gains k_{t1} and k_{b1}. 118

7.3. Values of $Re(\lambda_0)$ with different gains k_{t1} and k_{t2} under controllers $\mathcal{C}$. 119

Chapter 1
Introduction

1.1 Motivation

Enhancing the performance and extending the capabilities of human-machine interaction (HMI) systems, and in particular, unstable physical human-machine interaction (upHMI) systems are interesting challenges. Research into these topics, especially in terms of theory and implementations for the modeling and control of these interactions, is sparse due to the involvement of human motor skills and the complex dynamics of such systems. In this dissertation, a bicycle system is considered as a new research paradigm for HMI modeling, autonomous transportation system reinforcement, and human balance control performance tuning.

Despite our highly developed modern transportation system, bicycles and motorcycles are still considered important transportation tools that we include in our daily routines, due to their high maneuverability and agile off-road capabilities. Furthermore, these single-track vehicles provide a perfect platform for recreation, exercises, competitive sports, and even patients rehabilitation. Therefore, enhancing the safety and efficiency of these systems is desirable and critical. To achieve this, we must not only model and analyze the human motor skills necessary to balance the bicycle while following a path, but we must also develop an actively controlled bicycle-based robot system to tune the rider-bicycle interaction.

When looked at in the framework of HMI systems, a rider-bicycle system presents many research questions. First, rider motor skills are an important part of these systems, however, compared to sitting, standing, and walking, research on balancing while riding is

limited and must therefore be investigated. Furthermore, understanding how to sense and fuse human and machines states, and how to reshape human maneuvers are both extremely important steps toward enhancing the capabilities of rider-bicycle human-in-the-loop systems. Finally, built on this human control mechanism and robotics system, the human motor skills assisting and training system can be developed.

The main goals of this dissertation are twofold. The first one is to develop the balancing and tracking control of an autonomous bicycle system, and the second one is to better understand the human rider balancing and path-tracking motor skills through rider-bicycle interactions. The work done towards achieving these two goals lays the foundation for the development of the rider assistive riding system and the design of the rider motor skills tuning system. The last part of this dissertation investigates this topic further.

1.2 Background

A discussion on the state of HMI systems research, and rider-bicycle interaction in particular, can be divided into two parts: autonomous bicycle systems, and human control mechanisms.

1.2.1 Autonomous bicycle systems

The history of bicycles dynamics modeling and stability analysis is over one hundred years. "Whipple Model" in [2] discusses the non-minimum phase system property and the stability with the linearized model structure. Based on the precise calculation of multi-body dynamics and model linearization, the study in [2] firstly systematically demonstrates the self-stable characteristics for a uncontrolled bicycle under the influences of bicycle geometry, mass distribution and bicycle velocity. However, due to the complex geometric and non-holonominal constraints, it is difficult to get the express form of the original nonlinear dynamics in [2]. Thus, that is not a suitable model facing to control. The nonlinear models in [3, 4] proposed some approximated relationships between the steering and the

balancing torques, which can be utilized in the controller design. Furthermore, the complex tire ground frictional interactions are also considered and fused into the whole system dynamics in [5–9].

For the trajectories tracking by only using the steering and velocity control inputs, bicycle is a typical non-minimum phase underactuated system. It is proven that no continuous control exists for exactly tracking with keeping internal subsystem stable [10]. Feedback linearization control methods are designed for balancing task. For example, the sliding mode control strategy is utilized for the balancing and tracking task in [4]. Considering that the bicycle dynamics has the external/internal convertible (EIC) structure [11], a series of EIC-based control strategies are proposed for implementing the approximate tracking task. First, the classic EIC-based controller is utilized for the simplified bicycle model [11]. The modified EIC-based control laws are designed for the complex bicycle/motorcycle models that include the special steering balancing effect and the tire ground interaction [12]. Additionally, the steering effect is proven to be able to balance a stationary bicycle [12]. However, the experimental results for this control system are inadequate comparing with the theoretical work. The results of Blue Team in the 2005 DARPA Challenge confirm these difficulties [13]. The recent experimental results of precisely trajectories tracking are mentioned in [14]. In the recent years, Honda company proposes a motorcycle assist system [15] that has the excellent balancing capabilities at zero or slow velocity.

To enhance the autonomous bicycle balancing and tracking capabilities and considering human rider operations, auxiliary devices are introduced and equipped on the typical bicycle system, such as the weight lifting devices and gyro-balancers. These devices can provide additional control inputs for internal subsystem keeping stable, and improve the whole system balancing and tracking performances. The effect of weight shifting operation, which can be considered as the rider upper-body leaning motion, is shown to eliminate the right half-plane zeros of the linearized closed-loop system [16]. The gyro-balancer is another control inputs for balancing, such as the developments in [17–19]. The bikebot

system [14, 20] is built for the autonomous bicycle control laws implementation and human riding process observation. In [20], for the stationary bicycle, the gyro-balancer is shown to regulate the bicycle rolling motion on a designed periodical orbit. Based on the EIC structure, in [14], the gyro-balancer is designed as an auxiliary control for assisting the bicycle balance and enhancing the trajectories tracking performances.

1.2.2 Human control mechanisms modeling and analysis

Modeling human control mechanisms is a complete and challenging task for several reasons. Models must account for not only a non-rigid human body and multiple contact interactions, but also complex human sensing, actuation and decision mechanisms. As much, most research in this area focuses on the control of sitting, standing or walking motions.

For human stance, the whole or upper-body is approximately considered as an inverted pendulum. Following the same treatment, the rider upper-body leaning motion in cycling is modeled as an inverted pendulum swing motion [12, 21, 22]. This motion is one of the main balancing sources generated by the rider. The precise dynamics model including the other joints motion of the upper-body, arms and legs are also constructed. The work in [23] proposes a physical-learning model for depicting these motions, which uses a low-dimensional learning-based model to simulate the complex high dimensional dynamics effectively. In most studies, only the upper-body leaning motion is considered in the system stability analysis. The rider posture estimation is necessary for the rider physical dynamics validating and the rider control model construction. In [24, 25], the wearable inertial measurement units (IMUs), including the accelerometers and gyroscopes, are used for the body segments orientation and position estimation. Other sensors, such as the magnetic sensor and the onboard camera, are also introduced to enhance the measure precision and to eliminate the IMU drifting effect [26, 27].

It is challenging to capture and model human control motor skills. The motor skills depict the combination of human sensing, decision and actuation. Several neuro-balancing models are constructed for human stance. In [28], a time-delayed proportional-derivative

(PD) feedback control model is proposed. In those models, the time delayed human angular positions and angular velocities are multiplied by the control gains as the balancing joints torques. The model depicts the human sensory response to balancing states as short-, medium- and long-latency phasic mechanisms due to proprioception, vestibular and visual sensory. The muscle stiffness and damping factors of the neuro-musculoskeletal system are also considered in the model. Experiments are conducted and used to validate the model structure and identify the model parameters, the control gains and time delay constants. However, the closed-loop system stability was not analyzed and included in [28]. A similar simplified control model structure is used for standing on balancing board problem. Properties of the nonlinear closed-loop dynamics are discussed quantitatively, such as the limit cycle existence and the bifurcation phenomena. The work in [29, 30] gives the qualitative discussion of human riding behaviors, from the dynamics viewpoint and based on the experimental observation. The balance control model in [28] is also used for capturing the stationary balancing riding in [31] and for riding stability analysis [1].

Besides balancing task, the human motor skills for complex operations are also discussed in recent years. In [32], the motion planning method is conducted on the learned low-dimensional skill manifolds but not the complex analytical robotic models. The manifold concepts are utilized for depicting the human motion sets and synergies relationships in [33, 34]. Human motor skills learning process and behavior forming process are also discussed, such as [35] for a kind of simulated non-minimum phase system tracking task. However, these aforementioned works mainly focus on the human motor skills without considering the dynamics interactions between human and machines. Few quantitative analysis is reported for the rider path tracking with balancing maneuvers.

1.3 Dissertation outline and contributions

This dissertation is divided into eight chapters. Chapter 1 is the introduction of the dissertation. Chapter 2 presents the bikebot system dynamics and the rider-bicycle dynamics and

also introduces the experiment setup. In Chapter 3, the control system for bikebot balancing task under different velocities is designed and implemented. Chapter 4 demonstrates the EIC-based control strategies with and without gyro auxiliary operation. In Chapter 5, based on the EIC structure dynamics analysis, the human path following riding performances are analyzed. In Chapter 6, the human rider balancing control models are presented and also experimentally validated. The closed-loop system stability analysis is also presented. In Chapter 7, we present the tuning and control of the interaction dynamics. Finally, Chapter 8 presents the concluding remarks of the current work and the discussion of the future work. The content of each chapter is described as follows.

Chapter 2 is about the physical system dynamics and experimental setup. First, the dynamic models of the bikebot and the rider-bicycle systems are introduced. These models depict the influence of the steering and bicycle speed changing on platform balancing. The balancing torque generated by the gyro-balancer is also calculated for the bikebot. For the rider-bicycle system, the upper-body leaning torque is included in the model. Second, we present the bikebot experimental system. This prototype is used for implementing the autonomous riding control algorithms.

Chapter 3 provides the design for the autonomous bikebot balancing task under different velocities. For the stationary balancing, the bikebot is controlled to periodically swing near the unstable equilibriums by the gyro-balancer's flywheel pivoting actuation. The desired periodical orbits of bicycle rolling motion and flywheel pivoting motion are constructed by using the energy shaping technique. A Lyapunov-based nonlinear control law is designed to regulate both the bikebot rolling and flywheel pivoting motion onto their desired orbits. For task of balancing in moving stage, the steering motion is used for balancing the system. Based on the feedback linearization method, the steering control law is proposed. Considering the closed-loop dynamics with parameters and the actuators motion limitation, the domains of attraction (DOAs) are estimated under these two control laws. Furthermore, the largest DOAs are also estimated which depend on only the motion limitation, but not on the control law structures. From these control capabilities analysis, a

switching control strategy is proposed for balancing in the stationary-moving stages transition process. The experiments results demonstrate the performances of the aforementioned control methods.

Chapter 4 focuses on the bikebot autonomous tracking tasks. First, using the steering properties of the EIC structure, we present a tracking and balancing control strategy. The tracking and balancing errors analysis is then discussed. Considering the non-minimum phase system property, an auxiliary gyro pivoting control law is designed for reducing the path tracking errors. The tracking performance of these two control methods are demonstrated by both the analysis and the experiments. The EIC-based control with modified velocity vector field is also implemented.

Chapter 5 presents the analyzing methods and results about the human rider path tracking and balancing performance. Based on the EIC structure, the balance equilibrium manifold (BEM) concept is introduced. Based on the BEM concepts, we first analyze the balancing contribution of the steering and the upper-body leaning operations. The analysis shows that using the steering actuation is much more effective than the body movement in term of platform balance task. A balancing metric is also defined for measuring the balancing performance along the rider tracking process. A second metric is introduced for depicting the tracking and balancing results of riders. Finally, multiple riders are asked to control the bikebot to track the given paths. These rider experiments results are used to demonstrate the effectiveness of the proposed analyzing methods.

In Chapter 6, the human balance skills are discussed. Based on the recorded data from the conducted balance riding experiments, the control models of steering operation and upper-body leaning torque are constructed and proposed in this chapters. Both control models share the time delayed PD feedback structures with the bicycle frame and the upper-body rolling information. We then discuss the stability analysis of the linearized closed-loop system. For the stability and balancing performances, the influence of the changing of the dynamics physical parameters, the control gains and time delays in the human control

models are also discussed. Extensive experiments are conducted by multiple subjects, under different types disturbances, the rolling torque perturbation by gyro pivoting, the visual feedback channel disturbance and the additional time delay on the steering actuator. We analyze these experimental results and present the human balance motor skill changes.

Using the rider-bikebot interaction to enhance the human rider riding performance is the aim of the work presented in Chapter 7. The interaction model is rewritten to a strict feedback form first. From the steering actuation to bikebot rolling motion, the stiffness and damping effect of the interaction dynamics are analyzed. A stiffness and damping effects tuning method is designed by reshaping and implementing the rider steering angle. Several riders are requested to ride the bikebot under the tuned different interaction models. Performance comparisons are also presented among the human normal riding and the proposed rider-bikebot interactions controllers. It has been demonstrated that the balance performance and the stability of the controlled rider-bikebot interactions are significantly improved comparing to that with only human control. Furthermore, from theoretical analysis, under some special tuned stiffness and damping effects, the rider-bicycle system can be balanced autonomously without rider control. This property is also verified by the experiments.

The main contributions of this dissertation focus on the new control methods of autonomous control system and new modeling and analysis of human riding behaviors. The detailed contributions of this dissertation are listed as follows.

1. Novel control methods for bikebot autonomous balancing task in stationary stage and stationary-moving transition process are designed and implemented by experiments, including the orbital construction, stabilization and switching control. These innovative approaches are helpful not only for enhancing the balancing capabilities of the autonomous bicycle system, but also for the human riding assisting system design, especially under small or zero velocity conditions.

2. The autonomous tracking and balancing control system is new. To the best knowledge

of the author, no such experiments have been reported in the past.

3. The human riding behaviors for balancing and tracking tasks are systematically collected, observed and analyzed under designed experiments conditions with multiple types of disturbances. Based on this work, the human balancing motor skills are analyzed. These experiments and methods are new.

4. The human rider control models for balance riding are proposed and validated. This work provides in-depth understanding of human riding control mechanism, and a novel compensation method for general balancing mechanism study and the human-in-the-loop system design.

5. The rider tracking with balancing control skills are analyzed. We present new BEM concepts and metrics for measuring the rider performances. These metrics are new and can be used to capture and characterize the motor skills. The EIC-based evaluation indexes and the analyzing tool give the guidance for the rider assisting system design. Furthermore, these methods can also be extended to other human-machine interaction analysis, especially for the unstable control system.

6. A novel rider-bikebot interaction tuning method is designed and implemented in experiments. The method can effectively enhance the human rider riding safety and balancing performances. The proposed interaction tuning methodology has a potential value for riding training system design. To the best knowledge of the author, riding balance tuning design and experiments have not been reported in the past.

Chapter 2
System Dynamics and Experiment System

2.1 Introduction

For understanding the rider-bicycle system interaction and enhancing the autonomous bicycle system capability, the dynamic model construction is an important and foundational work. For validating the rider-bicycle interaction analysis, implementing the autonomous control system and assisting/perturbing the rider behaviors, building an autonomous bicycle experimental system is necessary and critical.

Lots of works have been done to depict the dynamics of the moving motorcycle and bicycles, including the special geometry structure and the tire-road interaction [12]. Based on the no-slipping and no-sliding assumption, the non-holonomic constraints are introduced, and the Whipple model is constructed for the moving bicycle utilizing multi-body Lagrangian equations [29]. Some self-stability properties are demonstrated under different geometrical and mass distribution parameters [2, 36]. Besides, the tire-road friction model is combined under the slipping and sliding condition [3]. Considering the lateral motion of the tire-ground contact point, the stationary motorcycle dynamics with an accurate steering mechanism is proposed in [37]. The bikebot system with gyro-balancer dynamics is also constructed in [14, 37], with the analysis of coupling effect from flywheel pivoting motion with bicycle frame rolling motion. Furthermore, combining the bicycle dynamics with the rider body motion, the rider-bicycle system dynamics is also studied in recent years. In [21, 22], the rider upper-body is considered as an inverted pendulum mounted on the bike seat, and the upper-body leaning motion is considered as an important motion for balancing.

The first part of this chapter demonstrates the rider-bicycle dynamics, and autonomous bikebot dynamics, which are mentioned in [21, 22] and [14, 20], respectively. Comparing with other rider-bicycle dynamic models, the rider upper-body leaning torque, the main balancing torque generated by riders, are picked up and calculated in the dynamics. For the bicycle part, some different kinds of balancing torques resulting from steering are also included. The second part focuses on the experiment system, which is mentioned and utilized in the works of [14, 20–22]. The functions and design details of sensing, data processing and actuating are included. It has to be pointed out that, the dynamics construction works are from the cooperation of this dissertation author and his research group colleague Dr. Yizhai Zhang, and for the experiment system, the author focuses on the redesign and modification works about the sensors, programs and actuators. The original bikebot design is proposed by colleague Dr. Yizhai Zhang [12]. Considering the whole work completeness and without repeating to mention these backgrounds, the dynamics and experimental system are proposed in this chapter as the preparing and basic work of the entire dissertation work.

The rest part of this chapter is organized as follows. The bikebot dynamics and rider-bicycle system dynamics are introduced in Section 2.2 and 2.3, respectively. Section 2.4 demonstrates the experimental system. The conclusion is listed in Section 2.5.

2.2 Bikebot system dynamics

As shown in Fig. 2.1(a), the bikebot system can be considered as several inter-connected parts: the rear frame with the rear wheel, the gyro-balancer mounted on the rear frame, and the front wheel. There are three coordinate frames are introduced for motions and attitude descriptions: the fixed inertial frame $\mathcal{N}$, the translating and rotating body frame $\mathcal{B}$, and the translating trajectory frame $\mathcal{R}$. As shown in Fig. 2.1(b), the origin of $\mathcal{R}$ frame is attached at the rear wheel contact point C_2 with x-axis parallel with the wheel base C_1C_2, which is defined as the straight line connecting the front wheel contact point C_1 and the rear wheel's

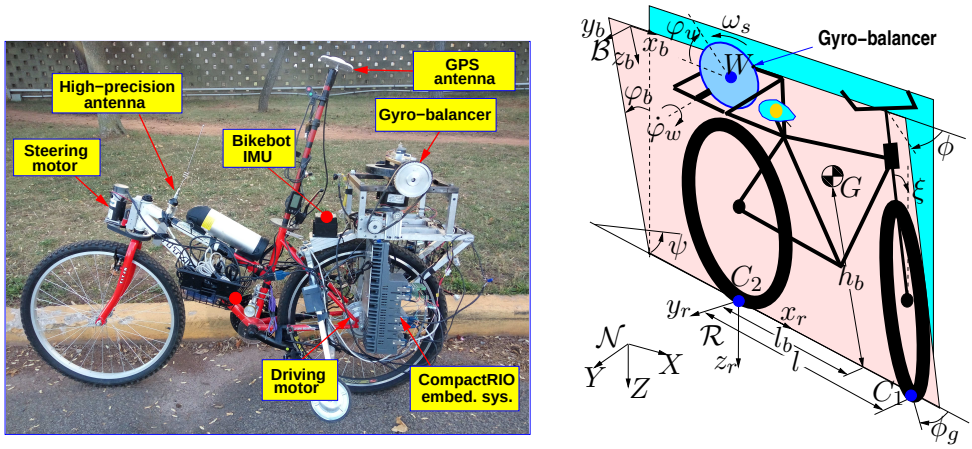

(a) (b)

Figure 2.1: (a) The Rutgers bikebot system. (b) A kinematic schematic of the gyro-balanced bikebot system.

C_2. The C_2 velocity along x_b is defined as v_r. The z-axis of frame $\mathcal{R}$ is parallel with the z-axis of $\mathcal{N}$. Bikebot roll angle, the angle between the z-axis of $\mathcal{B}$ and z-axis of $\mathcal{N}$, is defined as φ_b. The yaw angle ψ is defined as the angle between the x-axis of $\mathcal{N}$ and x-axis of $\mathcal{R}$. The horizontal and vertical positions of the mass center point G with respect to $\mathcal{B}$ are l_b and h_b, respectively. The bicycle mass and mass moment of inertia about G point in the direction of the x-axis of $\mathcal{B}$ are m_b and J_b, respectively. The length of wheel base C_1C_2 is denoted as l. And the front wheel caster angle is denoted as ξ, and the front wheel trail distance is denoted as l_t. With the steering angle ϕ, the projective steering angle on the ground is ϕ_g, which can be calculated as [1]

$$\phi_g = \arctan\left(\frac{\tan\phi\,\mathrm{c}_\xi}{\mathrm{c}_{\varphi_b}}\right).$$

As the same treatment in [22], the relationships between ψ and ϕ are

$$\dot{\psi} = \frac{v_r \tan\phi\,\mathrm{c}_\xi}{l\,\mathrm{c}_{\varphi_b}} \tag{2.1}$$

and

$$u_\psi = \frac{v_r\,\mathrm{c}_\xi}{l\,\mathrm{c}_{\varphi_b}}\left(\sec^2_\phi\,\dot{\phi} + \tan\phi\tan\varphi_b\dot{\varphi}_b\right) + \frac{\dot{v}_r\tan\phi\,\mathrm{c}_\xi}{l\,\mathrm{c}_{\varphi_b}} \tag{2.2}$$

with defining $u_\psi = \ddot{\psi}$.

[1] Notation $\mathrm{c}_x = \cos x (\mathrm{s}_x = \sin x)$ for variable x is used through the entire dissertation.

Combining the rolling and the yawing motion, the center mass point linear velocity vector $\boldsymbol{v}_g$ w.r.t. $\mathcal{N}$ expressed in $\mathcal{B}$ is

$$\boldsymbol{v}_G = \left(v_r - h_b\dot{\psi}\,\mathrm{s}_{\varphi_b}\right)\boldsymbol{i}_b + \left(h_b\dot{\varphi}_b + l_b\dot{\psi}\,\mathrm{c}_{\varphi_b}\right)\boldsymbol{j}_b - l_b\dot{\psi}\,\mathrm{s}_{\varphi_b}\,\boldsymbol{k}_b \tag{2.3}$$

with $\boldsymbol{i}_b$, $\boldsymbol{j}_b$ and $\boldsymbol{k}_b$ as the unit vectors of the x_b-, y_b- and z_b-axes of $\mathcal{B}$, respectively.

The height of the center mass is mainly dominated by the rolling motion by the term $h_b c_{\varphi_b}$. Furthermore, at small φ_b case, another height changing factor Δh_b has to be considered due to the combination of rolling and steering, which can be approximated as

$$\Delta h_b \approx \frac{l_t l_b\,\mathrm{c}_\xi \tan\phi\,\mathrm{s}_{\varphi_b}}{l}. \tag{2.4}$$

Thus, the potential energy V is

$$V = m_b g\left(h_b\,\mathrm{c}_{\phi_b} - \frac{l_t l_b\,\mathrm{c}_\xi \tan\phi\,\mathrm{s}_{\varphi_b}}{l}\right). \tag{2.5}$$

The pivoting angle of the spinning flywheel is φ_w along the y-axis of $\mathcal{B}$, and the spinning angular velocity is ω_s. Another pivoting coordinate frame $\mathcal{F}$ is introduced, in which the y- and z-axes are accorded by the definitions of φ_w and ω_s, respectively. $\boldsymbol{i}_f$, $\boldsymbol{j}_f$ and $\boldsymbol{k}_f$ are the unit vectors of the x-, y- and $z-$ axes directions in $\mathcal{F}$. Thus, the angular velocity vector $\boldsymbol{\omega}_f$ w.r.t to $\mathcal{N}$ expressed in $\mathcal{F}$ is

$$\boldsymbol{\omega}_f = \left(\mathrm{c}_{\varphi_w}\,\dot{\varphi}_b - \mathrm{s}_{\varphi_w}\,\mathrm{c}_{\varphi_b}\,\dot{\psi}\right)\boldsymbol{i}_f + \left(\mathrm{s}_{\varphi_b}\,\dot{\psi} + \dot{\varphi}_w\right)\boldsymbol{j}_f + \left(\mathrm{s}_{\varphi_w}\,\dot{\varphi}_b + \mathrm{c}_{\varphi_w}\,\mathrm{c}_{\varphi_b}\,\dot{\psi} + \omega_s\right)\boldsymbol{k}_f. \tag{2.6}$$

Let I_z be the mass moment of inertia of the flywheel along the spinning axis. Naturally, the mass momentum of inertia along the y- and x-axes of $\mathcal{F}$, I_x and I_y are approximated as $\frac{I_z}{2}$. The inertia matrix $\boldsymbol{I}_w$ expressed in $\mathcal{F}$ is $\boldsymbol{I}_w = diag\left\{\frac{I_z}{2}, \frac{I_z}{2}, I_z\right\}$.

The total kinematic energy T is obtained as

$$T = \frac{1}{2}m_b\boldsymbol{v}_G^T\boldsymbol{v}_G + \frac{1}{2}J_b\dot{\varphi}_b^2 + \frac{1}{2}\boldsymbol{\omega}_f^T\boldsymbol{I}_w\boldsymbol{\omega}_f. \tag{2.7}$$

The balancing dynamics along the x-axis of $\mathcal{B}$ has the general coordinates $\boldsymbol{q} = [\varphi_b, \varphi_w]^T$ under the controlled pivoting torque τ_p. After defining the Lagrangian $L = T - V$, the Lagrangian equation is utilized for the dynamics construction

$$\frac{d}{dt}\left(\frac{\partial L}{\partial \dot{q}_i}\right) - \frac{\partial L}{\partial q_i} = u_i, i = 1, 2, \tag{2.8}$$

with $u_1 = 0, u_2 = \tau_p$. From (2.8), we obtain the equation of motion

$$\begin{aligned}
&\left(m_b h_b^2 + J_b + I_z \,\mathrm{s}_{\varphi_w}^2 + \tfrac{I_z}{2}\,\mathrm{c}_{\varphi_w}^2\right)\ddot{\varphi}_b + m_b h_b \,\mathrm{c}_{\phi_b}\, v_r \dot{\psi} - m_b h_b^2 \,\mathrm{c}_{\varphi_b}\,\mathrm{s}_{\varphi_b}\,\dot{\psi}^2 \\
&-\tfrac{m_b g l_t l_b \tan\phi \,\mathrm{c}_\xi \,\mathrm{c}_{\varphi_b}}{l} - m_b h_b g \,\mathrm{c}_{\varphi_b} - m_b h_b l_b \,\mathrm{c}_{\varphi_b}\, u_\psi \\
&+I_z \,\mathrm{c}_{\varphi_w}\left(\omega_s - \tfrac{1}{2}\dot{\varphi}_b \,\mathrm{s}_{\varphi_w} - \tfrac{1}{2}\dot{\psi}\,\mathrm{c}_{\varphi_b}\,\mathrm{c}_{\varphi_w}\right)\left(\dot{\varphi}_w - \mathrm{c}_{\varphi_b}\,\dot{\psi}\right) = 0
\end{aligned} \tag{2.9}$$

and

$$\begin{aligned}
&\tfrac{I_z}{2}\ddot{\varphi}_w + I_z \,\mathrm{c}_{\varphi_w}^2\,\mathrm{c}_{\varphi_b}\,\dot{\psi}\dot{\varphi}_b + \tfrac{I_z}{2}\,\mathrm{c}_{\varphi_w}\,\mathrm{s}_{\varphi_w}\,\dot{\varphi}_b^2 - \tfrac{I_z}{2}\,\mathrm{c}_{\varphi_w}\,\mathrm{s}_{\varphi_w}\,\mathrm{c}_{\varphi_b}^2\,\dot{\psi}^2 \\
&+I_z\omega_s\left(\dot{\psi}\,\mathrm{c}_{\varphi_b}\,\mathrm{s}_{\varphi_w} - \tfrac{1}{2}\dot{\varphi}_b\,\mathrm{c}_{\varphi_w}\right) - \tfrac{I_z}{2}\,\mathrm{s}_{\varphi_b}\,u_\psi = \tau_p.
\end{aligned} \tag{2.10}$$

The trajectory motion kinematics is calculated as follow. The 2-dimensional position of rear wheel contact point C_2 is defined as $\boldsymbol{r}_{C_2} = [X, Y]^T$ in $\mathcal{N}$, with velocity $\boldsymbol{v}_{C_2} = \dot{\boldsymbol{r}}_{C_2}$. Under the non-holonomic constraint of C_2, the lateral velocity is zero and the velocity $\boldsymbol{v}_{C_2}$ has the relationship with v_r and ψ as

$$\boldsymbol{v}_{C_2} = \begin{bmatrix} v_X \\ v_Y \end{bmatrix} = \begin{bmatrix} \dot{X} \\ \dot{Y} \end{bmatrix} = \begin{bmatrix} \mathrm{c}_\psi & -\mathrm{s}_\psi \\ \mathrm{s}_\psi & \mathrm{c}_\psi \end{bmatrix} \begin{bmatrix} v_r \\ 0 \end{bmatrix}. \tag{2.11}$$

After taking twice derivatives, under the control input $u = [u_r, u_\psi]$ with $u_r = \ddot{v}_r$, the dynamics extension results in

$$\boldsymbol{r}_{C_2}^{(3)} = \ddot{\boldsymbol{v}}_{C_2} = -\underbrace{\begin{bmatrix} 2\dot{v}_r \,\mathrm{s}_\psi + v_r\dot{\psi}\,\mathrm{c}_\psi \\ -2\dot{v}_r \,\mathrm{c}_\psi + v_r\dot{\psi}\,\mathrm{s}_\psi \end{bmatrix}}_{\boldsymbol{\Psi}}\dot{\psi} + \underbrace{\begin{bmatrix} \mathrm{c}_\psi & -v_r \,\mathrm{s}_\psi \\ \mathrm{s}_\psi & v_r \,\mathrm{c}_\psi \end{bmatrix}}_{\boldsymbol{R}_\psi} u. \tag{2.12}$$

2.3 Rider-bicycle system dynamics

For the rider-bicycle system, the kinematics of the trajectory motion is same as that of the aforementioned bikebot system. Only the rolling dynamics is given in this section, which is also similar as the former system.

As shown in Fig. 2.2(b), the rear frame and steering structures of the rider-bicycle system are the same as the bikebot in Fig. 2.1(b). The flywheel part is not considered in the dynamics. One main difference is that the upper-body motion is considered. Naturally, the upper-body with arms has multiple DoFs. However, only the upper-body leaning motion

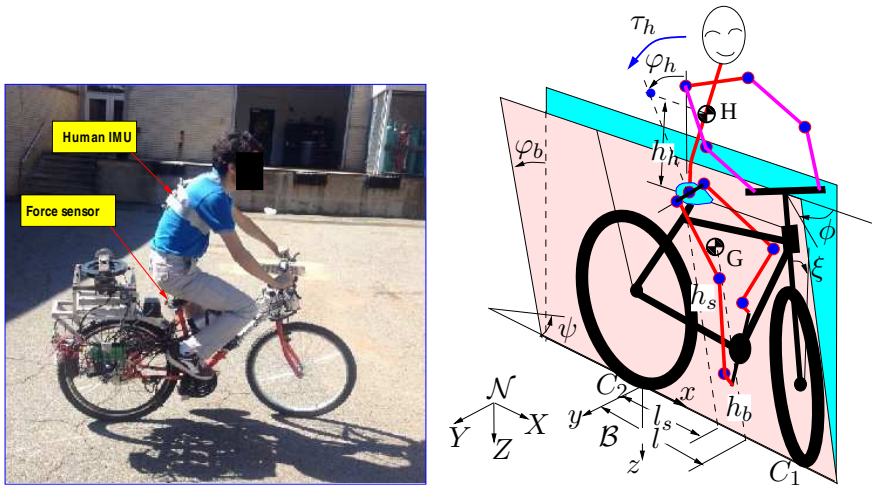

(a) (b)

Figure 2.2: (a) Human riding experiment. (b) A kinematic schematic of the rider-bicycle system.

is considered since it has the significant influence on the rolling dynamics. Therefore, the upper-body is simplified as an inverted pendulum with a mass m_h and mass moment of inertia J_h. The mass center is at distance h_h from the seat, and the horizontal and vertical positions of the seat are l_s and h_s in $\mathcal{B}$, respectively. The swing angle φ_h w.r.t. the z-axis of $\mathcal{B}$ is defined as the human rider upper-body leaning angle. The human leaning torque τ_h is considered as a control input.

Following the same process in the last section, the equations of motion of the rider-bicycle system are

$$\boldsymbol{M}(\boldsymbol{q})\ddot{\boldsymbol{q}} + \boldsymbol{C}(\boldsymbol{q}, \dot{\boldsymbol{q}}) + \boldsymbol{G}(\boldsymbol{q}) = \boldsymbol{\tau} + \boldsymbol{B}\boldsymbol{u}, \tag{2.13}$$

with the states variable $\boldsymbol{q} = [\varphi_b, \varphi_h]^T$, the control inputs $\boldsymbol{u} = [u_r, u_\psi]^T$, and $\boldsymbol{\tau} = [0, \tau_h]^T$. The matrixes and vectors in (2.13) are

$$\boldsymbol{M} = \begin{bmatrix} m_b h_b^2 + m_h \left(h_s^2 + h_h^2 + 2h_s h_h \, \mathrm{c}_{\varphi_h}\right) + J_b + J_h & m_h \left(h_h^2 + h_s h_h \, \mathrm{c}_{\varphi_b}\right) \\ m_h \left(h_h^2 + h_s h_h \, \mathrm{c}_{\varphi_h}\right) & m_h h_h^2 + J_h \end{bmatrix},$$

$$\begin{aligned} \boldsymbol{C}_1 &= \left(m_b l_b + m_h l_s\right) \mathrm{c}_{\varphi_b} \, g l_t \, \mathrm{c}_\xi \, v_r^{-1} \dot{\psi} + \left(m_b h_b \, \mathrm{c}_{\varphi_b} + m_h h_s \, \mathrm{c}_{\varphi_b} + m_h h_h \mathrm{c}_{\varphi_b + \varphi_h}\right) v_r \dot{\psi} \\ &\quad - m_h h_h h_s \, \mathrm{s}_{\varphi_h} \, \dot{\varphi}_h \left(2\dot{\varphi}_b + \dot{\varphi}_h\right) - \left(m_b h_b^2 \, \mathrm{s}_{\varphi_b} \, \mathrm{c}_{\varphi_b} + m_h h_h^2 \tfrac{\mathrm{s}_{2\varphi_b + 2\varphi_h}}{2} + h_s h_h \, \mathrm{c}_{2\varphi_b + \varphi_h}\right) \dot{\psi}^2, \\ \boldsymbol{C}_2 &= m_h h_h h_s \, \mathrm{s}_{\varphi_h} \, \dot{\phi}_h^2 + m_h h_h \, \mathrm{c}_{\varphi_b + \varphi_h} \, v_r \dot{\psi} - \left(m_h h_s h_h \, \mathrm{s}_{\varphi_b} \, \mathrm{c}_{\varphi_b + \varphi_h} + m_h h_h^2 \frac{\mathrm{s}_{2\varphi_b + 2\varphi_h}}{2}\right) \dot{\psi}^2, \end{aligned}$$

$$\boldsymbol{G} = \begin{bmatrix} -m_b h_b g \, \mathrm{s}_{\varphi_b} - m_h h_s g \, \mathrm{s}_{\varphi_b} - m_h h_h g \, \mathrm{s}_{\varphi_b + \varphi_h} \\ -m_h h_h g \, \mathrm{s}_{\varphi_b + \varphi_h} \end{bmatrix},$$

and

$$\boldsymbol{B} = \begin{bmatrix} 0 & -m_b h_b l_b \, \mathrm{c}_{\varphi_b} - m_h h_s l_h \, \mathrm{c}_{\varphi_b} - m_h h_h l_h \, \mathrm{c}_{\varphi_b + \varphi_h} \\ 0 & -m_h h_h l_h \, \mathrm{c}_{\varphi_b + \varphi_h} \end{bmatrix}.$$

2.4 Bikebot experiments system

Fig. 2.3 shows the bikebot experiment system, that can be ride by human rider or controlled by the onboard computer. The bikebot system is designed and built for three aims. The first aim is recording the rider operation and system states, and generating disturbances into the rider's closed-loop sensorimotor feedback system. The second one is experimentally validating the designed autonomous bikebot balancing and tracking controllers. The last one is to tune the human behaviors for enhancing the riding safety and efficiency and training the human riders.

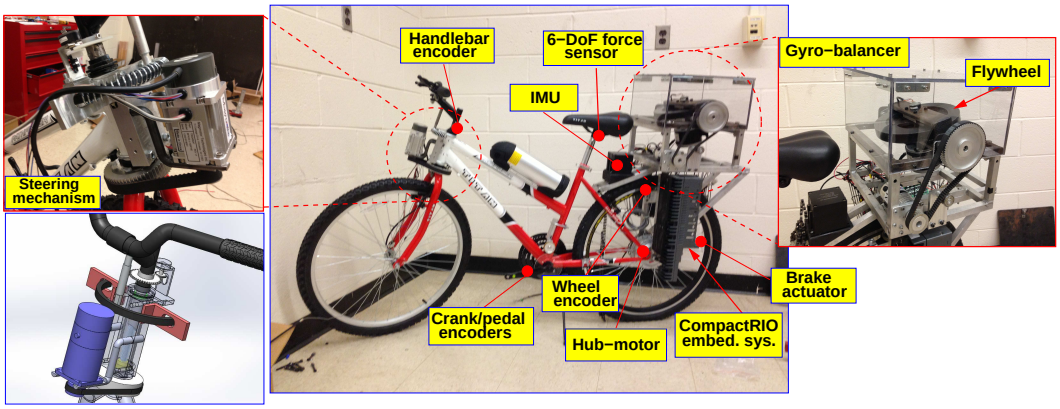

Figure 2.3: The Rutgers bikebot.

This platform is modified from a mountain bicycle with added onboard sensors and actuators. As shown in Fig. 2.4(a), a real-time embedded system (from NI cRIO model 9082) is used for collecting the sensor measurements and also for motion control. For the sensing part, the bicycle velocity v_r is obtained by the encoder mounted on the rear wheel; the steering angle ϕ and the handlebar rotating angle ϕ_h are measured by two encoders on

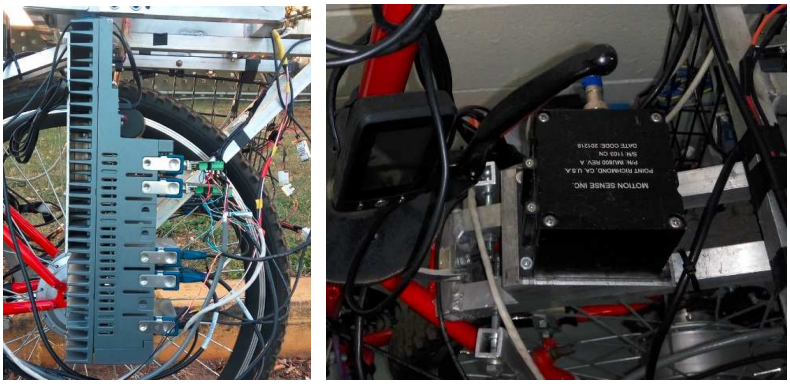

(a) (b)

Figure 2.4: (a) Bikebot data onboard control system. (b) 6-DoFs IMU.

(a) (b)

Figure 2.5: (a) Gyro-balancer part. (b) Autonomous steering part.

the steering structure, and the upper-body relative leaning angle φ_h is captured by a rolling arm equipped with an encoder that is connected to the upper body. In the gyro-balancer subsystem (Fig. 2.5(a)), the flywheel pitching and spinning angles are measured by the encoders. Besides, the bicycle and upper-body 6-DoFs motion information, including φ_b, φ_h and ψ, are detected by two IMUs attached on them. The bicycle frame-fixed IMU is shown in Fig. 2.4(b). The bicycle position is measured by the onboard GPS system, or calculated by the measured steering angle ϕ and bicycle speed v_r along the riding trajectory.

For the actuation parts, the pedaling actuation is powered by a motor through the onboard computer system, while a human rider can still manually control it. As shown in

Fig. 2.5(b), the front wheel can be configured either mechanically connected or disconnected to the handlebar. On one hand, like a normal bicycle, the bicycle steering operation can be carried out directly by the rider through the handlebar. On the other hand, when the front wheel is mechanically disconnected with the handlebar, the steering motion is driven by the steering motor directly. This function provides the capability that the actual steering angle can be controlled to follow a designed profile. For the rolling torque generated by the gyro-balancer subsystem (Fig. 2.5(a)), the pitching angle and spinning speed of the flywheel are independently controlled by two motors.

2.5 Conclusion

The dynamics models of the bikebot system and the rider-bicycle system were proposed in this chapter. The control effects of steering, gyro-balancing torque, and rider upper-body leaning motion were demonstrated in these models. The bicycle experimental system was also demonstrated, in which the states measuring and recording, control processer, and the actuators were introduced.

Chapter 3
Bikebot Autonomous Balancing Control

3.1 Introduction

Bicycles and motorcycles provide an excellent platform for studying human-machine or human-robot interactions. It has also been reported for clinical diagnosis and rehabilitation treatment [38–40]. In [20], an actively controlled bicycle-based robot, called bikebot, is designed to study human neuro-control mechanism and physical human-robot interactions. Due to its non-minimum phase dynamics, it is challenging to design bikebot control system. From practice viewpoint, it is desirable to have a complete autonomous strategy for the bikebot system from stationary to moving maneuvers. However, because of different bikebot dynamics at stationary and moving speed, the platform balance strategies are not the same. The goals of this chapter are to design the balance control laws under stationary and moving conditions, and to develop an integrated stationary and moving balance control for autonomous bikebot.

Dynamics and control of bicycles or motorcycles are among active research areas for many years [16]. Autonomous single-track vehicles need to maintain both trajectory tracking and platform balancing tasks simultaneously. Using the steering and velocity actuations, several controller designs were developed [11, 14, 41–43]. An elegant design in [11] takes advantage of the EIC dynamics structure of the riderless bicycle to design an autonomous controller. A simplified bicycle model is used in [11] and only simulation results are presented to illustrate the design methodology. The work in [14] extends the EIC-based control design and demonstrates the experimental implementation and performance using the bikebot. Other experimental and demonstration works include those in [14, 42, 44, 45].

The stationary balance control is also a difficult task for the bikebot system. The additional rolling torque generated by the gyro-balancer can be used for the balance keeping task. In recent years, control laws are proposed for balancing similar systems, such as the inverted pendulum, Furuta pendulum and acrobat system [46, 47]. These controllers can be divided into two groups: the equilibrium point regulation and orbital regulation. The typical method of the former is the energy shaping and dissipation injection design [48–51]. The latter design is sophisticated with two parts: the orbit constructing and regulation control design. The first part is orbits existence, that is, the target orbit of the system states should be related and they are the solutions of the closed-loop dynamics. Virtual constraints [52, 53], sliding modes [4] or limit-cycle dynamics [54] are introduced, and the system dynamic forms are dominated by the conservation of the first integral. The regulation control law can then drive the states onto their target orbits [55], such as time varying linear feedback control methods with transverse dynamics [56]. In [20], using gyro-balancer, an orbital regulation control law is proposed to balance the platform at stationary or low moving velocities.

It is challenging to estimate the maximum roll motion range under a certain control system. The results in [57] show that the bicycle can only be stabilizable within a small range of roll angles (e.g., 1-2 degs), particularly at low moving velocities. The simple analysis in [37] has showed that balancing a stationary bicycle only by steering actuation is extremely difficult because of a small DOA under the controller design. Introducing additional actuators can overcome this limited stabilizable range and assist the balance capability. However, no formal analysis is given to estimate the DOA under the control design in [20].

In this chapter, the gyro-balancer control law is proposed first for the stationary balance control task. In this task, the orbital regulation is chosen as the control method. That is, the stationary bicycle is expected not only to keep balance but also to swing near the equilibrium point periodically controlled by the gyro-balancer pivoting motion. The energy shaping techniques is utilized for shaping the desired dynamics as a simple pendulum

dynamics. The virtual constraint between the bikebot rolling angle and flywheel pivoting velocity is built to get the desired periodical orbits for the bikeobt frame rolling and flywheel pivoting motion. According to the reshaped energy and proposed virtual constraint, a Lyapunov-based orbital regulation controller is designed. The theoretical stability analysis and experimental results demonstrate that the system states can converge to the desired orbits. It has to be pointed out that for the first time the gyro-balancer stationary balancing control experiment is carried out by the author and Dr. Yizhai Zhang, and other parts in this chapter are completed by the author himself. For balancing of a moving platform, based on the feedback linearization structure, the steering balancing control law is introduced.

We then present an integrated stationary/moving balance control of autonomous bikebots. The control system integrates the balance control strategies for the stationary and moving bikebot platform. Due to different dynamics and control design for stationary and moving bikebot, we analyze the DOAs for the given controllers and then a switching strategy is used to integrate them for stationary-to-moving and moving-to-stop maneuvers. The integration design guarantees that the transition state lies in the DOAs of the closed-loop dynamics under the targeted control design. To demonstrate the DOA analysis and integration design, we use the orbital regulation control law [20] for balancing stationary bikebot and the EIC-based balance control is used for the moving bikebot [22]. Furthermore, a feasible DOA concept is introduced to capture the possibly largest state variable region under any balance control laws with consideration of actuation limits. The main contribution of work lies in the analysis and design of the integrated balance control for the autonomous bikebot in the stationary-moving transition. The switched control design provides guaranteed balance performance and could be used for other underactuated balance robots.

The rest parts of this chapter are organized as follows. Section 3.2 focuses on the task of balancing under only gyro pivoting control design, including the orbits construction and orbital regulation control. Section 3.3 introduces a steering balancing control for moving stage. The control capacity analyses, the DOA estimates, and the switching control design

are presented in Section 3.4. Section 3.5 demonstrates the experimental results and provides the control performance analysis. Section 3.6 gives the conclusion of the works in this chapter.

3.2 Stationary balancing by gyro-balancer

This section focuses on the stationary bicycle balancing by the gyro pivoting control. First, an orbits constructing method is proposed, and then the orbit regulation controller with stability analysis is demonstrated. Finally, the control system performance is shown by the experiment results.

3.2.1 Orbits construction

Under conditions $v_r = 0$ and $\phi = 0$, the bikebot dynamics (2.9) and (2.10) reduce to

$$\left(m_b h_b^2 + J_b + I_z \,\mathrm{s}_{\varphi_w}^2 + \frac{I_z}{2}\,\mathrm{c}_{\varphi_w}^2\right)\ddot{\varphi}_b - m_b h_b g\,\mathrm{s}_{\varphi_b} + I_z\left(\omega_s - \frac{1}{2}\dot{\varphi}_b\,\mathrm{s}_{\varphi_w}\right)\mathrm{c}_{\varphi_w}\,\dot{\varphi}_w = 0, \quad (3.1)$$

and

$$\frac{I_z}{2}\ddot{\varphi}_w + \frac{I_z}{2}\,\mathrm{c}_{\varphi_w}\,\mathrm{c}_{\varphi_w}\,\dot{\varphi}_b^2 - \frac{1}{2}I_z\omega_s\,\mathrm{c}_{\varphi_w}\,\dot{\varphi}_b = \tau_p. \quad (3.2)$$

Noticing (3.2) without the coupling term of $\ddot{\varphi}_b$, the pivoting angular velocity $\dot{\varphi}_w$ can be easily controlled to track the desired trajectories through a lower level tracking controller. Thus, these dynamics can be modified into a 3-dimensional system as

$$\dot{x}_1 = x_2 \quad (3.3a)$$

$$\dot{x}_2 = f(\boldsymbol{x}) + g_1(\boldsymbol{x})u_1 \quad (3.3b)$$

$$\dot{x}_3 = u_1, \quad (3.3c)$$

with the states $\boldsymbol{x} = [x_1, x_2, x_3]^T = [\varphi_b, \dot{\varphi}_b, \mathrm{s}_{\varphi_w}]^T$, the control input $u_1 = \mathrm{c}_{\varphi_w}\,\dot{\varphi}_w$, and

$$f(\boldsymbol{x}) = \frac{m_b g h_b\,\mathrm{s}_{x_1}}{m_b h_b^2 + J_b + I_z\,\mathrm{s}_{\varphi_w}^2 + \frac{I_z}{2}\,\mathrm{c}_{\varphi_w}^2}, g_1(\boldsymbol{x}) = -\frac{I_x x_2\,\mathrm{s}_{2x_3} + I_z\omega_s}{m_b h_b^2 + J_b + I_z\,\mathrm{s}_{\varphi_w}^2 + \frac{I_z}{2}\,\mathrm{c}_{\varphi_w}^2}.$$

Due to the mechanical structure constraints, the pivoting φ_w and $\dot{\varphi}_w$ are bounded as

$$|x_3| = |\,\mathrm{s}_{\varphi_w}\,| \le \mathrm{s}_{\varphi_w^{\max}} < 1, |u_1| = |\,\mathrm{c}_{\varphi_w}\,\dot{\varphi}_w| \le \omega_w^{\max}$$

with the maximum pivoting angle and angular velocity as $\varphi_w^{\max}$ and $\omega_w^{\max}$, respectively. The equilibrium of the dynamics (3.3) is $x_{1e} = x_{2e} = 0$ under $\dot{\varphi}_{we} = 0$.

Furthermore, the rolling dynamics (3.2) satisfies

$$\frac{d}{dt}\left[(m_b h_b^2 + I_x)x_2 + I_x x_1 x_3^2 + I_z \omega_s x_3\right] = -\frac{\partial}{\partial x_1}\left(m_b g h_b \, \mathrm{c}_{x_1}\right) \tag{3.4}$$

with the angular momentum along the x-axis as

$$p_x(t) = (m_b h_b^2 + I_x)x_2(t) + I_{wxz} x_2(t) x_3^2(t) + I_{wz}\omega_s x_3(t). \tag{3.5}$$

By integrating (3.4), the angular momentum is

$$p_x(t) - p_x(0) = \int_0^t m_b g h_b \, \mathrm{s}_{x_1(\tau)} \, d\tau. \tag{3.6}$$

Thus, the following property is introduced.

Property 3.1. *For a given periodic profile $x_1(t)$ with period T, the profile for the pivoting angle is also periodic with the same period.*

Proof. Given an arbitrary periodical orbit $x_1(t+T) = x_1(t)$ for any t, $x_2(t) = \dot{x}_1(t)$ is also periodic with period T, i.e., $x_2(t+T) = x_2(t)$. And then, the following relationships are obtained

$$p_x(t+T) - p_x(0) = \int_0^{t+T} m_b g h_b \, \mathrm{s}_{x_1(\tau)} \, d\tau$$

and

$$p_x(t+T) - p_x(t) = \int_0^{T} m_b g h_b \, \mathrm{s}_{x_1(\tau)} \, d\tau. \tag{3.7}$$

Under periodical $x_1(t)$ and $x_2(t)$, $\int_0^T \mathrm{s}_{x_1(\tau)} \, d\tau = 0$. Therefore, (3.4) reduces to

$$\left[x_3(t+T) - x_3(t)\right]\left[I_{wz}\omega_s + I_{wxz}(x_3(t+T) + x_3(t))\right] = 0.$$

Thus, $x_3(t+T) = x_3(t)$ and φ_w is also periodic with period T. □

In the following, the orbits construction method based on energy shaping mechanism is demonstrated. First, the rolling dynamics (3.3b) is simplified, considering the facts that $\omega_s \gg |x_2|$, $I_z \omega_s \, \mathrm{c}_{x_3} \gg |I_x x_2 \, \mathrm{s}_{2x_3}|$ and $m_b h_b^2 \gg I_x$. Thus,

$$\dot{x}_2 - \frac{g}{h_b}\, \mathrm{s}_{x_1} + \frac{I_z \omega_s}{m_b h_b^2} u_1 = 0, \tag{3.8}$$

with $\boldsymbol{x} \in \mathcal{D} := \mathbb{S} \times \mathbb{R} \times (-1, 1)$. The desired bicycle rolling orbit $\mathcal{O}_b$ is then designed as the following simple pendulum dynamics profile as

$$\mathcal{O}_b : \ \dot{x}_2 + \frac{b}{h_G} \mathrm{s}_{x_1} = 0 \tag{3.9}$$

with a gravitationally equivalent constant $b > 0$ and a given initial value x_{10}. When the rolling states x_1 and x_2 are on $\mathcal{O}_b$, the controlled x_3 has to satisfy the relationship as

$$\dot{x}_3 = -\frac{(b+g)m_b h_b^2}{I_{wz} b \omega_s} \dot{x}_2 = -L\dot{x}_2 \tag{3.10}$$

with constant $L = \frac{(g+b)m_b h_b^2}{I_z b \omega_s}$. For obtaining the large control actuator pivoting range, the desired flywheel pivoting orbit $\mathcal{O}_w$ is designed as the integration of (3.10) with zero initial values. Therefore, $\mathcal{O}_w$ is designed as

$$\mathcal{O}_w : \ x_3 = -Lx_2, \tag{3.11}$$

which can be also considered as a virtual constraint for the system states x_1 and x_3.

In fact, the orbits structures (3.9) and (3.11) provide a family of orbits with the same dynamics form. To determine the final orbits, the initial states values are needed. Here, the defined energy function is introduced for choosing a unique orbit in $\mathcal{O}_b$, that is, the total energy under the defined b, as

$$E(x_1, x_2) = \frac{1}{2} m_b h_b^2 x_2^2 + m_b h_b b \left(1 - \mathrm{c}_{x_1}\right). \tag{3.12}$$

When target orbit $\mathcal{O}_b$ reaches the maximum angle x_1^d with $x_2 = 0$, the total energy is $E_d = m_b h_b b(1 - \mathrm{c}_{x_1^d})$. Thus, the dynamics (3.9) and (3.11) with E_d generate a unique orbits couple $\mathcal{O}_b$ and $\mathcal{O}_w$.

Remark 3.1. *The proposed orbits construction process is similar as the classic method in [53,56]. However, there are two main differences comparing these two strategies, which are dominated by the special dynamics form of the bikebot system. First, the construction steps are not the same. In the proposed method, the orbit shape, as (3.9), is designed firstly, and the virtual constraint (3.11) is obtained using the orbit shape. That is, the*

energy shaping progress is to determine the dynamics to a desired form. Contrary to the presented approach, the method in [53, 56] takes a reverse order in design. Second, the virtual constraints are not the same. The proposed method is a linear relationship between the angular velocity $\dot{\varphi}_b$ and the angular position φ_w, not as that among the position states. That is due to the dynamics model structure. The coupling term is only in the centripetal-Coriolis torque, but not in the potential and acceleration terms.

3.2.2 Orbital regulation controller design

For regulating the system states on the desired orbits, the control law is proposed as follows. The control input u_1 is designed as

$$u_1 = \frac{Lb}{h_b}\left(\mathrm{s}_{x_1} + v_1\right). \tag{3.13}$$

And the auxiliary control input v_1 defined as

$$v_1 = k_2\left[\Delta E x_2 + \alpha k_1\left(x_3 + L x_2\right)\right], \tag{3.14}$$

with constant $\alpha = \frac{g}{bI_z\omega_s}$ and the energy difference $\Delta E = E(x_1, x_2) - E_d$ under given desired E_d.

Property 3.2. *Starting at a given non-zero state $\boldsymbol{x}_0$, state $\boldsymbol{x}$ of dynamics (3.3) and (3.8) can be asymptotically regulated onto the desired orbits (3.9) and (3.11) with desire E_d, under the designed controller (3.13) and (3.14).*

Proof. The positive defined Lyapunov candidate function $V_1(\boldsymbol{x})$ is designed as follows

$$V_1(\boldsymbol{x}) = \frac{1}{2}\Delta E^2 + \frac{1}{2}k_1\left(x_3 + L x_2\right)^2 \tag{3.15}$$

with the positive constant k_1. Its time derivative is

$$\dot{V}_1(\boldsymbol{x}) = \Delta E(m_b h_b^2 x_2 \dot{x}_2 + m_b h_b b \mathrm{s}_{x_1} x_2) + k_1(x_3 + L x_2)(\dot{x}_3 + L\dot{x}_2). \tag{3.16}$$

Substituting the dynamics (3.3b) and the designed controller (3.13), (3.16) becomes

$$\dot{V}_1(\boldsymbol{x}) = -m_b h_b (g + b)\left[\Delta E x_2 + \alpha k_1\left(x_3 + L x_2\right)\right] v_1. \tag{3.17}$$

Considering v_1 structure in (3.14), $\dot{V}_1(\boldsymbol{x})$ is not greater than zero, as

$$\dot{V}_1(\boldsymbol{x}) = -m_b h_b (g+b) k_2 \left[\Delta E x_2 + \alpha k_1 \left(x_3 + L x_2\right)\right]^2 \leq 0. \tag{3.18}$$

Based on (3.18), according to LaSalle theory [58], $\boldsymbol{x}$ can be proven to converge to the invariant set $\mathcal{S}(\boldsymbol{x})$ asymptotically,

$$\mathcal{S}(\boldsymbol{x}) = \left\{\boldsymbol{x} \in \mathcal{D} \,|\Delta E x_2 + \alpha k_1 \left(x_3 + L x_2\right) = 0\right\}. \tag{3.19}$$

It is obvious that the origin point is in the set, as $\boldsymbol{x}_e = \mathbf{0} \in \mathcal{S}(\boldsymbol{x})$. At this point, $\dot{\boldsymbol{x}} = \mathbf{0}$. For any none zero states point in $\mathcal{S}(\boldsymbol{x})$, the auxiliary control input v_1 is zero, and the desired orbit dynamics (3.9) is satisfied. That is, the energy difference ΔE is a constant value, and integrating from (3.10), the virtual constraint value of $x_3 + L x_2$ is constant.

If $\Delta E \neq 0$, considering non-constant x_2 on (3.10), with the constant $x_3 + L x_2$, the equation $v_1 = 0$ can not be satisfied. It exists a contradiction. Thus, $\Delta E = 0$ and the set $\mathcal{O}_w = \mathcal{S}(\boldsymbol{x}) \setminus \{\mathbf{0}\}$ also satisfies

$$\mathcal{O}_w(\boldsymbol{x}) = \left\{\boldsymbol{x} \in \mathcal{D} \,|\Delta E = 0,\, x_3 + L x_2 = 0\right\}. \tag{3.20}$$

That is equivalent to the desired $\mathcal{O}_b$ and $\mathcal{O}_w$ with $E = E_d$. □

3.3 Balancing control by steering actuation

We consider to use steering actuation to balance the platform under moving velocity $v_r > 0$. From the bikebot dynamics, the balance torque τ_s generated by steering is calculated as

$$\tau_s = \left(k_{p1} + k_{p2}\phi_t\right)\phi_t + k_d u_s \tag{3.21}$$

with $\phi_t := \tan\phi$, and $u_s := \dot{\phi}_t$ as the controlled steering angular velocity. $k_{p1} = \frac{m_b h_b \, \mathrm{c}_\xi}{l}(v_r^2 - v_c^2)$, $v_c = \sqrt{\frac{g l_b l_t \, \mathrm{c}_\xi}{h_b}}$, $k_{p2} = -\frac{m_b h_b^2 v_r^2 \, \mathrm{c}_\xi^2 \tan\varphi_b}{l}$ and $k_d = \frac{m_b h_b l_b v_r \, \mathrm{c}_\xi}{l}$. Note that the sign of parameter k_{p1} depends on the velocity v_r and $k_d > 0$. It is straightforward to obtain that with increasing steering angle ϕ and velocity v_r, the torque τ_s value grows as well. It is noted that when bikebot velocity v_r is small, the value of torque τ_s is small. Because of this

observation, it is extremely challenging to use steering actuation to balance the platform when v_r is small. Therefore, the following design is for relative large velocity $v_r \geq v_c$.

Using the feedback linearization, the steering control input u_s can be designed as same as the EIC-based control strategy [14] and also in Chapter 4. For a given moving trajectory, we can calculate the balance equilibrium manifold and let φ_{be} denote the desired roll angle. The balance errors are denoted as $e_{\varphi_b} = \varphi_b - \varphi_{be}$, $\dot{e}_{\varphi_b} = \dot{\varphi}_b - \dot{\varphi}_{be}$, and $\ddot{e}_{\varphi_b} = \ddot{\varphi}_b - \ddot{\varphi}_{be}$. Under fixed flywheel pivoting $\varphi_w = \dot{\varphi}_w = 0$ and $\omega_s = 0$, $u_w = 0$, (2.9) is approximately reduced to

$$J_t \ddot{\varphi}_b \approx f_s - k_d u_s,$$

with $f_s = m_b g h_b s_{\varphi_b} - k_{p1} \tan\phi - k_{p2} \tan^2\phi$, $J_t = m_b h_b^2 + J_b + I_z$ and the approximation of u_ψ as $u_\psi \approx \frac{v_r \, c_\xi}{l \, c_{\varphi_b}} u_s$. The steering control input u_s is designed as

$$u_s = \frac{1}{k_d} \left[f_s + J_t (c_1 \dot{e}_{\varphi_b} + c_0 e_{\varphi_b}) \right], \tag{3.22}$$

where constants $c_1, c_2 > 0$. The closed-loop dynamics is then $\ddot{e}_{\varphi_b} + c_1 \dot{e}_{\varphi_b} + c_0 e_{\varphi_b} = 0$, which is obviously asymptotically stable.

3.4 Balance switching control laws

In this section, we present the balance capacity and comparison between the gyro-balancer and the steering actuation first. The main goal of this comparison is to explain and justify the use of each of these two actuators for balance control. From this analysis, it becomes clear that the gyro-balancer can effectively be used for stationary bikebot balance (small steering-induced torque), while the steering balance torque would dominate the gyro-balance torque at relatively large moving velocities. Because of this observation, we consider that at stationary or low velocity, the balance is maintained by the gyro-balance only and at relatively large velocities, only steering balance is used. For a complete design, a switching control strategy is needed, that is, the gyro-balancer and steering actuation are used for balance control at different velocity ranges. The switching conditions are determined by the control capacity of each actuation. The estimated DOA is an effective

measure for quantifying control capacity.

3.4.1 Balancing actuation capacity comparison

We consider the following physical actuation limits for flywheel and steering motions: $|\varphi_w(t)| \leq \varphi_w^{\max} < \frac{\pi}{2}$, $|\dot{\varphi}_w| \leq \omega_w^{\max}$, $|\ddot{\varphi}_w(t)| \leq \gamma_w^{\max}$, $|\phi(t)| \leq \phi_s^{\max} < \frac{\pi}{2}$, $|\dot{\phi}(t)| \leq \omega_s^{\max}$, $|\ddot{\phi}(t)| \leq \gamma_s^{\max}$, where $\varphi_i^{\max}$, $\omega_i^{\max}$, and $\gamma_i^{\max}$, $i = w, s$, are the constants of maximum position, velocity, and acceleration for the flywheel pivoting and steering actuations, respectively.

From (2.9), the gyro-balancer torque τ_g is

$$\tau_g = I_z \, \mathrm{c}_{\varphi_w} \left(\omega_s - \frac{1}{2}\dot{\varphi}_b \, \mathrm{s}_{\varphi_w} - \frac{1}{2}\dot{\psi} \, \mathrm{c}_{\varphi_b} \, \mathrm{c}_{\varphi_w} \right) \left(\dot{\varphi}_w + \dot{\psi} \, \mathrm{s}_{\varphi_b} \right). \tag{3.23}$$

Considering that $\dot{\varphi}_b$ can be neglected comparing with ω_s for small φ_b and $\dot{\varphi}_b$, the gyro-balancer torque $\tau_g(t)$ is approximated as $\tau_g(t) \approx I_z \omega_s \, \mathrm{c}_{\varphi_w} \, \dot{\varphi}_w$ and the maximum instantaneous torque amplitude is $|\tau_g|^{\max} = I_z \omega_s \omega_w^{\max}$. Under this approximation, over a time interval $[t_1, t_2]$, the impulse of τ_g is obtained as

$$I_g(t_1, t_2) = \int_{t_1}^{t_2} \tau_g(\nu) d\nu = I_z \omega_s \, \mathrm{s}_{\varphi_w} \Big|_{t_2}^{t_1}.$$

It is straightforward that $|I_g|^{\max} = 2 I_z \omega_s s_{\varphi_w^{\max}}$. The value of $I_g(t_1, t_2)$ only depends on the pivoting angles $\varphi_w(t_1)$ and $\varphi_w(t_2)$. By $\varphi_w^{\max}$, $\omega_w^{\max}$ and $\gamma_w^{\max}$, we can obtain the smallest time duration $\Delta t = t_2 - t_1$ for providing $|I_g|^{\max}$ and the average torque $\bar{\tau}_g$.

Under $\varphi_b = 0$ and a constant ϕ, from (3.21), the steering-induced balance torque τ_s is

$$\tau_s = \frac{m_b h_b \, \mathrm{c}_\xi}{l} (v_r^2 - v_c^2) \tan \phi.$$

It is clear from the above result that the value of torque τ_s increases with increasing velocity v_r and steering angle ϕ. Moreover, comparing with torque τ_g generated by the gyro-balancer with a short time duration Δt ($= 0.5$ s for the bikebot), the steering-induced torque τ_s is more persistent and can last for long time. Moreover, the magnitude of τ_g is also larger than that of $\tau_s^{\max}$ (around 20 Nm) under significant velocity v_r.

3.4.2 DOA Estimates

We give an estimation of the DOA estimate $\mathcal{D}_1(\boldsymbol{x})$ under the gyro-balancer control (3.13) and (3.14). From the previous analysis in Section 3.2, under $\boldsymbol{x} = \mathbf{0}$, $V_1(\mathbf{0}) = \frac{1}{2}E_d^2$. With the non-increasing $\dot{V}_1(\boldsymbol{x})$, for converging onto the desired orbits $\mathcal{O}_b$ and $\mathcal{O}_w$, a conservative estimation $\mathcal{D}_1(\boldsymbol{x})$ is obtained as

$$\mathcal{D}_1(\boldsymbol{x}) = \left\{ \boldsymbol{x} \in \mathbb{R}^3 \,|\, V_1(\boldsymbol{x}) \leq \frac{1}{2}E_d^2 \right\}. \tag{3.24}$$

For an given initial pivoting angle φ_{w0}, the set $\mathcal{D}_1(\boldsymbol{x})$ in the φ_b-$\dot{\varphi}_b$ plane can be calculated and plotted. We introduce $\mathcal{D}_w \subset [-\frac{\pi}{2}, \frac{\pi}{2}] \times \mathbb{R}$ as the projected set of $\mathcal{D}_1(\boldsymbol{x})$ onto the φ_b-$\dot{\varphi}_b$ plane, namely,

$$\mathcal{D}_w = \{(x_1, x_2) \mid \boldsymbol{x} \in \mathcal{D}_1(\boldsymbol{x}) \text{ for a given } x_3\}. \tag{3.25}$$

The above set indeed covers all trajectory of $(\varphi_b(t), \dot{\varphi}_b(t)) \in \mathcal{D}_w$ from a given initial condition $\varphi_w(0)$ under the gyro-balancer control u_w. We plot the boundary of $\mathcal{D}_w$ to illustrate the controllable range.

Under a given speed v_r, the DOA estimate $\mathcal{D}_s \subset [-\frac{\pi}{2}, \frac{\pi}{2}] \times \mathbb{R}$ of the steering controller (3.22) is dominated by variables $\phi_s^{\max}$, $\dot{\phi}_s^{\max}$ and $\gamma_s^{\max}$. It is difficult to explicitly obtain a closed-form calculation under these motion limits. We use the computational approach to obtain an estimation of $\mathcal{D}_s$ by finding the maximum initial states $(\varphi_{b0}, \dot{\varphi}_{b0})$ to maintain a stable trajectory under given control parameters.

The above calculated DOA estimates $\mathcal{D}_w$ and $\mathcal{D}_s$ are under specific gyro-balancer and steering controllers. In the following, we introduce sets $\boldsymbol{\Omega}_w$, $\boldsymbol{\Omega}_s \subset [-\frac{\pi}{2}, \frac{\pi}{2}] \times \mathbb{R}$ for the gyro-balancer and steering actuations, respectively, under any possible controllers. In other words, if the initial state $(\varphi_{b0}, \dot{\varphi}_{b0}) \notin \boldsymbol{\Omega}_w$, $\boldsymbol{\Omega}_s$, the bikebot cannot be balanced respectively under any gyro-balancer and steering controllers.

To simplify the analysis, the linearized closed-loop dynamics under the gyro-balancer and steering actuation controls are given respectively as

$$\Sigma_g : \qquad \ddot{\varphi}_b - k^2\varphi_b + k_g u_w/J = 0, \tag{3.26}$$

$$\Sigma_s : \qquad \ddot{\varphi}_b - k^2\varphi_b + k_{p1}\phi_t/J + k_d u_s/J = 0, \tag{3.27}$$

where constants $J = m_b h_b^2 + J_b$, $k = \sqrt{J^{-1} m_b g h_b}$, and $k_g = I_z \omega_s$. For a given initial values $\varphi_b(0) = \varphi_{b0}$ and $\dot{\varphi}_b(0) = \dot{\varphi}_{b0}$, the solutions for Σ_g and Σ_s are

$$\varphi_b(t) = I_I(\varphi_{b0}, \dot{\varphi}_{b0}, t) + I_C(u_i, [0,t]),\ i = s, w. \tag{3.28}$$

The initial and input terms in (3.28) are given as

$$I_I(\varphi_{b0}, \dot{\varphi}_{b0}, t) = k_{e1}(t)\varphi_{b0} + k_{e2}(t)\dot{\varphi}_{b0}, \tag{3.29}$$

$$I_C(u_s, [0,t]) = \frac{1}{J}\int_0^t k_{e2}(t-s)(k_{p1}\phi_t(s) + k_d u_s(s))ds, \tag{3.30}$$

$$I_C(u_w, [0,t]) = \frac{1}{J}\int_0^t k_{e2}(t-s) k_g u_w(s) ds, \tag{3.31}$$

where $k_{e1}(t) = \frac{e^{kt}+e^{-kt}}{2}$ and $k_{e2}(t) = \frac{e^{kt}-e^{-kt}}{2k}$. Noting that $\dot{\phi}_t = u_s$, it is straightforward to obtain $I_C(-u_i, [0,t]) = -I_C(u_i, [0,t])$ for $i = s, w$.

We denote inputs $u_s^*(t)$ and $u_w^*(t)$ profiles as to drive $\phi(t)$ and $\varphi_w(t)$ from zero their maximum values $\phi_s^{\max}$ and $\varphi_w^{\max}$ as fast as possible respectively, and then hold them at the maximum values afterward. Let us denote the times to reach their maximum values under $u_s^*(t)$ and $u_w^*(t)$ as t_s^* and t_w^*, respectively. In (3.28), $k_{e2}(t)$ is increasing function with t, $k_{p1} > 0$, $k_g > 0$, and $k_d > 0$. We present and prove the following property.

Property 3.3. *For any given $u_i(t)$, $i = s, w$, under aforementioned physical actuation limits, for $t > 0$, $I_C(u_i, [0,t])$ is bounded as*

$$|I_C(u_i, [0,t])| \le I_C(u_i^*, [0,t]), i = s, w. \tag{3.32}$$

Proof. Considering the similar structures of $I_C(u_i, [0,t])$ for u_s and u_w, we only give the proof of the property (3.32) for u_s. The $\phi_t^*(t)$ is noted as the control steering angular position under $u_s^*(t)$, and $\phi_t(t)$ is under a given $u_s(t)$.

From the definition of $u_s^*(t)$, the signal $\phi_t^*(t)$ is generated. Compared to any arbitrary control input $u_s(t)$, we have the relationship as

$$-\phi_t^*(t_x) \le \phi_t(t_x) \le \phi_t^*(t_x) \tag{3.33}$$

which is equal to

$$-\int_0^{t_x} u_s^*(s)\,ds \le \int_0^{t_x} u_s(s)\,ds \le \int_0^{t_x} u_s^*(s)\,ds \tag{3.34}$$

for any time point t_x. With $k_{e2}(t) > 0, \forall t > 0$, we have the inequality about $u_s(t)$ as

$$\left|\int_0^t k_{e2}(t-s)\,\phi_t(s)\,ds\right| \le \int_0^t k_{e2}(t-s)\,\phi_t^*(s)\,ds. \tag{3.35}$$

And then, we focus on the second convolution term $\int_0^t k_{e2}(t-s)\,u_s(s)\,ds$ of the control term $I_C(u_s,[0,t])$. We define the signal difference $v_s(s)$ as

$$v_s(s) = u_s^*(s) - u_s(s), s \ge 0. \tag{3.36}$$

Naturally, considering $u_s^*(0) = u_s(0)$, $v_s(0) = 0$. And because of the bounded $\dot{\phi}_s$ and γ_s, $v_s(s)$ is 2-ordered differentiable w.r.t. s. For simply expression, we introduced two integrals as

$$M(t_1,t_2) = \int_{t_1}^{t_2} v_s(s)\,ds, \forall 0 \le t_1 < t_2 \le t, \tag{3.37}$$

and

$$E(t_1,t_2) = \int_{t_1}^{t_2} k_{e2}(t-s)\,v_s(s)\,ds, \forall 0 \le t_1 < t_2 \le t. \tag{3.38}$$

Naturally, $M(t_1,t_2) + M(t_2,t_3) = M(t_1,t_3)$ and $E(t_1,t_2) + E(t_2,t_3) = E(t_1,t_3)$ with $\forall 0 \le t_1 \le t_2 \le t_3 \le t$. Besides, from (3.34), we have

$$M(0,t_1) \ge 0, \forall 0 \le t_1 \le t. \tag{3.39}$$

Because of the 2-ordered differentiable $v_s(s)$. That is, in the time interval $(0,t)$, there exists a open time interval array, noted as $(a_1,b_1),(a_2,b_2),\cdots(a_k,b_k),\cdots$, with $a_1 \ge 0$. And any two of these intervals have no intersection. A set $S_{>0} \subset [0,t]$ is introduced as

$$S_{>0} = (a_1,b_1) \cup (a_2,b_2) \cup \cdots \cup (a_k,b_k) \cup \cdots .$$

When $s \in S_{>0}$, $v_s(s) > 0$. And if $s \notin S_{>0}$ and $s \in (0,1)$, $v_s(s) \le 0$.

From (3.39), $M(0,a_1) = 0$. Combining with $v_s(s) \le 0, \forall s \in (0,a_1)$, $v_s(s) = 0, \forall s \in (0,a_1)$. That is, $E(0,a_1) = 0$. $E(0,a_2)$ can be divided as

$$E(0,a_2) = E(0,a_1) + E(a_1,b_1) + E(b_1,a_2). \tag{3.40}$$

Since the positive $k_{e2}(t-s)$ is strictly decreasing w.r.t. s, $v_s(s) \leq 0, s \in (b_1, a_2)$, and $v_s(s) > 0, s \in (a_1, b_1)$, we have the following inequality

$$\begin{array}{l} E\left(0, a_2\right) > M\left(0, a_1\right) + k_{e2}\left(t - b_1\right) M\left(a_1, b_1\right) \\ + k_{e2}\left(t - b_1\right) M\left(b_1, a_2\right) \end{array}. \tag{3.41}$$

Thus,

$$E\left(0, a_2\right) > k_{e2}\left(t - b_1\right) M\left(0, a_2\right) > 0. \tag{3.42}$$

Similarly, for the interval $(0, a_3)$, we have

$$E\left(0, a_3\right) = E\left(0, a_2\right) + E\left(a_2, b_2\right) + E\left(b_2, a_3\right), \tag{3.43}$$

and

$$\begin{array}{l} E\left(0, a_3\right) > k_{e2}\left(t - b_1\right) M\left(0, a_2\right) + \\ k_{e2}\left(t - b_2\right) M\left(a_2, b_2\right) + k_{e2}\left(t - b_2\right) M\left(b_2, a_3\right) \end{array}. \tag{3.44}$$

Therefore,

$$E\left(0, a_3\right) > k_{e2}\left(t - b_2\right) M\left(0, a_3\right) > 0. \tag{3.45}$$

Supposing

$$E\left(0, a_k\right) > k_{e2}\left(t - b_{k-1}\right) M\left(0, a_k\right),$$

we can deduce an inequality about $E(0, a_{k+1})$ as

$$E\left(0, a_{k+1}\right) > k_{e2}\left(t - b_k\right) M\left(0, a_{k+1}\right) > 0. \tag{3.46}$$

Using this process iteratively to the end, we have

$$E\left(0, t\right) > 0.$$

With (3.38), we have the bounded convolution value as

$$\int_0^t k_{e2}\left(t - s\right) u_s\left(s\right) ds \leq \int_0^t k_{e2}\left(t - s\right) u_s^*\left(s\right) ds. \tag{3.47}$$

Symmetrically, we also can conclude

$$-\int_0^t k_{e2}\left(t - s\right) u_s^*\left(s\right) ds \leq \int_0^t k_{e2}\left(t - s\right) u_s\left(s\right) ds. \tag{3.48}$$

Finally, combining the relationships (3.47) and (3.48) about $u_s^*(s)$ and the relationship (3.35) about $\phi_t^*(s)$, we proved the bounded relationship (3.32) about $u_s^*(t)$. The (3.32) about u_w^* can be obtained by the similar process. We omit the details here. □

Then, we give the definitions of the Ω_s and Ω_w as

$$\Omega_i\left(\varphi_b, \dot{\varphi}_b\right) = \left\{\left(\varphi_b, \dot{\varphi}_b\right) \mid \left|I_I\left(\varphi_b, \dot{\varphi}_b, t_i\right)\right| \leq I_C\left(u_i^*, [0, t_i]\right)\right\}, i = s, w. \tag{3.49}$$

The defined Ω_i has the following property as

Property 3.4. *Given an initial states point $(\varphi_{b0}, \dot{\varphi}_{b0})$ at $t = 0$, if $(\varphi_{b0}, \dot{\varphi}_{b0}) \notin \Omega_i$, the system can not be balanced under any control input u_i. If $(\varphi_{b0}, \dot{\varphi}_{b0}) \in \Omega_i$, there exist a control input, noted as u_i^*, under which, the system can be balanced.*

Proof. Considering that the balancing task is to let $\varphi_b(t) \to 0$ as $t \to 0$, the exponential converging factor e^{-kt} can be neglected. Then the term $I_I(\varphi_b, \dot{\varphi}_b, t)$ can be rewritten as

$$I_I\left(\varphi_{b0}, \dot{\varphi}_{b0}, t\right) = \frac{e^{kt}}{2}\varphi_{b0} + \frac{e^{kt}}{2k}\dot{\varphi}_{b0}.$$

Naturally, we have

$$I_I\left(\varphi_{b0}, \dot{\varphi}_{b0}, t\right) = e^{k(t-t_i)} I_I\left(\varphi_{b0}, \dot{\varphi}_{b0}, t_i\right). \tag{3.50}$$

Based on the u_i^* definitions, we have $u_i^*(t) = 0, t > t_i$. Similarly, since $u_i^*(t) = 0, t > t_i$, and neglecting the e^{-kt} term, $I_C(u_i^*, t)$ can be approximated as

$$I_C\left(u_i^*, [0, t]\right) = e^{k(t-t_i)} I_C\left(u_i^*, [0, t_i]\right), t > t_i. \tag{3.51}$$

Combining with Property 3.3, for any given u_i, $I_C(u_i, [0, t])$ is bounded as

$$-e^{k(t-t_i)} I_C\left(u_i^*, [0, t_i]\right) \leq I_C\left(u_i, [0, t]\right) \leq e^{k(t-t_i)} I_C\left(u_i^*, [0, t_i]\right). \tag{3.52}$$

If $(\varphi_{b0}, \dot{\varphi}_{b0})$ satisfies the relationship as

$$I_I\left(\varphi_{b0}, \dot{\varphi}_{b0}, t_i\right) > I_C\left(u_i^*, [0, t_i]\right), \tag{3.53}$$

combining with (3.52) and (3.27), we have

$$\varphi_b\left(t\right) \geq e^{k(t-t_i)}\left(I_I\left(\varphi_{b0}, \dot{\varphi}_{b0}, t_i\right) - I_C\left(u_i^*, [0, t_i]\right)\right) > 0.$$

That is, with $e^{k(t-t_i)}$, φ_b has to diverges, under any arbitrary control u_i. Symmetrically, If $(\varphi_{b0}, \dot{\varphi}_{b0})$ satisfies the relationship as

$$I_I\left(\varphi_{b0}, \dot{\varphi}_{b0}, t_i\right) < -I_C\left(u_i^*, [0, t_i]\right), \tag{3.54}$$

combining (3.52) with (3.27), we have

$$\varphi_b\left(t\right) \leq e^{k(t-t_i)}\left(I_I\left(\varphi_{b0}, \dot{\varphi}_{b0}, t_i\right) + I_C\left(u_i^*, t_i\right)\right) < 0.$$

That is, φ_b also diverges. Therefore, from the solution under initial condition (3.53) and (3.54), with $(\varphi_{b0}, \dot{\varphi}_{b0}) \notin \Omega_i$ and any control u_i, φ_b has to diverge.

If $(\varphi_{b0}, \dot{\varphi}_{b0}) \in \Omega_i$, and we note that $B_i = I_I(\varphi_{b0}, \dot{\varphi}_{b0}, t_i)$. Naturally, we have

$$-I_C(u_i^*, t_i) \leq B_i \leq I_C(u_i^*, t_i).$$

Besides, the value of $I_C(ku_i, t)$ is continuous about k. That is, there exists $k_i \in [-1, 1]$ to satisfy that

$$I_C(k_i u_i^*, t_i) = -B_i.$$

We noted the desired control u_i^d as $u_i^d = k_i u_i^*$. Under u_i^d, the exponential growing term in φ_b can be eliminated, as

$$e^{k(t-t_i)}\left(I_I\left(\varphi_{b0}, \dot{\varphi}_{b0}, t_i\right) + I_C\left(u_i^d, t_i\right)\right) = 0.$$

That is, $\varphi_b(t)$ will converge to zero under control u_i^d. □

3.4.3 Switching Strategy

We now discuss the switching control during the stationary-to-moving maneuver for the bikebot. From stationary to moving conditions, the control laws switch by velocity v_r values. The switching velocity is denoted as v_{s1} at t_{s1} and from the previous analysis, the velocity v_{s1} has to satisfy the condition

$$\mathcal{D}_w(t_{s1}) \subseteq \mathcal{D}_s(t_{s1}).$$

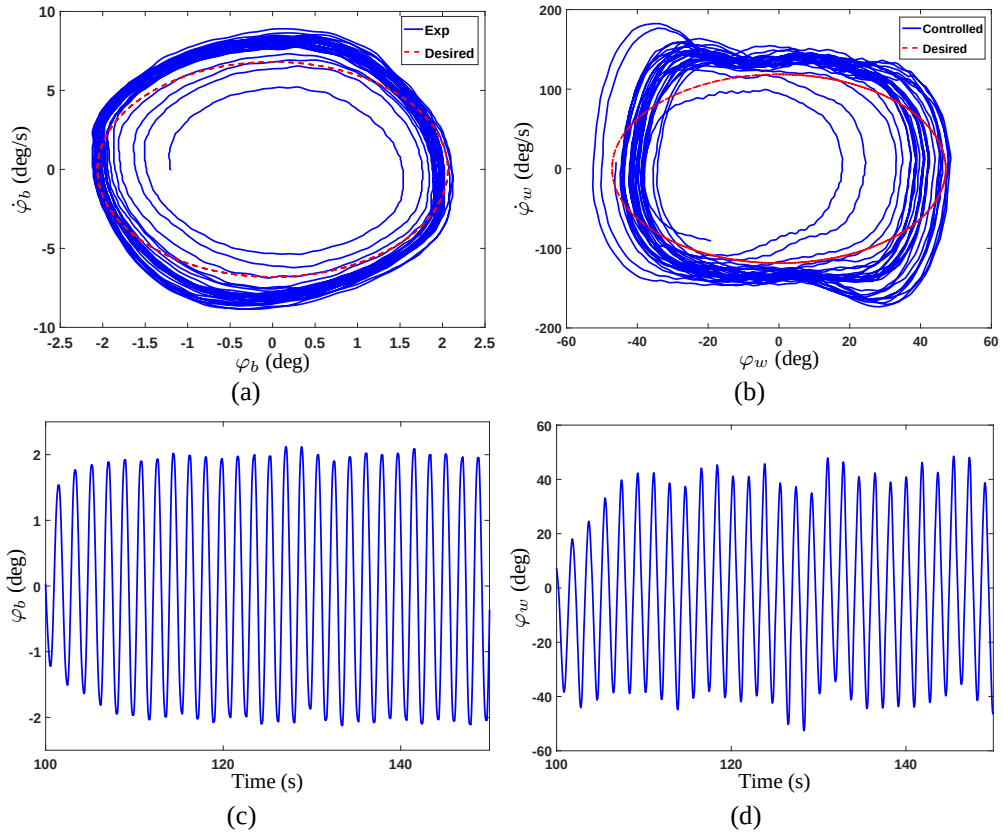

Figure 3.1: Gyro-balancer orbital regulation results. (a) Bikebot rolling trajectory on φ_b-$\dot{\varphi}_b$ phase plan. (b) Flywheel pivoting trajectory on φ_w-$\dot{\varphi}_w$ phase plan. (c) Bikebot roll angle φ_b trajectory. (d) Flywheel pivoting angle φ_w trajectory.

To switch the control from u_s (under the steering balance) to u_w (under the gyro-balancer), that is, from moving-to-stationary transition, we consider the switching velocity at v_{s2} with time t_{s2}. The condition that needs to be satisfied is given as $(\varphi_b(t_{s2}), \dot{\varphi}_b(t_{s2})) \in \mathcal{D}_w$. In this case, the gyro-balancer controller can balance the system with a zero steering angle ϕ. However, in practice, this condition is difficult to satisfy under zero steering angle, particularly under possibly disturbances. We will present experimental results and discussion in the next section.

3.5 Experiments results

We first demonstrate the stationary balance control performance under the orbital stabilization control u_w. The values of the major bikebot parameters are $m_b = 37.5$ kg, $h_b = 0.64$

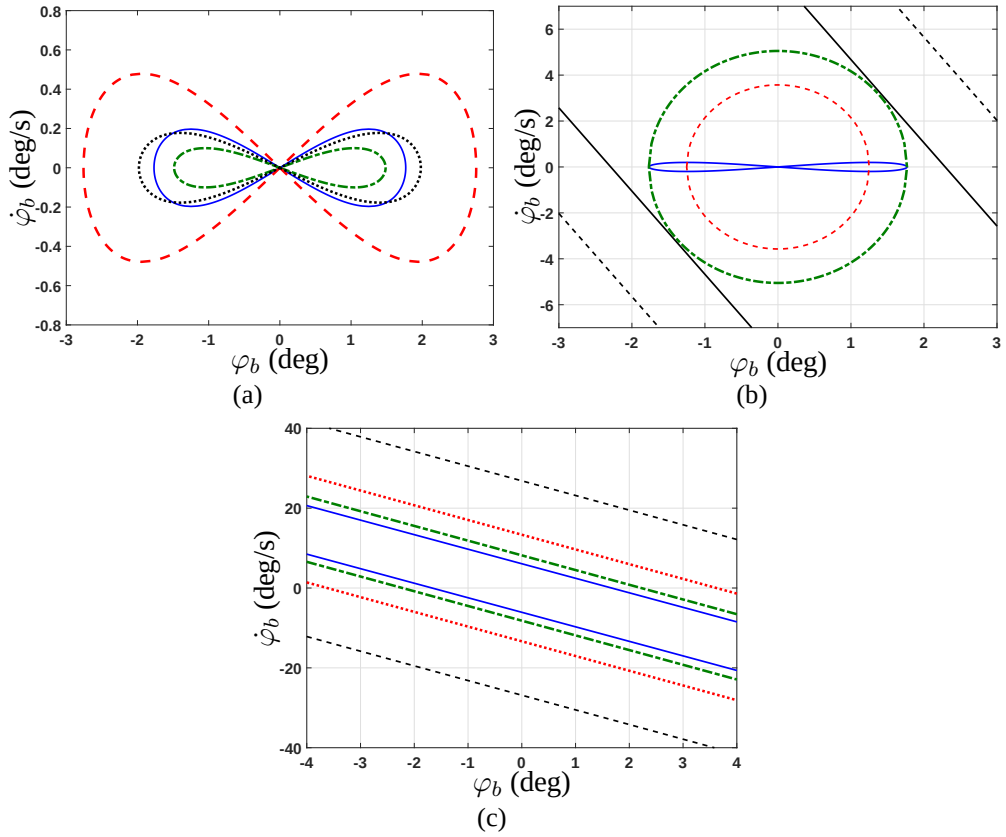

Figure 3.2: The DOA plots of the gyro-balancer and steering balance controls. (a) The DOA plots under gyro-balancer orbital regulation control u_w with initial condition $\varphi_{w0} = 0$ and various parameters. Blue: $m_b = 55$ kg, $\omega_s = 1500$ rpm, $h_b = 0.64$ m; Green: $m_b = 42$ kg, $\omega_s = 1500$ rpm, $h_b = 0.64$ m; Red: $m_b = 55$ kg, $\omega_s = 1200$ rpm, $h_b = 0.64$ m; Black: $m_b = 55$ kg, $\omega_s = 1200$ rpm, $h_b = 0.48$ m. (b) The DOA plots of the gyro-balancer control u_w and steering control u_s. (c) Plots of $\mathbf{\Omega}_w$ and $\mathbf{\Omega}_s$. Blue: boundary of $\mathbf{\Omega}_w$ at $m_b = 55$ kg and $\omega_s = 1500$ rpm; Green, red and black: boundaries of $\mathbf{\Omega}_s$ under $v_r = 0.75$ m/s, $v_r = 1.00$ m/s and $v_r = 1.50$ m/s.

m and $\omega_s = 1500$ rpm. Figs. 3.1(a) and 3.1(b) show the phase portraits of the φ_b-$\dot{\varphi}_b$ and φ_w-$\dot{\varphi}_w$, while Figs. 3.1(c) and 3.1(d) show the roll angle φ_b and pivoting angle φ_w profiles. The desired roll angle orbits reach to ± 2 deg. The bikebot is released at $\varphi_{b0} = -1.2$ deg and $\dot{\varphi}_{b0} = 0$ deg/s with $\varphi_{w0} = 0$. From Fig. 3.1(c), after several periods, the bike roll angle profiles converge to the desired roll orbit $\mathcal{O}_b$. This is clearly shown in Fig. 3.1(a). When the rolling motion reaches the desired orbit, the flywheel pivoting motion is also near the pivoting orbit, as shown in Fig. 3.1(b). The flywheel pitching trajectory is within the range of ± 50 deg as shown in Fig. 3.1(d).

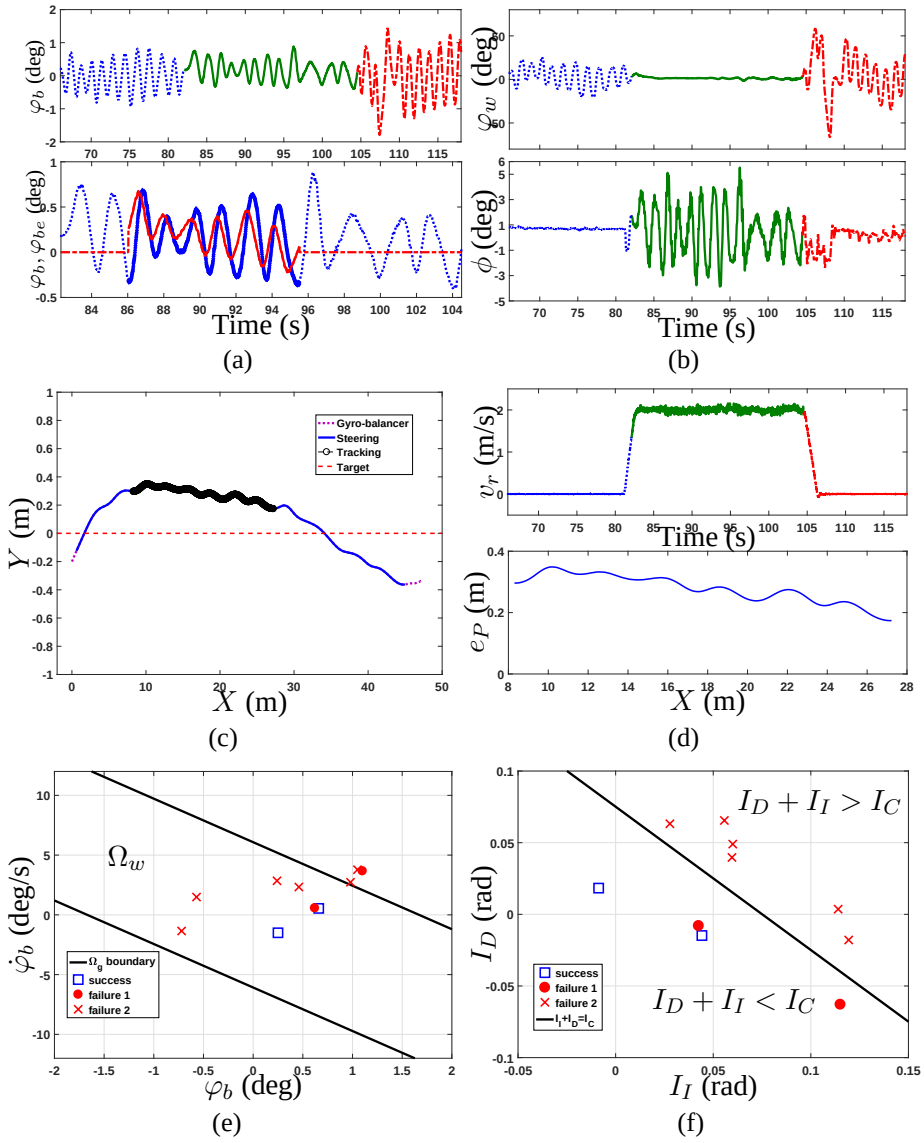

Figure 3.3: Switched balance control results. (a) Bikebot roll angle φ_b and target roll angle φ_{be}. (Top-figure: blue and red curves under u_w and green curve under u_s; Bottom-figure: blue and red curves are the roll angle $\varphi_b(t)$ and the desired $\varphi_{be}(t)$, respectively. The solid and dash lines portion represent the only balancing and balancing-tracking,respectively. (b) Flywheel pivoting angle φ_w and steering angle ϕ. Blue and red portion under u_w control and the green portion under u_s control.) (c) Bikebot planar position (X, Y). Purple dash, blue solid, and black square portions are under u_w, u_s, and EIC-based velocity-steering control (u_v, u_s), respectively. The red dash line is the target path. (d) Bikebot velocity v_r and path following error e_P. For the top-figure, blue and red portion are under u_w and u_s controls, respectively. (e) State variable $(\varphi_b(t_{s2}), \dot{\varphi}_b(t_{s2}))$ on the φ_b-$\dot{\varphi}_b$ plane. Blue squares, red circles, red crosses marks are for the success, failure with $|I_I + I_D| \leq I_C$, failure with $|I_I + I_D| > I_C$ cases, respectively. The black lines are the boundary of $\mathbf{\Omega}_w$. (f) Running conditions in the I_I-I_D plane. Blue squares, red circles, and red crosses are for the success, failure with $|I_I + I_D| \leq I_C$, failure with $|I_I + I_D| > I_C$ cases, respectively. The black line represents $I_I + I_D = I_C$.

Fig. 3.2(a) shows the sets boundaries of $\mathcal{D}_w$ at various combinations of parameter m_b, h_b and ω_s. From these plots, we observe that the smaller m_s, smaller h_b, or larger ω_s values, the DOA estimates $\mathcal{D}_w$ become larger. Under the outdoor experiment condition (i.e., $m_b = 55$ kg, $h_b = 0.64$ m and $\omega_w = 1500$ rpm, the blue curve in Fig. 3.2(a)), the estimated maximum controllable roll angle by gyro-balancer control u_w is less than 1.7 deg. That region is also plotted in Fig. 3.2(b) and is bounded by blue curve. If the initial roll states $(\varphi_{b0}, \dot{\varphi}_{b0}) \in \mathcal{D}_w$, controller u_w can drive the state to converge to orbit $\mathcal{O}_b$ (i.e., red circle). Fig. 3.2(b) also shows the plot of $\mathcal{D}_s$ under different velocity v_r values. For $v_r = 0.85$ (black solid lines) and 1 m/s (black dash lines), the regions $\mathcal{D}_s$ increases in size. If $v_r \geq 0.85$ m/s, DOA region $\mathcal{D}_w$ under u_w is covered by $\mathcal{D}_s$ under u_s. Fig. 3.2(c) shows the boundaries of largest DOAs $\mathbf{\Omega}_s$ and $\mathbf{\Omega}_w$ under various velocity values. With increased v_r, region $\mathbf{\Omega}_s$ is enlarged. When $v_r \geq 0.75$ m/s, $\mathbf{\Omega}_w \subset \mathbf{\Omega}_s$. Comparing with $\mathcal{D}_s$ in Fig. 3.2(b), for a given v_r, $\mathbf{\Omega}_s$ is almost at the same size as that of $\mathcal{D}_s$.

We also run stationary-to-moving-to-stationary experiments under the switching control between u_w and u_s. During the second moving phase, the bikebot is commanded to track a straight-line trajectory under the EIC-based steering control u_s, and the first and third transition phases, balancing is the only target under u_w. Fig. 3.3 shows the performance of one experimental run results. The stationary-to-moving transition are from 66.2 s to 81.6 s and the moving-to-stationary duration is from 106.3 s to 118.5 s. The path following portion is therefore from 86.1 s to 95.5 s. The balanced roll angle profiles are plotted in Fig. 3.3(a). In the first and third portions, the bikebot experiences the periodical swing motions in the range about $[-1, 1]$ deg under the orbital stabilization control u_w. In the middle portion, under steering control u_s, roll angle is within the range of $[-1,\ 1]$ deg. Moreover, the roll angle tracks the desired trajectory $\varphi_{be}(t)$ by the EIC design. The gyro-balancer pivoting and steering angle control inputs are shown in Fig. 3.3(b). Fig. 3.3(c) shows the bikebot planar position and the position errors are held within ± 0.4m as shown in Fig. 3.3(d). The switching velocities are designed at $v_{s1} = 1.2$ m/s and $v_{s2} = 1.9$ m/s and v_{s1} satisfies the DOA analysis.

The challenging task in experiments is to keep balancing the system during moving-to-stationary transition. Out of ten experimental runs, only two were successful and the rest eight failed. At the switching moment t_{s2}, the condition of $(\varphi_b(t_{s2}), \dot{\varphi}_b(t_{s2})) \in \mathcal{D}_w$ is critical. We conduct a similar DOA analysis to find out the condition. Supposing that $\phi(t) = 0, t > t_a := t_{s2} + t_w^*$. Similar to the analysis to obtain the results in (3.49), if $|I_I(\varphi_b(t_{s2}), \dot{\varphi}_b(t_{s2})) + I_C(u_s, [t_{s2}, t_a])| > I_C(u_w^*, [t_{s2}, t_a])$, there does not exist a $u_w(t)$ for the convergence of $\varphi_b(t)$, that is, a success balance condition in this case is

$$|I_I + I_D| \leq I_C, \tag{3.55}$$

where initial state term $I_I = I_I(\varphi_b(t_{s2}), \dot{\varphi}_b(t_{s2}))$, disturbance term $I_D = I_C(u_s, [t_{s2}, t_a])$, and control term $I_C = I_C(u_w^*, [t_{s2}, t_a])$. The calculation of these terms is given by (3.29)-(3.31).

We take the 10 experimental runs data to check condition (3.55). Fig. 3.3(e) shows the initial states $(\varphi_b(t_{s2}), \dot{\varphi}_b(t_{s2}))$ in the phase portrait. The region of $\mathbf{\Omega}_w$ is also plotted in the figure. We found that 7 runs are in $\mathbf{\Omega}_w$, including the two successful runs. Fig. 3.3(f) further shows the initial state values in the I_I-I_D plane. In this figure, if $I_I + I_D < 0$, the point $(-I_I, -I_D)$ is instead plotted for the absolute value. The curve $I_I + I_D = I_C$ is also plotted in the figure. It is clearly shown that only 4 experiment runs satisfy the condition (3.55) and two of them are successful (marked by the blue squares). The other two runs with $I_I + I_D \leq I_C$ still cannot balance (marked by the red circles). The possible explanation for this result could come from two reasons. First, the region $\mathbf{\Omega}_w$ is much larger than $\mathcal{D}_w$. Thus, there exists the states which could be balanced by u_w^* but not by the orbital stabilization control u_w. Second, the estimation of steering disturbance I_D is not precise under small v_r values. In this case, it is possible that some experimental runs fail even if condition (3.55) is satisfied. Nevertheless, the results in Fig. 3.3(f) confirm that the condition works for most cases.

3.6 Conclusion

This chapter presented a stationary balance control law, a moving balance control law, and an integrated balance control of autonomous bikebot system in complete stationary-to-moving maneuvers. Gyro-balance and steering actuation are two main effective control strategies for stationary and moving cases respectively. We analyzed the DOA of the closed-loop systems under these two control designs and then built on the DOA analysis, a safety control strategy was designed for stationary-to-moving maneuvers. We conducted extensive experiments to illustrate and demonstrate the analysis and design. The results validated the effectiveness of the switching control strategies.

From theoretical analysis and experiments results, the proposed switching control seems not robust enough for handling large disturbances in practical experiments. We plan to relax some assumptions in the analysis and develop a combined gyro-balancer and steering control strategy to enhance the balance performance in future.

Chapter 4
Bikebot Autonomous Tracking Control

4.1 Introduction

Underactuated balancing systems such as bicycles or motorcycles provide a unique platform to train and treat human with postural balance disabilities [38, 59]. Balancing control of the bikebot is presented in Chapter 3. To further understand and tune the characteristics of human balance motor skills in these unstable physical human-robot interactions, it is desirable to design and build an autonomous trajectory tracking and balancing capability for the bikebot system.

Trajectory tracking control of a riderless autonomous bicycle (or motorcycle) has also been proposed and studied in [11, 13, 17, 41–43, 60]. Steering and velocity control are the main two actuations for the autonomous bicycles or motorcycles designs except that in [17, 60], additional mechanisms such as weight-shifting are used to assist the balance of the systems. Although many above-mentioned research work discuss the motion control of autonomous bicycles, few experimental results and demonstration have been reported. The results of the Blue team in the 2005 DARPA Challenge confirm the difficulties to achieve accurately trajectory tracking and balance control of autonomous single-track vehicles [13]. One of the research goals of this chapter is to demonstrate the experiments of trajectory tracking and balancing of autonomous bikebot using steering and velocity control.

Understanding the human sensorimotor mechanism in the physical unstable rider-bicycle interaction is studied in recent work in [12, 29, 30]. Modeling and pose estimation of the rider-bicycle interactions are reported in [26, 27, 61]. To further identify the human control strategies quantitatively, the research work in [21, 22] present the human upper-body

movement and steering control models and their influences on platform balance. Bikebot is utilized in the work presented in [21, 22]. The use of the gyro-balancer as an additional actuation helps the balance of the stationary bikebot [20] and also enables the further tuning of human motor skills through the physical rider-bikebot interactions. Another goal of this work is to integrate the gyro-balancer design into the trajectory-tracking and balancing control.

In this chapter, a trajectory tracking and balance control law is first presented. With the steering and velocity control, the bikebot can track a target trajectory autonomously. The controller design is built on an extension of the EIC structure of the nonlinear dynamics of the bikebot system [11, 41]. The EIC-based control is modified and implemented to achieve both trajectory-tracking and platform-balancing tasks. The control design is then extended by incorporating the gyro-balancer actuation to further enhance the control performance. The use of additional gyro-balancer torque further reduces the position tracking error and the performance improvement is also guaranteed by design. The control systems designs are validated and demonstrated by experiments.

To our best knowledge, there is no reported experimental demonstration for the precise and successful trajectory tracking and balance control of autonomous bicycles or motorcycles. The experiments in [42, 62] and other demonstrations only show the balance capability of controlled bicycle or motorcycle systems and trajectory tracking is not among the control tasks. Indeed, from control systems design viewpoint, trajectory tracking and platform balancing are two competing tasks. Other studies (e.g., [11, 17, 43]) do not include experimental demonstration and validation. The EIC-based control with inclusion of the gyro-balancer design complements the human rider control strategies developed in literature [21, 22, 29, 30]. The control design in this chapter also enables the use of bikebot for control of physical human-robot interactions. Although the chapter focuses on the bikebot, the proposed control systems approach can be applied to other underactuated balancing systems, such as pole-cart, Furuta pendulum, or biped walkers, etc.

The remainder of this chapter is organized as follows. The control laws are designed

in Section 4.2. The theoretical analysis for this control system stability and performance is demonstrated in Section 4.3. The designed experiments are presented in Section 4.4. The concluding remarks are discussed in Section 4.5.

4.2 EIC-based controller design

The bikebot dynamics in (2.9) and (2.12) can be converted into an nearly EIC form. The nearly EIC form of a nonlinear dynamical system is an extension of the EIC form introduced in [11].

Definition 4.1. *An $n(=m+p)$-dimensional nonlinear control system is called in an* nearly external/internal convertible form *if the system is of the form*

$$\Sigma: \begin{cases} \dot{x}_i = x_{i+1},\ \dot{x}_m = u, i = 1, \cdots, m-1, \\ \dot{\alpha}_j = \alpha_{j+1}, \\ \dot{\alpha}_p = f(\boldsymbol{x}, \boldsymbol{\alpha}) + g(\boldsymbol{x}, \boldsymbol{\alpha})u + g_i(\boldsymbol{x}, \boldsymbol{\alpha})u_i, \\ y = x_1,\ j = 1, \cdots, p-1, \end{cases} \tag{4.1}$$

with inputs $u, u_i \in \mathbb{R}$, output $y \in \mathbb{R}$, state variables $(\boldsymbol{x}, \boldsymbol{\alpha})$, with $\boldsymbol{x} = [x_1 \cdots x_m]^T \in \mathbb{R}^m$ and $\boldsymbol{\alpha} = [\alpha_1 \cdots \alpha_p]^T \in \mathbb{R}^p$. Functions $f(\boldsymbol{x}, \boldsymbol{\alpha})$, $g(\boldsymbol{x}, \boldsymbol{\alpha})$ and $g_i(\boldsymbol{x}, \boldsymbol{\alpha})$ are smooth and $g(\boldsymbol{x}, \boldsymbol{\alpha}) \neq 0$ for all $(x, \alpha) \in \mathbb{B}_r \subset \mathbb{R}^{n+p}$ is an open ball. Moreover, we refer to the external subsystem *of Σ as*

$$\Sigma_{\text{ext}}: \ \dot{x}_i = x_{i+1},\ \dot{x}_m = u,\ i = 1, \cdots, m-1, \tag{4.2}$$

and the internal subsystem *of Σ as*

$$\Sigma_{\text{int}}: \ \dot{\alpha}_i = \alpha_{i+1},\ \dot{\alpha}_p = f(\boldsymbol{x}, \boldsymbol{\alpha}) + g(\boldsymbol{x}, \boldsymbol{\alpha})u + g_i(\boldsymbol{x}, \boldsymbol{\alpha})u_i, \tag{4.3}$$

for $i = 1, \cdots, p-1$.

Fig. 4.1 shows the structure of the nearly EIC system. The nearly EIC system Σ is *convertible* because Σ_{int} is nearly converted to Σ_{ext} (with an addition internal control u_i

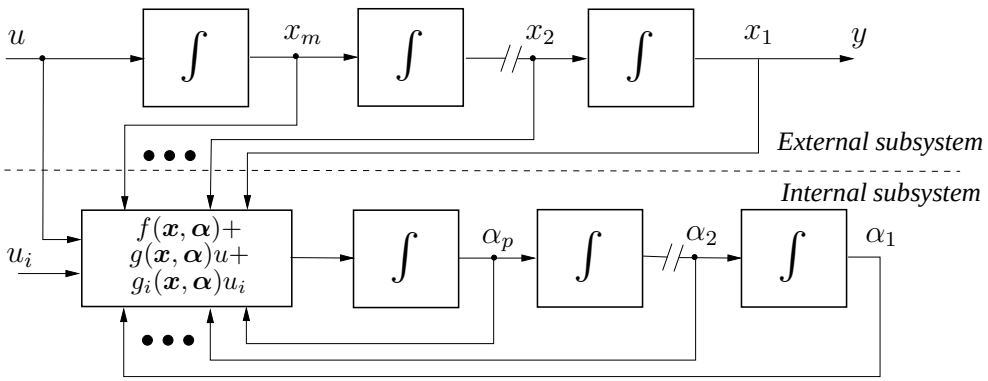

Figure 4.1: A nearly external/internal convertible system.

term), and Σ_{ext} is nearly converted to Σ_{int} (again with an addition internal control u_i term) under a simple transformation $u = g(\boldsymbol{x}, \boldsymbol{\alpha})^{-1}[v - f(\boldsymbol{x}, \boldsymbol{\alpha})]$. To see this dual-structure property, defining $\xi = \alpha_1$ as the dual output and applying the above transformation to Σ (4.1), we obtain the *dual* of $\Sigma(u)$.

$$\Sigma_d : \begin{cases} \dot{x}_i = x_{i+1}, \dot{x}_m = -g^{-1}(\boldsymbol{x}, \boldsymbol{\alpha}) f(\boldsymbol{x}, \boldsymbol{\alpha}) + g^{-1}(\boldsymbol{x}, \boldsymbol{\alpha}) v, \\ \dot{\alpha}_j = \alpha_{j+1}, \dot{\alpha}_p = v + g^{-1}(\boldsymbol{x}, \boldsymbol{\alpha}) g_i(\boldsymbol{x}, \boldsymbol{\alpha}) u_i, \\ \xi = \alpha_1, i = 1, \cdots, m-1, j = 1, \cdots, p-1. \end{cases} \tag{4.4}$$

The bikebot rolling dynamics (2.9) can be rewritten as

$$J_t \ddot{\varphi}_b = f(\varphi_b) + g_\psi(\varphi_b) u_\psi + g_w u_w, \tag{4.5}$$

with $J_t = m_b h_b^2 + J_b + I_z(1 + \mathrm{s}_{\varphi_w}^2)/2$, $f(\varphi_b) = -m_b h_b \,\mathrm{c}_{\varphi_b}\, v_r \dot{\psi} + m_b h_b^2 \,\mathrm{c}_{\varphi_b}\, \mathrm{s}_{\varphi_b}\, \dot{\psi}^2 + m_b h_b g \,\mathrm{s}_{\varphi_b} + I_z \,\mathrm{c}_{\varphi_w}\, \mathrm{s}_{\varphi_b}\, \dot{\psi}(\omega_s - \dot{\varphi}_b \,\mathrm{s}_{\varphi_w}/2 - \dot{\psi}\,\mathrm{c}_{\varphi_b}\,\mathrm{c}_{\varphi_w}/2) + \frac{m_b g l_t l_b \tan\phi \,\mathrm{c}_\xi \,\mathrm{c}_{\varphi_b}}{l}$, $g_w = -I_z(\omega_s - \dot{\varphi}\,\mathrm{s}_{\varphi_w}/2 - \dot{\psi}\,\mathrm{c}_{\varphi_b}\,\mathrm{c}_{\varphi_w}/2)\,\mathrm{c}_{\varphi_w}$, and $g_\psi(\varphi_b) = -m_b h_b l_b \,\mathrm{c}_{\varphi_b}$. The equivalent control inputs for rolling are u_ψ and $u_w = \dot{\varphi}_w$. Combining with (2.12) and (4.5), the EIC form of this system is

$$\Sigma_{\text{ext}} \quad : \quad \boldsymbol{r}_{C_2}^{(3)} = \boldsymbol{u}_N, \tag{4.6a}$$

$$\Sigma_{\text{int}} \quad : \quad \ddot{\varphi} = J_t^{-1}\left[f(\varphi_b) + g_\psi(\varphi_b) u_\psi + g_w u_w\right]. \tag{4.6b}$$

For a given desired trajectory $\mathcal{T}$:$(X_d(t), Y_d(t))$, we design a linear feedback controller for Σ_{ext} [22]

$$\boldsymbol{u}_N^{\text{ext}} = \boldsymbol{r}_d^{(3)} - b_2\ddot{\boldsymbol{e}}_p - b_1\dot{\boldsymbol{e}}_p - b_0\boldsymbol{e}_p, \tag{4.7}$$

and $\boldsymbol{u}^{\text{ext}} = \boldsymbol{R}_\psi^{-1}\left(\boldsymbol{\Psi} + \boldsymbol{u}_N^{\text{ext}}\right)$, where $\boldsymbol{r}_d = [X_d(t), Y_d(t)]^T$, error $\boldsymbol{e}_p(t) = [e_X, e_Y]^T = \boldsymbol{r}_{C_2} - \boldsymbol{r}_d$, and $\boldsymbol{r}_d^{(3)}$ denotes the third derivative of $\boldsymbol{r}_d$. The control gains b_i, $i = 0, 1, 2$, are chosen to guarantee that $s^3 + b_2 s^2 + b_1 s + b_0 = 0$ is Hurwitz. Under (4.7), the external vector field $\mathbf{N}_{ext}$ is defined as

$$\mathbf{N_{ext}} := \begin{bmatrix} \dot{X}(t) \\ \ddot{X}(t) \\ X_d^{(3)} - \Sigma_{i=0}^2 b_i e_X^{(i)} \\ \dot{Y}(t) \\ \ddot{Y}(t) \\ Y_d^{(3)} - \Sigma_{i=0}^2 b_i e_Y^{(i)} \end{bmatrix}. \tag{4.8}$$

Using control design (4.7), the BEM is defined as

$$\mathcal{E} = \left\{ (\boldsymbol{x}, \varphi_{be}) \,\middle|\, \varphi_b = \varphi_{be}(\dot{\psi}, v_r, \boldsymbol{u}^{ext}, \varphi_w), \dot{\varphi}_b = \ddot{\varphi}_b = 0 \right\}, \tag{4.9}$$

where $\boldsymbol{x} = [\boldsymbol{r}_{C_2}^T\, \dot{\boldsymbol{r}}_{C_2}^T\, \ddot{\boldsymbol{r}}_{C_2}^T]^T$ and $\boldsymbol{\alpha} = [\varphi_b\, \dot{\varphi}_b]^T$. In (4.9), the roll angle equilibrium $\varphi_{be} = \varphi_{be}(\dot{\psi}, v_r, \boldsymbol{u}^{\text{ext}}, \varphi_w)$ is the solution of the following equation (under $u_\psi = u_\psi^{\text{ext}}$ and $u_w = 0$)

$$\boldsymbol{F}(\varphi_{be}, \dot{\psi}, v_r, \boldsymbol{u}, \varphi_w) = f(\varphi_b) + g_\psi(\varphi_b) u_\psi^{\text{ext}} = 0. \tag{4.10}$$

The derivatives $\dot{\varphi}_{be}$ and $\ddot{\varphi}_{be}$ can be approximated by the directional derivatives along $\mathbf{N_{ext}}$ with $u_w = 0$ as

$$\bar{L}_{\mathbf{N_{ext}}}\varphi_{be} = L_{\mathbf{N_{ext}}}\varphi_e + \frac{\partial \varphi_{be}}{\partial t}, \bar{L}^2_{\mathbf{N_{ext}}}\varphi_{be} = \bar{L}_{\mathbf{N_{ext}}}\bar{L}_{\mathbf{N_{ext}}}\varphi_{be}.$$

If the gyro-balancer is not actuated, that is, $u_w = 0$, the internal system controller is designed as

$$u_\psi^{\text{int}} = g_\psi^{-1}(\varphi_b)(-f(\varphi_b) + J_t v_\psi^{\text{int}}) \tag{4.11}$$

where

$$v_\psi^{\text{int}} = \bar{L}^2_{N_{ext}}\varphi_{be} - a_1\dot{e}_{\varphi_b} - a_0 e_{\varphi_b} \tag{4.12}$$

with the tracking errors definitions $e_{\varphi_b} = \varphi_b - \varphi_{be}$, $\dot{e}_{\varphi_b} = \dot{\varphi}_b - \dot{\varphi}_{be} \approx \dot{\varphi}_b - \bar{L}_{\mathbf{N_{ext}}}\varphi_{be}$, and $a_0, a_1 > 0$. Under this u_ψ^{int}, the closed-loop error dynamics for Σ_{int} is $\ddot{e}_\varphi + a_1\dot{e}_\varphi + a_0 e_\varphi = 0$ and asymptotically stable. Therefore, without using the gyro-balancer actuation, the controller is

$$\mathcal{C}: \; u_r = u_r^{\text{ext}}, u_\psi = u_\psi^{\text{int}}, u_w = 0. \tag{4.13}$$

The gyro-balancer pivoting control u_w and the modified $\bar{u}_\psi^{\text{int}}$ are designed in the following. According to the EIC control structure, under control input $\boldsymbol{u}^{\text{ext}} = [u_r^{\text{ext}} \;\; u_\psi^{\text{ext}}]^T$, the bikebot position $(X(t), Y(t))$ converges to the desired trajectory $\mathcal{T}$ exponentially. However, for the balancing task, the steering input u_ψ^{int} is different from u_ψ^{ext} and thus introduces position tracking errors $\boldsymbol{e}_p$. On the other hand, u_ψ^{int} has to tune roll angle φ_b to follow equilibrium φ_{be}. The goal of the gyro-balancer control u_w is to assist platform balancing under $\bar{u}_\psi^{\text{int}}$. We consider that under the combined u_w and $\bar{u}_\psi^{\text{int}}$, the balancing capability is the same as u_ψ^{int} in (4.11) and thus

$$J_t v_\psi^{\text{int}} = f(\varphi_b) + g_\psi(\varphi_b) u_\psi^{\text{int}} = f(\varphi_b) + g_\psi(\varphi_b)\bar{u}_\psi^{\text{int}} + g_w u_w. \tag{4.14}$$

Under $\boldsymbol{u}^{\text{ext}}$ (4.7) and $\boldsymbol{u}^{\text{ext}} = \boldsymbol{R}_\psi^{-1}(\boldsymbol{\Psi} + \boldsymbol{u}_N^{\text{ext}})$, the position tracking closed-loop dynamics is

$$\boldsymbol{r}_d^{(3)} - b_2\ddot{\boldsymbol{e}}_p - b_1\dot{\boldsymbol{e}}_p - b_0\boldsymbol{e}_p = \boldsymbol{\Psi} + \boldsymbol{R}_\psi \begin{bmatrix} u_r^{\text{ext}} \\ u_\psi^{\text{ext}} \end{bmatrix}. \tag{4.15}$$

On the other hand, from (4.6a) and control (4.7),

$$\boldsymbol{r}_c^{(3)} = \boldsymbol{\Psi} + \boldsymbol{R}_\psi \begin{bmatrix} u_r^{\text{ext}} \\ u_\psi^{\text{int}} \end{bmatrix} \tag{4.16}$$

and subtracting (4.15) from (4.16), the real closed loop tracking system is

$$\boldsymbol{e}_p^{(3)} + b_2\ddot{\boldsymbol{e}}_p + b_1\dot{\boldsymbol{e}}_p + b_0\boldsymbol{e}_p = \boldsymbol{d}_p := \boldsymbol{R}_\psi \begin{bmatrix} 0 \\ u_\psi^{\text{int}} - u_\psi^{\text{ext}} \end{bmatrix}. \tag{4.17}$$

Using the BEM definition (4.9), u_ψ^{ext} can be rewritten in terms of φ_{be} as

$$u_\psi^{\text{ext}} = -g_\psi^{-1}(\varphi_{be}) f(\varphi_{be}). \tag{4.18}$$

Substituting u_ψ^{int} in (4.6) and u_ψ^{ext} in (4.18) into (4.17), the error disturbance $\boldsymbol{d}_p$ becomes

$$\boldsymbol{d}_p = \boldsymbol{R}_\psi \begin{bmatrix} 0 \\ d_0 \end{bmatrix}, \tag{4.19}$$

where $d_0 = u_\psi^{\text{int}} - u_\psi^{\text{ext}} = -g_\psi^{-1}(\varphi_b)f(\varphi_b) + g_\psi^{-1}(\varphi_{be})f(\varphi_{be}) + g_\psi^{-1}(\varphi_b)J_t v_\psi^{\text{int}}$. Under the new control input $\bar{u}_\psi^{\text{int}}$ and u_r^{ext}, the error disturbance $\bar{\boldsymbol{d}}_p$ can be obtained as

$$\bar{\boldsymbol{d}}_p = \boldsymbol{R}_\psi \begin{bmatrix} 0 \\ \bar{d}_0 \end{bmatrix} = \boldsymbol{R}_\psi \begin{bmatrix} 0 \\ \bar{u}_\psi^{\text{int}} - u_\psi^{\text{ext}} \end{bmatrix}, \tag{4.20}$$

where $\bar{d}_0 = -g_\psi^{-1}(\varphi_b)f(\varphi_b) + g_\psi^{-1}(\varphi_{be})f(\varphi_{be}) + g_\psi^{-1}(\varphi_b)J_t v_\psi^{\text{int}} - g_\psi^{-1}(\varphi_b)g_w u_w$.

From (4.20), if the steering control is designed as $\bar{u}_\psi^{\text{int}} = u_\psi^{\text{ext}}$, then $\bar{\boldsymbol{d}}_p = \boldsymbol{0}$ and therefore the position errors $\boldsymbol{e}_p$ converge to zero exponentially by (4.17). However, because of (4.14) and the restrictively pivoting motion of the gyro-balancer, the magnitude of $\bar{u}_\psi^{\text{int}}$ cannot be arbitrarily chosen. In the following, the controller for u_w and $\bar{u}_\psi^{\text{int}}$ is proposed by considering the physical constraints of the gyro-balancer actuator. As mentioned in Chapter 3, the gyro-balancer pivoting motion is constrained by the hardware limitation. According to these constraints, the upper- and lower-boundary functions $f_{wc}^+(\varphi_w)$ and $f_{wc}^-(\varphi_w)$ for u_w are designed, that is, $f_{wc}^-(\varphi_w) \le u_w \le f_{wc}^+(\varphi_w)$, where

$$f_{wc}^+(\varphi_w) = \begin{cases} \omega_w^{\max} & -\varphi_w^{\max} \le \varphi_w \le \varphi_{w1} \\ 2\gamma_w^{\max}\sqrt{\varphi_w^{\max} - \varphi_w} & \varphi_{w1} < \varphi_w \le \varphi_w^{\max} \end{cases}$$

and $f_{wc}^-(\varphi_w) = -f_{wc}^+(-\varphi_w)$, with $\varphi_{w1} = \varphi_w^{\max} - \frac{(\omega_w^{\max})^2}{2\gamma_w^{\max}}$.

If $|d_0| > b_\psi$ for a given boundary $b_\psi > 0$, we design the rolling torque $g_w u_w$ in the direction of $g_\psi(u_\psi^{\text{int}} - u_\psi^{\text{ext}})$ and given constraints $f_{wc}^+(\varphi_w)$ and $f_{wc}^-(\varphi_w)$, that is,

$$u_w = \operatorname{sgn}(u_w)\min\left(\left|g_w^{-1}g_\psi(|d_0| - b_\psi)\right|, \left|f_{wc}^{\pm}(\varphi_w)\right|\right), \tag{4.21}$$

where $\operatorname{sgn}(u_w) = \operatorname{sign}(g_w^{-1}g_\psi d_0)$. For the case of $d_0 \le b_\psi$, we choose $u_w = 0$. From (4.14), the steering control input $\bar{u}_\psi^{\text{int}}$ is obtained as

$$\bar{u}_\psi^{\text{int}} = g_\psi^{-1}(\varphi_b)\left[J_t v_\psi^{\text{int}} - f(\varphi_b) - g_w u_w\right]. \tag{4.22}$$

Remark 4.1. *Because of physical limitation of the gyro-balancer pivoting effects, the balancing actuation u_w itself might not be powerful enough to fully balance the platform. That is the main reason why utilizing u_w as an auxiliary control when $|d_0|$ is large. A practical scenario is that the desired trajectory has a sharp turning or the balancing platform faces strong disturbances in a short time interval. Because of the limited actuation, in most parts of the tracking process, the balancing performance mainly depends on the steering actuation.*

4.3 Stability analysis

Under the EIC-based control $\mathcal{C} : (u_r^{\text{ext}}, u_\psi^{\text{int}}, 0)$, the position tracking error is denoted as $\boldsymbol{e}_p$. With the additional gyro-balancer actuation, the control inputs and the position tracking error are denoted as $\bar{\mathcal{C}} : (u_r^{\text{ext}}, \bar{u}_\psi^{\text{int}}, u_w)$ and $\bar{\boldsymbol{e}}_p$, respectively. It can be shown that under the new control $\bar{\mathcal{C}}$, the magnitude of the tracking errors is reduced. To show this property, the following results are first demonstrated.

Property 4.1. *The magnitude of error disturbance $\bar{\boldsymbol{d}}_p$ under controller $\bar{\mathcal{C}}$ is not greater than that of $\boldsymbol{d}_p$ under controller $\mathcal{C}$.*

Proof. From (4.19) and (4.20), this property is equivalent to show $|\bar{d}_0| \leq |d_0|$. For the case of $|d_0| < b_\psi$, $u_w = 0$ is utilized, thus $|\bar{d}_0| = |d_0|$. Therefore $\left\|\bar{\boldsymbol{d}}_p\right\|_2 = \|\boldsymbol{d}_p\|_2$. For the case $|\bar{d}_0| > |d_0|$, we have

$$d_0 - \bar{d}_0 = u_\psi^{\text{int}} - \bar{u}_\psi^{\text{int}} = g_\psi^{-1}(\varphi) g_w u_w. \tag{4.23}$$

Form the sign and amplitude definition of u_w, we conclude the following relationships: $\operatorname{sgn}(d_0) = \operatorname{sgn}\left(g_\psi^{-1} g_w u_w\right)$ and $|g_\psi^{-1} g_w u_w| \leq |d_0| - b_\psi < |d_0|$. Therefore, under taking the absolute value of (4.23) without changing the form, the relationship $|d_0| - |\bar{d}_0| = |g_\psi^{-1} g_w u_w| > 0$ is obtained. □

Under controller $\bar{\mathcal{C}}$, the EIC structure and property are still held. Therefore, as shown in [11, 22], the closed-loop errors $\boldsymbol{e}_p$ and $\bar{\boldsymbol{e}}_p$ asymptotically converge to a bounded region

near origin. Similar to (4.17), the obtained dynamics for $\bar{\boldsymbol{e}}_p$ is

$$\bar{\boldsymbol{e}}_p^{(3)} + b_2\ddot{\bar{\boldsymbol{e}}}_p + b_1\dot{\bar{\boldsymbol{e}}}_p + b_0\bar{\boldsymbol{e}}_p = \bar{\boldsymbol{d}}_p. \tag{4.24}$$

Defining $\boldsymbol{e}_x = [\boldsymbol{e}_p^T, \dot{\boldsymbol{e}}_p^T, \ddot{\boldsymbol{e}}_p^T]^T$ and $\boldsymbol{e}_{\varphi_b} = [e_{\varphi_b}, \dot{e}_{\varphi_b}]^T$, similar to [11], the magnitudes of the disturbances $\boldsymbol{d}_p$ and $\bar{\boldsymbol{d}}_p$ are assumed to be affine function of $\boldsymbol{e}_x$ and $\bar{\boldsymbol{e}}_x$, respectively,

$$\|\boldsymbol{d}_p\|_2 \leq k_0 + k_1 \|\boldsymbol{e}_x\|_2, \ \left\|\bar{\boldsymbol{d}}_p\right\|_2 \leq \bar{k}_0 + \bar{k}_1 \|\bar{\boldsymbol{e}}_x\|_2, \tag{4.25}$$

where $\bar{\boldsymbol{e}}_x = [\bar{\boldsymbol{e}}_p^T, \dot{\bar{\boldsymbol{e}}}_p^T, \ddot{\bar{\boldsymbol{e}}}_p^T]^T$ and $k_0, k_1, \bar{k}_0, \bar{k}_1 > 0$ are positive constants. Because of the results in Property 4.1, it is assumed that

$$\bar{k}_0 \leq k_0, \ \bar{k}_1 \leq k_1. \tag{4.26}$$

The following results about errors $\boldsymbol{e}_p$ and $\bar{\boldsymbol{e}}_p$ are based on the following property.

Property 4.2. *Under controllers $\mathcal{C}$ and $\overline{\mathcal{C}}$, the position tracking errors $\boldsymbol{e}_p(t)$ and $\bar{\boldsymbol{e}}_p(t)$ exponentially converge to regions near the origin. Moreover, there exist error bounds $e_p^b(t)$ and $\bar{e}_p^b(t)$, that is, $\|\boldsymbol{e}_p(t)\| \leq e_p^b(t)$ and $\|\bar{\boldsymbol{e}}_p(t)\| \leq \bar{e}_p^b(t)$, then $\bar{e}_p^b(t) \leq e_p^b(t)$, for $\forall t \geq 0$.*

Proof. We prove the property through the Lyapunov stability theorem [58] and the results by Property 4.1. Using state variable $\boldsymbol{e}_x$, we re-write the error dynamics (4.17) as

$$\dot{\boldsymbol{e}}_x = \boldsymbol{A}\boldsymbol{e}_x + \boldsymbol{d}_p, \boldsymbol{A} = \boldsymbol{A}_0 \otimes \boldsymbol{I}_2, \boldsymbol{A}_0 = \begin{bmatrix} 0 & 1 & 0 \\ 0 & 0 & 1 \\ -b_0 & -b_1 & -b_2 \end{bmatrix}, \tag{4.27}$$

where operator $\otimes$ represents the Kronecker product and $\boldsymbol{I}_n \in \mathbb{R}^{n\times n}$ is the n-dimensional identity matrix.

The Lyapunov function $V = \boldsymbol{e}_x^T\boldsymbol{P}\boldsymbol{e}_x$ is introduced, where positive definition matrix $\boldsymbol{P} = \boldsymbol{P}^T \in \mathbb{R}^{6\times 6}$ is the solution of Lyapunov equation $\boldsymbol{A}^T\boldsymbol{P} + \boldsymbol{P}\boldsymbol{A} = -\boldsymbol{I}_6$. Note that $\boldsymbol{P}$ always exists since $\boldsymbol{A}$ is Hurwitz. Following the stability of the perturbed systems [58] and (4.25), the time derivative of $V = \boldsymbol{e}_x^T\boldsymbol{P}\boldsymbol{e}_x$ is

$$\dot{V} \leq -\left(\frac{1}{c_2} - k_1\frac{2c_2}{c_1}\right)V + 2c_2k_0\sqrt{\frac{V}{c_1}}, \tag{4.28}$$

where $c_1 = \lambda_{\min}(\boldsymbol{P}) > 0$ and $c_2 = \lambda_{\max}(\boldsymbol{P}) > 0$ are the minimum and maximum eigenvalues of $\boldsymbol{P}$, respectively. Defining $W = \sqrt{V}$, we write (4.28) as

$$\dot{W} \leq -\alpha W + \frac{2c_2 k_0}{\sqrt{c_1}}, \tag{4.29}$$

where $\alpha = \frac{1}{2}\left(\frac{1}{c_2} - k_1 \frac{2c_2}{c_1}\right) > 0$, namely, $k_1 < \frac{c_1}{2c_2^2}$. Considering $W(t) = \sqrt{V(t)} \geq \sqrt{c_1}\|\boldsymbol{e}_x(t)\|$ and by comparison lemma [58], from (4.29) it is obtained that

$$\|\boldsymbol{e}_x(t)\| \leq c_r e^{-\alpha t}\|\boldsymbol{e}(0)\| + \frac{2c_r^2 k_0}{\alpha} =: e_p^b(t), \tag{4.30}$$

where $c_r = c_2/c_1$. For the error dynamics under controller $\overline{\mathcal{C}}$, the inequality is obtained as

$$\|\overline{\boldsymbol{e}}_x(t)\| \leq c_r e^{-\bar{\alpha} t}\|\overline{\boldsymbol{e}}(0)\| + \frac{2c_r^2 \bar{k}_0}{\bar{\alpha}} =: \bar{e}_p^b(t), \tag{4.31}$$

with $\bar{\alpha} = \frac{1}{2}\left(\frac{1}{c_2} - \bar{k}_1 \frac{2c_2}{c_1}\right) > 0$ and $\bar{k}_1 < \frac{c_1}{2c_2^2}$. From (4.30) and (4.31), it is straightforward to obtain that both errors exponentially converge to the regions near the origin with bounds $\frac{2c_r^2 k_0}{\alpha}$ and $\frac{2c_r^2 \bar{k}_0}{\bar{\alpha}}$, respectively. Considering $\|\boldsymbol{e}_x(0)\| = \|\bar{\boldsymbol{e}}_x(0)\|$ and $\bar{\alpha} \geq \alpha$, $e^{-\bar{\alpha} t} \leq e^{-\alpha t}$ for any t and $\frac{\bar{k}_0}{\bar{\alpha}} \leq \frac{k_0}{\alpha}$, and thus $\bar{e}_p^b(t) \leq e_p^b(t)$ for any $t \geq 0$ because of relationships in (4.26). □

From (4.14), under $\overline{\mathcal{C}}$, the balancing control effect is the same as that of $\mathcal{C}$. The internal system closed-loop error dynamics is still as

$$\ddot{e}_{\varphi_b} + a_1 \dot{e}_{\varphi_b} + a_0 e_{\varphi_b} = d_{\varphi_b}, \tag{4.32}$$

where disturbance $d_{\varphi_b} = \ddot{\varphi}_{be} - \bar{L}_{N_{\text{ext}}}^2 \varphi_{be} + a_1\left(\dot{\varphi}_{be} - \bar{L}_{N_{\text{ext}}} \varphi_{be}\right)$ is also bounded by the norms of the desired trajectory, $\boldsymbol{e}_p$ and $\boldsymbol{e}_{\varphi_b}$ [11]. Because of the unchanged internal error dynamics (4.32) under $\mathcal{C}$ and $\overline{\mathcal{C}}$, the stability and tracking performance for the BEM are the same for these two controllers. Note that this property is obtained by the particular gyro-balancer control u_w given by (4.14). Other alternative control of u_w can be also designed to achieve different properties and to obtain the performance trade-off between position tracking error $\boldsymbol{e}_x$ and balancing error $\boldsymbol{e}_{\varphi_b}$.

4.4 Experiments

Three kinds of experiments are conducted for the path following, trajectory tracking and gyro-balancer assistive control, respectively.

4.4.1 Path following control

These experiments are the autonomous path following without human rider and under the EIC-based control law. Unlike the trajectories tracking, the aim of path following is only reducing the distance between the current position and the desired path. That is, the bikebot rear wheel velocity v_r is controlled and regulated at a constant value. Only the steering control is used for reducing position error. The position error e_p is defined as the directed minimum distance between bikebot current position and the target path. Five paths are introduced for the testing: the straight line, the two types of circluar trajectories with 6-m and 4-m radii, and the two types of '8'-figure trajectories that are formed by circles with 6-m and 4-m radii. For every target path, three different velocities v_r are set, about 1.7 m/s, 2.1 m/s and 2.6 m/s.

In experiments, at the starting time, the bicycle is held by hand and its velocity increases to the desired value before fully released. After releasing and balancing autonomously, the autonomous path following control starts to work. The time varying $\varphi_{be}(t)$ is tracked for both the balancing and path following tasks. This process is repeated for several trials under different experimental conditions. In one trail, the straight line is followed once; the circles are followed twice or three times; and the '8'-figures are followed by once or twice.

Three typical riding performances of straight line, circle and '8'-figure are plotted in Fig. 4.2. In Figs. 4.2(a), 4.2(b) and 4.2(c), the red lines are the target paths. In Fig. 4.2(a), the target straight line is followed by the bikebot over 25 m under $v_r = 2.1$ m/s. The position error is held less than ± 0.15 m. In Fig. 4.2(b), the target circle with radius $r = 6$ m and centered at $(0, 12)$ is tracked by the bikebot in the counter-clockwise direction from the point $(6, 12)$ under $v_r = 2.1$ m/s. A portion of the '8'-figure path following process

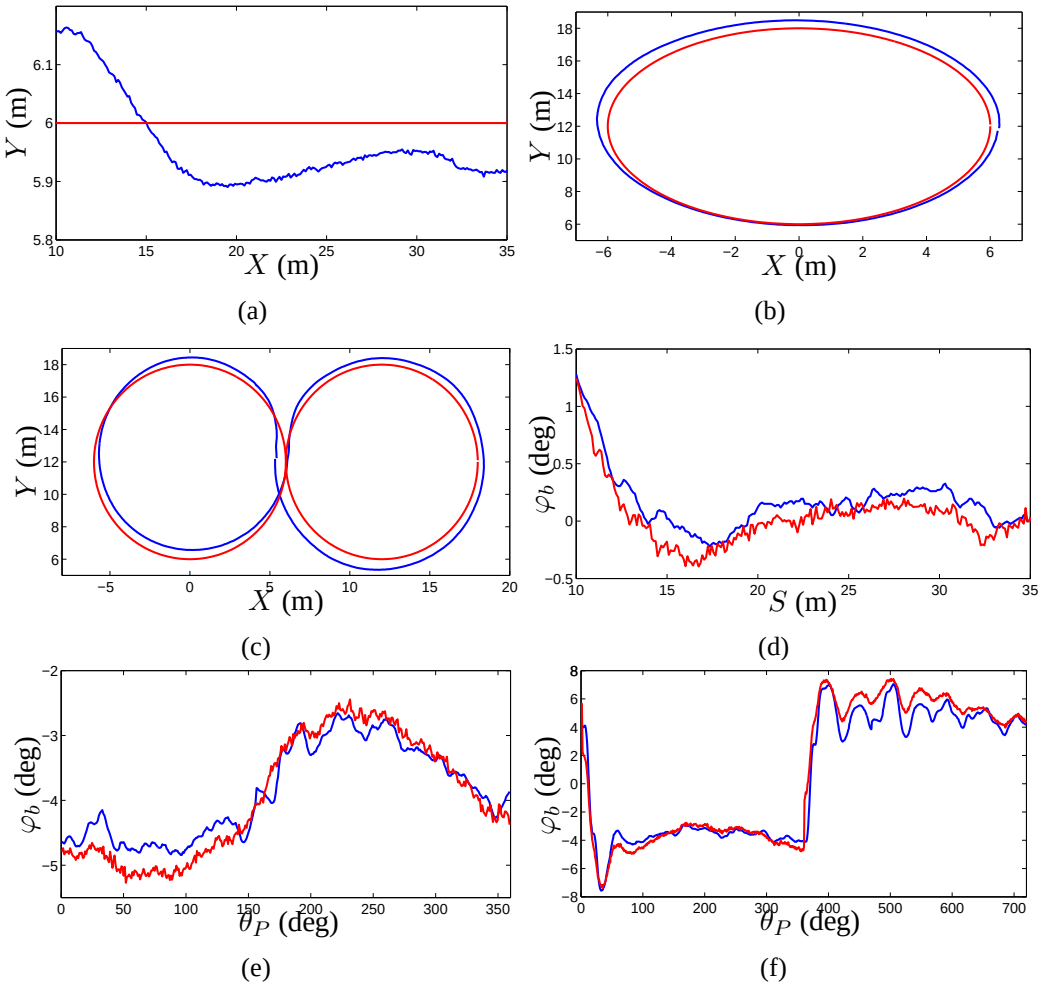

Figure 4.2: Bikebot path following results. (a), (b) and (c) Horizontal position results of Straight line, circle and '8'-figure. (Blue lines are the bikebot horizontal position, Red lines are the target paths.) (d), (e) and (f) Roll angle tracking results of Straight line, circle and '8'-figure. (Blue lines are the measured bikebot roll angle φ_b, Red lines are the target φ_{be} trajectories.)

is also plotted in Fig. 4.2(c). The target path includes two circles with a 6-m radius and centered at $(0, 12)$ and $(12, 12)$, respectively. Under $v_r = 2.1$ m/s, the bikebot starts near the circle-connection point $(6, 12)$, and follows the entire left circle in the counter-clockwise direction and then the entire right circle in the clockwise direction. The blue line is the actual position trajectory. The roll angle φ_{be} tracking results in these three processes are also included in Fig. 4.2. From straight line to '8'-figure, the target path becomes complex, and the position error also increases.

In Figs. 4.2(d), 4.2(e), and 4.2(f), the roll angle trajectories are displayed along the path

arc-length $S(t)$ rather than time. For the straight line, the X-coordinate of the position is used to represent the arc-length. For the circle and '8'-figure, the angular position θ_P is used to represent the arc-length. Angle θ_p is calculated from the vector direction from centers of the circles to the current position. Thus, for the circle path, an entire circle corresponds to $\theta_p \in [0, 360]$ deg, the '8'-figure $\theta_p \in [0, 720]$ deg, with the second circle $\theta_p \in [360, 720]$ deg. From Fig. 4.2, the actual roll angle φ_b (blue line) can track the desired φ_{be} (red line) closely. φ_b of the circle following is shown in Fig. 4.2(e). The most challenging case for roll angle following is for the '8'-figure trajectory, which can be considered as following two circles sequentially from two opposite directions. As shown in Fig. 4.2(f), after passing the connection point $(6, 12)$ (i.e., $\theta_p = 360$ deg), φ_{be} experiences a dramatic change from a negative to positive value.

Fig. 4.2 only demonstrates some examples out of all experiments under different riding conditions. Statistical analysis is required in order to reveal the performance differences among conditions. As previously mentioned, 15 experimental conditions (5 different paths and 3 different velocities) were conducted. Under each condition, 4 completed trails (similar as Fig. 4.2) are gathered. In every single process, the average of absolute position error $|e_p|_{ave}$ and balancing error $|e_\alpha|_{ave}$ are calculated. For every riding condition, the mean values and standard derivations of $|e_p|_{ave}$ and $|e_\alpha|_{ave}$ are calculated and shown in Table 4.1. 'S', 'C6', 'C4', 'E6' and 'E4' represent the straight line, circle with 6m radius, circle with 4m radius, '8'-figure with 6m radius and '8'-figure with 4m radius, respectively. 'L', 'M' and 'H' means the low, middle and high bikebot velocity v_r, respectively.

Table 4.1: The mean and standard deviation of $|e_p|_{ave}$(m) and $|e_\alpha|_{ave}$(deg) for the path following performances.

Path	$\|e_p\|_{ave}$(L)	$\|e_\alpha\|_{ave}$(L)	$\|e_p\|_{ave}$(M)	$\|e_\alpha\|_{ave}$(M)	$\|e_p\|_{ave}$(H)	$\|e_\alpha\|_{ave}$(H)
S	0.13±0.03	0.28±0.02	0.11±0.05	0.22±0.02	0.18±0.04	0.34±0.03
C6	0.28±0.04	0.54±0.03	0.31±0.04	0.38±0.03	0.39±0.05	0.48±0.03
C4	0.35±0.05	0.81±0.02	0.37±0.06	0.82±0.05	0.43±0.10	1.09±0.09
E6	0.33±0.10	0.61±0.06	0.38±0.10	0.73±0.08	0.49±0.11	0.84±0.11
E4	0.41±0.13	0.98±0.06	0.56±0.25	1.45±0.14	0.69±0.30	1.75±0.17

From Table 4.1, under the same velocity, the results of the straight line following always have the smallest position error and tracking errors. The circles' results are better than those of '8'-figures' trajectories. The results of big radius paths are better than those of the small radius paths. When the velocity is increased, both the position errors and the balancing tracking errors are enlarged. From the controller design, the path-following performance is highly related to the roll angle tracking results. If φ_b cannot converge to φ_{be} quickly, the current position also cannot follow the target path in a short time. Due to the model uncertainty, actuation errors and other factors, tracking the near zero $\varphi_{be}(t)$ (Fig. 4.2(d)) is easier than tracking the non-zero target profiles (Fig. 4.2(e)). Compared to the fast and dramatically changing $\varphi_{be}(t)$ profile (Fig. 4.2(f)), the slow varying $\varphi_{be}(t)$ is easier to track.

4.4.2 Trajectory tracking control

We apply the EIC-based controller to track the moving point on the horizontal plane for the bikebot system. The tracking error e_P is the distance between the bikebot and the target moving point, as $e_P = (e_X^2 + e_Y^2)^{0.5}$, where $e_X, e_Y \in \mathbb{R}$ are the errors in the X- and Y-directions, respectively. In the trajectory tracking control design, both the steer angle ϕ and the velocity v_r are considered as control inputs.

To improve the trajectory tracking performance, the regular EIC-based controller is modified by a velocity vector design method [12]. In this experiment, both the regular EIC-based controller and the enhanced EIC-based controller are tested for tracking the same target trajectory. The performances of these two controller are compared. For this comparison, the experimental conditions, the target trajectories and the control parameters of these two controllers are the same. The only difference is that the modified controller has a new modified vector field in the external subsystem controller. A moving point on a cosine wave is designed as the target with the time-parametrization,

$$x_d(t) = 2t, y_d(t) = -3\cos\left(\frac{\pi t}{3}\right) + 9.$$

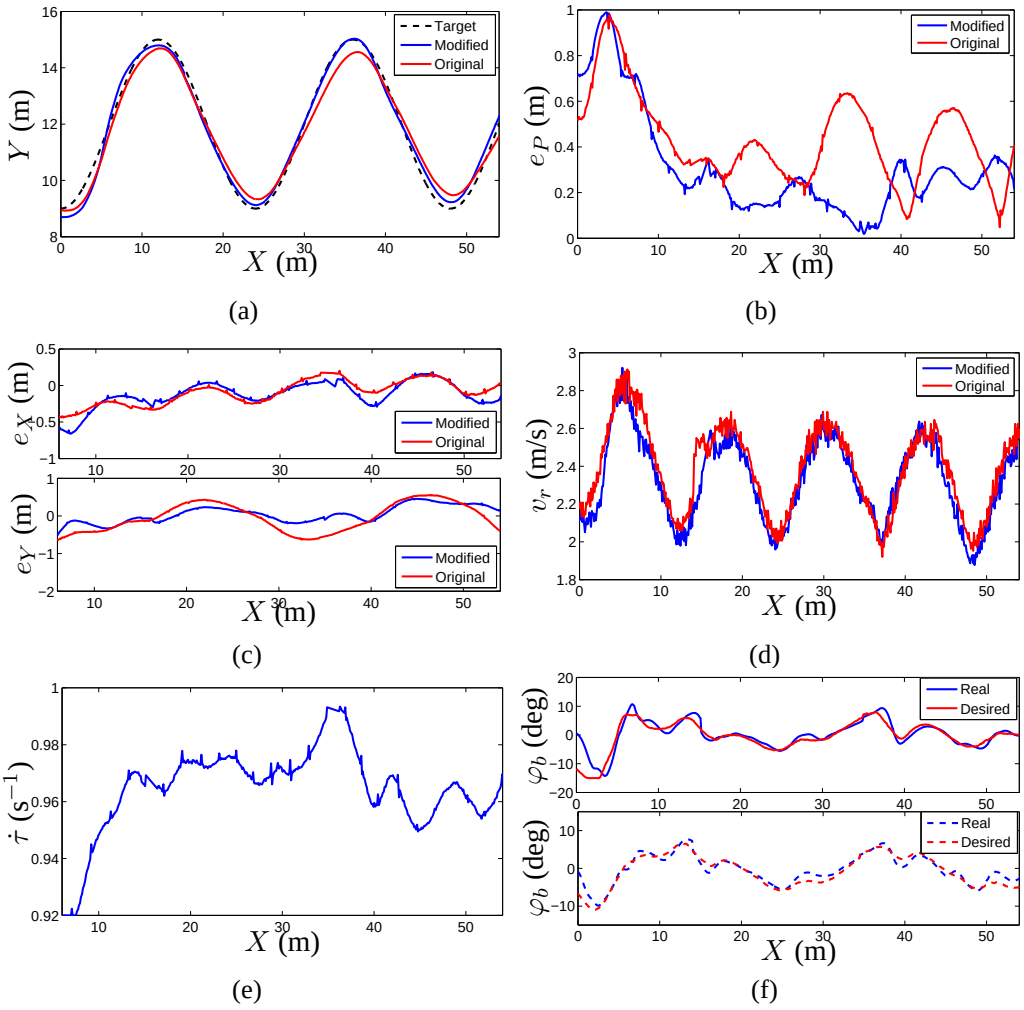

Figure 4.3: Tracking results comparison between the regular EIC controller and modified EIC controller. (a) Position trajectories. (black dash, blue solid and red solid lines are the target trajectory, real trajectory under modified EIC control and real trajectory under regular EIC control.) (b) Position tracking error. (c) Position Tracking errors in X- and Y-directions. (d) Bikebot real velocities under these two controllers. (e) time suspension rate in modified EIC control. (f) Roll angle tracking results. (Upper figure is for the modified EIC control, lower figure is for the original EIC control))

The results are shown in Fig. 4.3. From Fig. 4.3(a), both the enhanced EIC-based controller and the regular one can track the target trajectory. The enhanced controller has better performance than that under the regular EIC-based controller. The position tracking errors are plotted in Fig. 4.3(b). After a few seconds from starting, the position tracking errors of the enhanced controller are smaller than those of the regular control. The error element e_Y is reduced significantly in Fig. 4.3(c). In Fig. 4.3(d), besides the EIC controller, the velocity

vector field also changes the bikebot velocity. At the peak points of the target trajectory, the velocity under enhanced controller is smaller than that of the regular one. In the modified EIC control, the time coordinate of the target trajectory is tuned according to the current position errors, and the new time coordinate τ is introduced. The time suspension rate $\dot{\tau}$ is plotted in Fig. 4.3(e). In Fig. 4.3(f), the roll angle φ_{be} tracking results of these two test are similar under these two controllers.

4.4.3 Gyro-balancer assistive control

In this experiment, the gyro-balancer control is used to enhance performance. A straight line and a circular path are used as the desired paths for the bikebot to follow. Figs. 4.4, 4.5 and 4.6 show the straight line tracking experimental results under both controllers $\mathcal{C}$ and $\overline{\mathcal{C}}$. The trajectory is designed such that the bikebot is controlled to track a straight-line with a constant velocity. Figs. 4.4 and 4.5(a) show the tracking trajectories and tracking errors, respectively. Under both controllers, the bikebot successfully follows the straight-line. However, under $\overline{\mathcal{C}}$, the bikebot reaches to the desired trajectory in a smooth fashion and without overshoot compared to that under $\overline{\mathcal{C}}$. This observation is also clearly reflected by the controlled inputs shown in Figs. 4.6(a) and 4.6(b). Without using the gyro-balancer, after crossing the desired trajectory, the bikebot continues to turn (around 86 s in Fig. 4.6(b)). In contrast, the gyro-balancer helps to generate additional torques to assist balancing task (e.g., around 103 s in Fig. 4.6(a)). This actuation enhancement is also observed from the reduced tracking errors in Fig. 4.5(a). The roll angles shown in Fig. 4.5(b) demonstrate the tracking performance to follow the BEMs and there is no significantly difference between these two controllers. The circle trajectory tracking results are demonstrated in Figs. 4.7, 4.8 and 4.9. The differences between the two controllers are similar to those in the straight line results. By using the gyro-balancer control, the balancing angle tracking performance is enhanced, and the position error is also reduced.

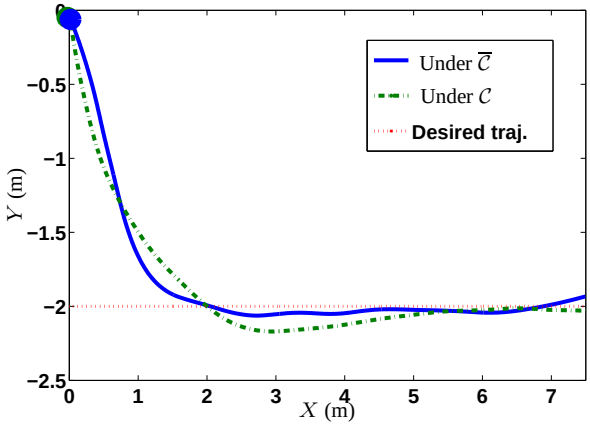

Figure 4.4: Performance comparison of the two controllers $\mathcal{C}$ and $\overline{\mathcal{C}}$ to follow a straight-line. (The solid circular dot indicates the starting location.)

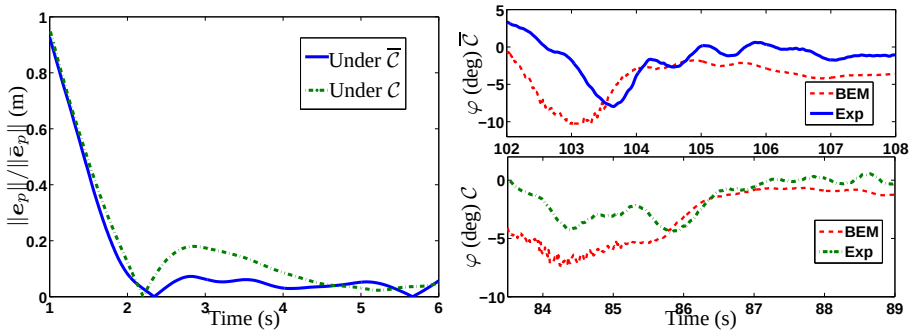

(a) (b)

Figure 4.5: Performance comparison of the two controllers $\mathcal{C}$ and $\overline{\mathcal{C}}$ to follow a straight-line. (a) Tracking errors. (b) Balancing roll angles.

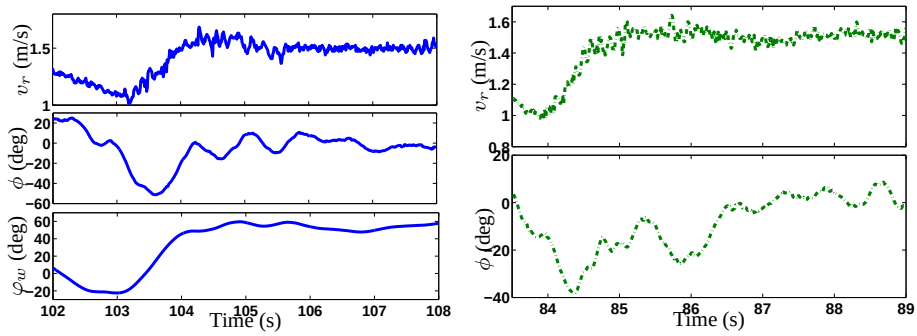

(a) (b)

Figure 4.6: Performance comparison of the two controllers $\mathcal{C}$ and $\overline{\mathcal{C}}$ to follow a straight-line. (a) Controller inputs under $\overline{\mathcal{C}}$. (b) Controller inputs under $\mathcal{C}$.

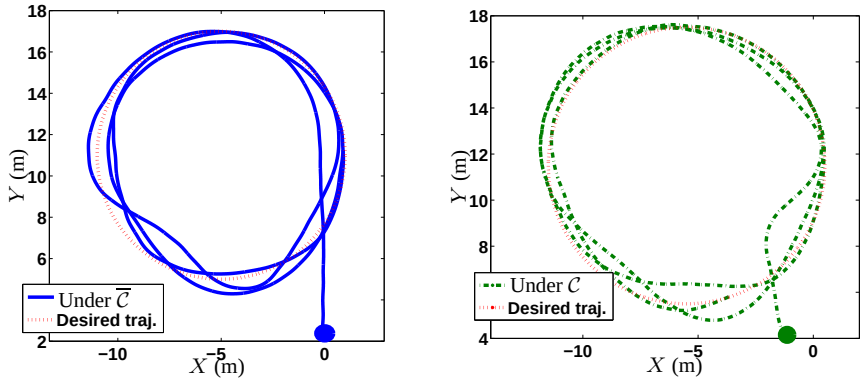

(a) (b)

Figure 4.7: Performance comparison of the two controllers $\mathcal{C}$ and $\overline{\mathcal{C}}$ to follow a circular trajectory. (a) The tracking trajectory under $\overline{\mathcal{C}}$. (b) The tracking trajectory under $\mathcal{C}$. The solid circular dots indicate the starting locations in (a) and (b).

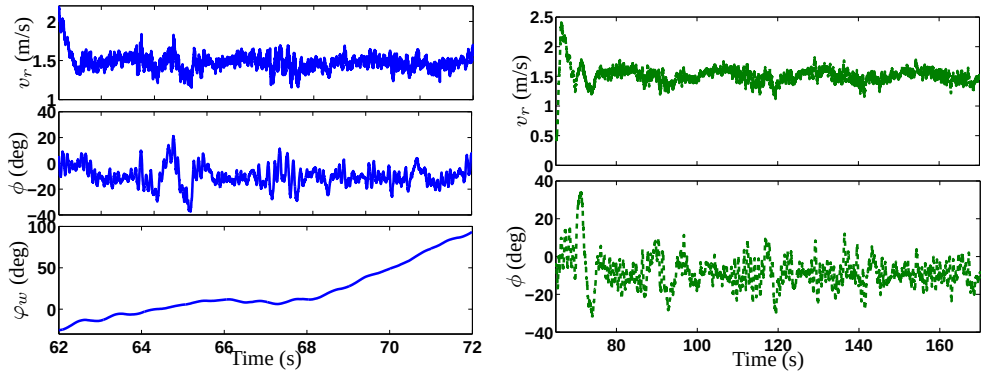

(a) (b)

Figure 4.8: Performance comparison of the two controllers $\mathcal{C}$ and $\overline{\mathcal{C}}$ to follow a circular trajectory. (a) Tracking errors under $\overline{\mathcal{C}}$. (b) Controller inputs under $\mathcal{C}$.

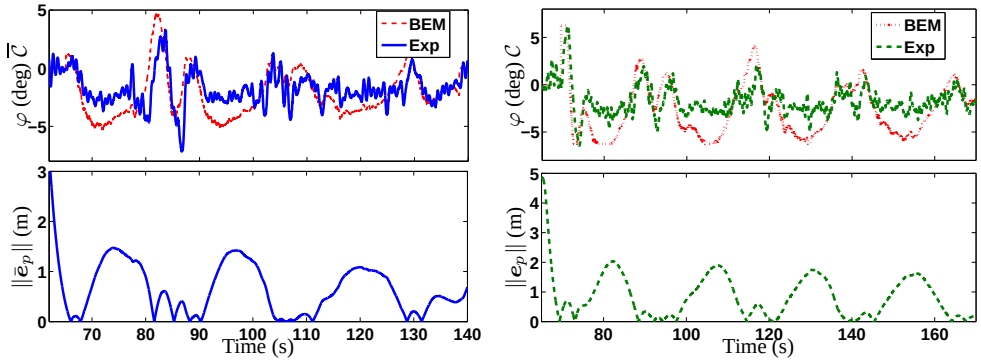

(a) (b)

Figure 4.9: Performance comparison of the two controllers $\mathcal{C}$ and $\overline{\mathcal{C}}$ to follow a circular trajectory. (a) Balancing roll angles and position errors under $\overline{\mathcal{C}}$. (b) Balancing roll angles and position errors under $\mathcal{C}$.

4.5 Conclusion

A trajectory tracking and balancing control design for autonomous bikebot was presented in this chapter. The control systems were built on the attractive EIC property of the bikebot dynamics. Two controller designs were proposed: one only used velocity and steering actuation as the control inputs and the other used the gyro-balancer as an additional actuation besides the aforementioned two inputs. Under both controllers, the position tracking error and the roll angle tracking error were guaranteed to converge exponentially to regions near the origin. Moreover, the use of the gyro-balancer was shown to guarantee a smaller position tracking error bound than that by only using steering and velocity inputs. Extensive outdoor bikebot experiments were conducted to validate and demonstrate the control design performance.

Chapter 5
Control Analysis for Human Tracking Riding

5.1 Introduction

Human with trained motor skills can fluidly and flexibly interact with machines and these machines can also provide augmented and enhanced actuation to facilitate human's motor skills. Postural balance is a critical human motor skill in many human daily activities, such as standing, walking, riding a bicycle, and other human-machine or human-robot interactions. Understanding and capturing the characteristics of human balance control in these human activities are important to design human assistive devices and rehabilitation robots. In this chapter, the rider-bikebot (i.e., bicycle-based robot) interactions are utilized as an example to study human balance skills and characteristics in interactions with machines.

As mentioned in Chapter 2, bikebot is an actively controlled bicycle-based robot that was developed for studying human balance motor skills [20]. Bikebot riding is used as the example to study human balance motor skills primarily for several considerations. First, balancing the unstable platform (e.g., bicycle) requires the coordinated control of multi-limb and body movements and thus, this riding activity excites the human whole-body movements and dynamics. Multiple actuations such as human upper-body movement, steering or speed control are used individually or combinationally for balance task. Therefore, it provides attractive venues to study how human rider use and choose multiple actuation options for the balance and path-following tasks. Second, as a single-track vehicle, a rider must also steer the platform to follow a desired path while maintaining a balance without falling. This multi-task feature in bicycle riding represents two complementary and sometimes competing aspects of human motor characteristics in human-machine or

human-robot interactions. Understanding how human deals with the trade-off or compromise between the path-following and the platform balance tasks is another motivation to study rider-bikebot interactions. Finally, as a direct application, bicycle riding is also reported as a diagnosis and rehabilitation tool for postural disabilities [40, 63].

The existing work on bicycle dynamics and models can be traced back more than one hundred years ago [16, 64]. However, understanding the rider's sensorimotor mechanism and its interaction with the unstable platform is only reported in recent years [12, 29, 30]. The work in [29] uses a multi-body dynamics approach and an input/output viewpoint to understand how the physical parameters affect the rider-bicycle interactions. In [30], extensive human experiments are conducted to present the relationship between the bicycle riding and the postural balance motor skill enhancements. The work in [12] focus on the sensing, modeling and control of the rider-bicycle-environment interactions. Inspired by the human stance control [65], the work in [21] proposes a feedback control model for the rider's upper-body movement and the steering mechanism in balancing the bicycle platform. The human control models in [21, 65] capture the human sensorimotor characteristics such as latencies. The stability conditions are presented for the rider-bicycle system using the time-delayed analysis [21].

Capturing and quantifying the human motor skills is an challenging task due to the complexity and high dimensions of human motion and locomotion. Machine learning technique is one approach to capture the human motor skills on the lower-dimensional skill manifolds. For example, in [32], motion planning is conducted on the learned skill manifolds without need to build the analytical robotic models. Embedded skill manifolds are also presented in [33, 34] to represent human hand motion. However, all of the aforementioned work mainly discuss the human motor skills without consideration their interactions with machines or robots. In many applications, the interactions between the human and the machines or robots provide assistance and enhancements to facilitate motor skills learning [66] and therefore, it is critical to capture and characterize these interactions.

Many bicycle dynamics and control work mainly consider the balance task rather than

focus on the competing trajectory-following task at the same time. The work presented in this chapter fills such a knowledge gap through the BEM concept. It is shown that the rider-bikebot dynamics that can be written as a nearly EIC form [11] and is similar as the autonomous bikebot dynamics discussed in Chapter 4. The external subsystem of the rider-bicycle dynamics deals with the trajectory tracking and the internal subsystem captures the rolling motion of the rider upper-body and the bikebot platform. The attractive property of the EIC structure enables to treat the trajectory-tracking and balance performance in two interconnected subsystems such that we can qualify each aspect of the performance under one modeling and control framework. The BEM is then used to analyze and compare the contributions of the human upper-body movement and steering actuations for balance task. Finally, taking advantage of the EIC structure, a state-feedback controller is proposed for rider tracking and balancing. The control performance is also compared with human control. The new metrics are introduced to define the human riding and balance motor skills. The extensive experiments are conducted to illustrate and demonstrate the BEM and balancing skill metrics. Furthermore, the control results of human rider are also compared with those of autonomous control in Chapter 4. The contribution of the work lies in the new BEM concept and the BEM-based metrics for human motor skills with applications to the rider-bikebot interactions. This work also complement the learned skill manifold approach by providing an analytical method to quantify the human balance motor skills in physical human-robot interactions.

The rest of the chapter is organized as follows. In Section 5.2, the BEM analysis is presented. The analysis of the steering and body movement actuation for the balance task is presented in Section 5.3. The control stability analysis and balance skill metrics are discussed in Section 5.4. Experimental results are presented in Section 5.5. Finally, the concluding remarks are summarized in Section 5.6.

5.2 Dynamics structure and BEM

Based on the same EIC structure mentioned in Fig. 4.1 of Chapter 4, and the rider-bicycle dynamics (2.13) and (2.12), it is straightforward to see from (5.1) that the rider-bikebot system is indeed in nearly EIC form, as

$$\Sigma_{\text{ext}} \;:\; \boldsymbol{r}_{C_2}^{(3)} = \boldsymbol{u}_N, \tag{5.1a}$$

$$\Sigma_{\text{int}} \;:\; \ddot{\boldsymbol{q}} = \boldsymbol{M}^{-1}(\boldsymbol{q})\left[\boldsymbol{B}(\boldsymbol{q})\boldsymbol{R}_{\psi}^{-1}(\boldsymbol{\Psi}+\boldsymbol{u}_N) - \boldsymbol{C}(\boldsymbol{q},\dot{\boldsymbol{q}}) - \boldsymbol{G}(\boldsymbol{q}) + \boldsymbol{u}_i\right] \tag{5.1b}$$

with $\boldsymbol{u}_i = \boldsymbol{\tau}$.

In the rider tracking task, the desired trajectory $\mathcal{T}$: $(X_d(t), Y_d(t))$ in $\mathcal{N}$ is tracked by the rider-bikebot system. According to the nearly EIC structure (5.1), the external dynamics Σ_{ext} determine the tracking of $\mathcal{T}$. The rider's control inputs for external system Σ_{ext} is denoted as $\boldsymbol{u}^h = [u_r^h, u_\psi^h]^T$ (i.e., velocity and yaw angle controls) and $\boldsymbol{u}_i = \boldsymbol{\tau}$ (i.e., trunk torque control) with bikebot trajectory $(X(t), Y(t))$ and rider-bicycle roll angles $\boldsymbol{q}(t)$. Under $\boldsymbol{u}^h$ and $\boldsymbol{u}_i^h$, dynamics (5.1) become

$$\Sigma_{\text{ext}} :\; \boldsymbol{r}_{C_2}^{(3)} = \boldsymbol{u}_N^h := -\boldsymbol{\Psi} + \boldsymbol{R}_\psi \boldsymbol{u}^h, \tag{5.2a}$$

$$\Sigma_{\text{int}} :\; \ddot{\boldsymbol{q}} = \boldsymbol{M}^{-1}(\boldsymbol{q})\left(\boldsymbol{B}(\boldsymbol{q})\boldsymbol{u}^h + \boldsymbol{\tau} - \boldsymbol{C}(\boldsymbol{q},\dot{\boldsymbol{q}}) - \boldsymbol{G}(\boldsymbol{q})\right). \tag{5.2b}$$

The internal (roll angles) equilibria are denoted as $\boldsymbol{q}_e$, by setting $\dot{\boldsymbol{q}} = \ddot{\boldsymbol{q}} = 0$ in (5.2b). The implicit function $\boldsymbol{F}(\boldsymbol{q}, \dot{\psi}, v_r, \boldsymbol{u}, \boldsymbol{\tau})$ of $\boldsymbol{q}$ is defined as

$$\boldsymbol{F}(\boldsymbol{q}, \dot{\psi}, v_r, \boldsymbol{u}, \boldsymbol{\tau}) := \boldsymbol{B}(\boldsymbol{q})\boldsymbol{u} + \boldsymbol{\tau} - \boldsymbol{C}_q(\boldsymbol{q}) - \boldsymbol{G}(\boldsymbol{q}) \tag{5.3}$$

with $\boldsymbol{C}_q(\boldsymbol{q}) := \boldsymbol{C}_q(\boldsymbol{q}, \boldsymbol{0})$. The roll angle equilibria $\boldsymbol{q}_e = \boldsymbol{q}_e(\dot{\psi}, v_r, \boldsymbol{u}, \boldsymbol{\tau})$ are the solutions of the algebraic equation

$$\boldsymbol{F}(\boldsymbol{q}_e, \dot{\psi}, v_r, \boldsymbol{u}, \boldsymbol{\tau}) = \boldsymbol{0}. \tag{5.4}$$

The BEM under rider control $\mathcal{E}(\boldsymbol{u}^h, \boldsymbol{\tau})$ is then defined as an 8-dimensional (X, Y)-subspace in $\mathbb{R}^8$ of Σ_{ext} under $\boldsymbol{u}^h$ and $\boldsymbol{\tau}$.

$$\mathcal{E}(\boldsymbol{u}^h, \boldsymbol{\tau}) = \left\{(\boldsymbol{x}, \boldsymbol{\alpha}) \;\middle|\; \boldsymbol{q}_e = \boldsymbol{q}_e(\dot{\psi}, v_r, \boldsymbol{u}^h, \boldsymbol{\tau}), \dot{\boldsymbol{q}} = \boldsymbol{0}\right\} \tag{5.5}$$

with $\boldsymbol{x} = [\boldsymbol{r}_{C_2}^T, \dot{\boldsymbol{r}}_{C_2}^T, \ddot{\boldsymbol{r}}_{C_2}^T]^T$ and $\boldsymbol{\alpha} = [\boldsymbol{q}^T, \dot{\boldsymbol{q}}^T]^T$. The design follows the similar approach in [67] and first step is to design a controller for Σ_{ext} disregarding, for the moment, the evolution of Σ_{int} (5.1b) as

$$\boldsymbol{u}_N^{\text{ext}} = \boldsymbol{r}_d^{(3)} - b_2\ddot{\boldsymbol{e}}_p - b_1\dot{\boldsymbol{e}}_p - b_0\boldsymbol{e}_p, \tag{5.6}$$

where $\boldsymbol{r}_d = [X_d(t), Y_d(t)]^T$, error $\boldsymbol{e}_p(t) = [e_X, e_Y]^T = \boldsymbol{r}_{C_2} - \boldsymbol{r}_d$, and $\boldsymbol{r}_d^{(m)}$ denotes the m-th derivative of $\boldsymbol{r}_d$. The constants b_i, $i = 0, 1, 2$, are chosen such that the polynomial equation $s^3 + b_2 s^2 + b_1 s + b_0 = 0$ is Hurwitz. Under such a control, a nominal external vector field $\mathbf{N}_{\text{ext}}$ is defined as

$$\mathbf{N}_{\text{ext}} := \begin{bmatrix} \dot{X}(t) \\ \ddot{X}(t) \\ X_d^{(3)} - \sum_{i=0}^{2} b_i e_X^{(i)} \\ \dot{Y}(t) \\ \ddot{Y}(t) \\ Y_d^{(3)} - \sum_{i=0}^{2} b_i e_Y^{(i)} \end{bmatrix}. \tag{5.7}$$

By (5.6), the input $\boldsymbol{u}^{\text{ext}}$ is defined as

$$\boldsymbol{u}^{\text{ext}} \;=\; \boldsymbol{R}_{\psi}^{-1}\left(\boldsymbol{\Psi} + \boldsymbol{u}_N^{\text{ext}}\right). \tag{5.8}$$

Similar to (5.5), the BEM $\mathcal{E}(\boldsymbol{u}^{\text{ext}}, \boldsymbol{\tau})$ is defined as

$$\mathcal{E}(\boldsymbol{u}^{\text{ext}}, \boldsymbol{\tau}) = \left\{ (\boldsymbol{x}, \boldsymbol{\alpha}) \;\middle|\; \boldsymbol{q}_e = \boldsymbol{q}_e(\dot{\psi}, v_r, \boldsymbol{u}^{\text{ext}}, \boldsymbol{\tau}), \dot{\boldsymbol{q}} = \boldsymbol{0} \right\}. \tag{5.9}$$

The BEM $\mathcal{E}(\boldsymbol{u}^{\text{ext}}, \boldsymbol{\tau})$ can be viewed as a time-dependent graph in $\mathbb{R}^6$ of Σ_{ext} that is evolved with the external nominal vector field $\mathbf{N}_{\text{ext}}$ under control $\boldsymbol{u}^{\text{ext}}$ and $\boldsymbol{\tau}$. The roll angles $\boldsymbol{q}$ need to be controlled around $\mathcal{E}(\boldsymbol{u}^{\text{ext}}, \boldsymbol{\tau})$ while tracking $\mathcal{T}$ under $\boldsymbol{u}^{\text{ext}}$. Note that $\dot{\boldsymbol{q}}_e \neq 0$ and $\ddot{\boldsymbol{q}}_e \neq 0$ in general and the derivatives $\dot{\boldsymbol{q}}_e$ and $\ddot{\boldsymbol{q}}_e$ are approximated by using directional derivatives [68] along $\mathbf{N}_{\text{ext}}$ due to their dependency on the external subsystems and $\mathbf{u}_{\text{ext}}$, namely,

$$\bar{L}_{\mathbf{N}_{\text{ext}}}\boldsymbol{q}_e = L_{\mathbf{N}_{\text{ext}}}\boldsymbol{q}_e + \frac{\partial \boldsymbol{q}_e}{\partial t},\; \bar{L}^2_{\mathbf{N}_{\text{ext}}}\boldsymbol{q}_e = \bar{L}_{\mathbf{N}_{\text{ext}}}\bar{L}_{\mathbf{N}_{\text{ext}}}\boldsymbol{q}_e.$$

Combining the inputs $\boldsymbol{u}_i$ and u_ψ in (2.13), (5.1b) is rewritten as

$$\ddot{\boldsymbol{q}} = \boldsymbol{M}^{-1}(\boldsymbol{q})[\boldsymbol{B}_\tau(\boldsymbol{q})\boldsymbol{u}^{\text{int}} - \boldsymbol{C}(\boldsymbol{q}, \dot{\boldsymbol{q}}) - \boldsymbol{G}(\boldsymbol{q})], \tag{5.10}$$

where

$$\boldsymbol{u}^{\text{int}} = \begin{bmatrix} u_\psi^{\text{int}} \\ u_\tau^{\text{int}} \end{bmatrix} = \begin{bmatrix} u_\psi \\ \tau \end{bmatrix}, \ \boldsymbol{B}_\tau = \begin{bmatrix} B_{12} & 0 \\ B_{22} & 1 \end{bmatrix}$$

and B_{ij} is element of $\boldsymbol{B}$ at the ith row and jth column. The stabilizing control of Σ_{int} in (5.10) around $\mathcal{E}(\boldsymbol{u}^{\text{ext}}, \boldsymbol{\tau})$ is then given by

$$\boldsymbol{u}^{\text{int}} = \boldsymbol{B}_\tau^{-1}\left(\boldsymbol{C} + \boldsymbol{G} + \boldsymbol{M}\boldsymbol{v}^{\text{int}}\right), \boldsymbol{v}^{\text{int}} = \bar{L}^2_{\mathbf{N}_{\text{ext}}}\boldsymbol{q}_e - a_1\dot{\boldsymbol{e}}_q - a_0\boldsymbol{e}_q, \tag{5.11}$$

where $\boldsymbol{e}_q = \boldsymbol{q} - \boldsymbol{q}_e$, $\dot{\boldsymbol{e}}_q = \dot{\boldsymbol{q}} - \dot{\boldsymbol{q}}_e \approx \dot{\boldsymbol{q}} - \bar{L}_{\mathbf{N}_{\text{ext}}}\boldsymbol{q}_e$, constants a_0 and a_1 are chosen such that $s^2 + a_1 s + a_0 = 0$ is Hurwitz.

The final control system design of the rider-bikebot system (5.1) combines the above development in (5.8) and (5.11) as

$$u_r = u_r^{\text{ext}}, \ u_\psi = u_\psi^{\text{int}}, \ \tau = u_\tau^{\text{int}}. \tag{5.12}$$

Notice that the internal subsystem design has no influence on the input channel u_r because only u_ψ gets involved into the internal subsystem (5.1b). The coupling between the external and internal subsystem control design is through the introduction of the BEM $\mathcal{E}(\boldsymbol{u}^{\text{ext}}, \boldsymbol{\tau})$. By BEM, the external and internal subsystems can be decoupled approximately due to the nearly EIC dual structural properties.

5.3 Balancing by body movement and steering

In this section, the effects of two control actuations, the rider upper-body movement and the bikebot steering actuation on balancing the platform, are discussed. The analysis is primarily built on the BEM development in the previous section.

To quantify the influence of the upper-body movement and the steering actuation on balance task, the rider-bikebot systems is perturbed around the BEM, and then the sensitivity near the perturbed BEM is computed. Noting that the first element of function

$\boldsymbol{F}(\boldsymbol{q}, \dot{\psi}, v_r, \boldsymbol{u}, \boldsymbol{\tau})$ in (5.3), denoted as F_1 [1], is not a function of τ. The total derivative of F_1 is

$$dF_1 = \frac{\partial F_1}{\partial \varphi_b} d\varphi_b + \frac{\partial F_1}{\partial \varphi_h} d\varphi_h + \frac{\partial F_1}{\partial \dot{\psi}} d\dot{\psi} + \frac{\partial F_1}{\partial u_\psi} du_\psi. \tag{5.13}$$

Around BEM, changes of rider upper-body roll angle ($d\varphi_h$) and the bikebot roll angle ($d\varphi_b$) are not independent. The relationship between $d\varphi_h$ and $d\varphi_b$ around $\mathcal{E}(\boldsymbol{u}, \boldsymbol{\tau})$ is first calculated. From the BEM relationship given in (5.3) and the internal dynamics (2.13), it is noted that function $\boldsymbol{F}(\boldsymbol{q}, \dot{\psi}, v_r, \boldsymbol{u}, \boldsymbol{\tau})$ indeed is the right hand side of internal dynamics (2.13) evaluated at $\dot{\boldsymbol{q}} = 0$, that is,

$$\boldsymbol{M}(\boldsymbol{q})\ddot{\boldsymbol{q}}\big|_{\dot{\boldsymbol{q}}=\boldsymbol{0}} = \boldsymbol{F}(\boldsymbol{q}, \dot{\psi}, v_r, \boldsymbol{u}, \boldsymbol{\tau}).$$

The first equation from above is

$$\left(M_{11} \frac{d\dot{\varphi}_b}{dt} + M_{12} \frac{d\dot{\varphi}_b}{dt} \right) \Big|_{\dot{\boldsymbol{q}}=\boldsymbol{0}} = F_1, \tag{5.14}$$

where M_{ij} is the element of $\boldsymbol{M}(\boldsymbol{q})$ at the ith row and jth column. Noting that around BEM, $F_1 = 0$ ($\dot{\boldsymbol{q}} = \boldsymbol{0}$), from (5.14), it is obtained that

$$\left(M_{11} d\dot{\varphi}_b + M_{12} d\dot{\varphi}_b \right) \Big|_{\dot{\boldsymbol{q}}=\boldsymbol{0}} = F_1 dt = 0,$$

and thus by integration,

$$\frac{d\varphi_b}{d\varphi_h} = -\frac{M_{12}}{M_{11}}. \tag{5.15}$$

Using (5.15), the first two terms in (5.13) reduce to

$$\underbrace{\left(-\frac{\partial F_1}{\partial \varphi_b} \frac{M_{12}}{M_{11}} + \frac{\partial F_1}{\partial \varphi_h} \right)}_{\lambda_{\varphi_h}} d\varphi_h = \lambda_{\varphi_h} d\varphi_h, \tag{5.16}$$

where λ_{φ_h} is the sensitivity factor of the upper-body roll angle φ_h. It is straightforward to calculate and obtain

$$\begin{aligned} \lambda_{\varphi_h} = & \left(-\tfrac{M_{12}}{M_{11}} A_1 + m_h h_h \, \mathrm{s}_{\varphi_b + \varphi_h} \right) v_r \dot{\psi} + \left(-\tfrac{M_{12}}{M_{11}} A_2 - m_h h_h \, \mathrm{c}_{\varphi_b + \varphi_h} \right) g \\ & + \left[\tfrac{M_{12}}{M_{11}} \left(m_b h_b l_b \, \mathrm{s}_{\varphi_b} + m_h h_s l_s \left(\mathrm{s}_{\varphi_b} + \mathrm{s}_{\varphi_b + \varphi_h} \right) \right) - m_h h_h l_s \, \mathrm{s}_{\varphi_b + \varphi_h} \right] \ddot{\psi} \\ & + \left[-\tfrac{M_{12}}{M_{11}} A_3 - m_h h_s (h_h \, \mathrm{c}_{2\varphi_b + \varphi_h} + h_s \, \mathrm{c}_{2\varphi_b + 2\varphi_h}) \right] \dot{\psi}^2, \end{aligned} \tag{5.17}$$

[1] The arguments of function $\boldsymbol{F}(\boldsymbol{q}, \dot{\psi}, v_r, \boldsymbol{u}, \boldsymbol{\tau})$ are dropped for notation concise. Also, input u_r (as part of $\boldsymbol{u}$ does not appear in $\boldsymbol{F}(\boldsymbol{q}, \dot{\psi}, v_r, \boldsymbol{u}, \boldsymbol{\tau})$.

with $A_1 = M_h\,\mathrm{s}_{\varphi_b} + m_h h_h\,\mathrm{s}_{\varphi_b+\varphi_h}$, $A_2 = M_h\,\mathrm{c}_{\varphi_b} + m_h h_h\,\mathrm{c}_{\varphi_b+\varphi_h}$, and $A_3 = J_m\,\mathrm{c}_{2\varphi_b} + m_h h_s^2\,\mathrm{c}_{2(\varphi_b+\varphi_h)} + 2m_h h_h h_s\,\mathrm{c}_{2\varphi_b+\varphi_h}$. For the steering actuation (i.e., steering angle ϕ), the sensitivity factor can be calculated similarly as

$$\lambda_\phi = \frac{\partial F_1}{\partial \phi} = -\frac{v_r^2\,\mathrm{c}_\xi}{l\,\mathrm{c}_{\varphi_b}\,\mathrm{c}_\phi^2}\left(A_2 + A_4\frac{\mathrm{c}_\xi\,\mathrm{s}_\phi}{2l\,\mathrm{c}_{\varphi_b}\,\mathrm{c}_\phi}\right), \tag{5.18}$$

with $A_4 = J_m\,\mathrm{s}_{2\varphi_b} + m_h h_s^2\,\mathrm{s}_{2\varphi_b+2\varphi_h} + 2m_h h_h h_s\,\mathrm{s}_{2\varphi_b+\varphi_h}$.

Although the closed-forms for sensitivity factors λ_{φ_h} and λ_ϕ are obtained, it is not obvious to obtain the conclusive comparison of their magnitude relationship directly from (5.17) and (5.18). Instead, using the typical parameter values of the rider-bicycle system, λ_{φ_h} and λ_ϕ are plotted under variations of kinematic parameters such as yaw rate and bikebot velocity as shown in Fig. 5.1. From Fig. 5.1(a), it is clearly observed that near the zero, magnitude of λ_{φ_h} becomes larger than that with other rider upper-body roll angles. Moreover, at higher bikebot yaw rate, the magnitude of λ_{φ_h} is larger as well. These results imply that it is more effective to turn upper-body at the up-straight position and with fast turning of bikebot. For steering actuation effect, it is clearly shown in (5.18) that the value of λ_ϕ highly depends on the bikebot velocity v_r (e.g., proportional to v_r^2). The influence of the yaw rate on λ_ϕ is minimal. It is also clearly shown that it is much more effective to use steering actuation at small steering angles (i.e., high sensitivity).

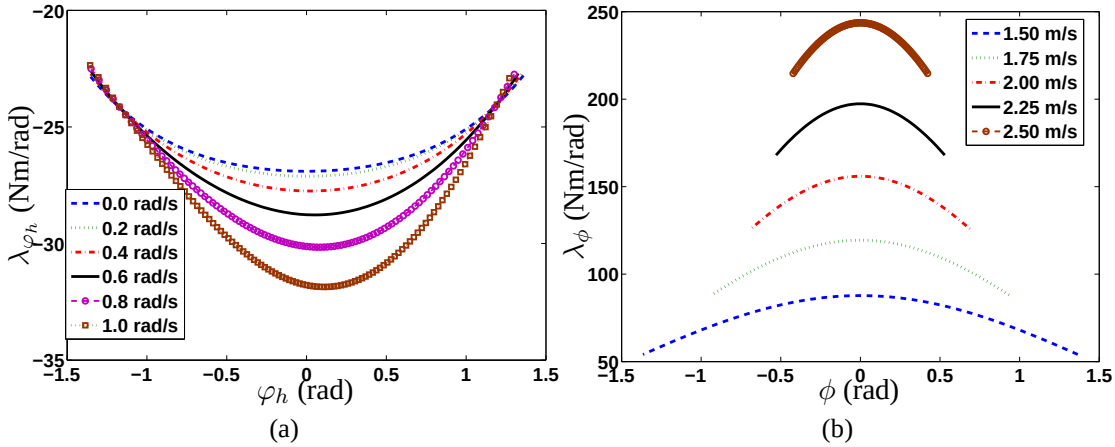

Figure 5.1: (a) Sensitivity factor λ_{φ_h} with varying yaw rate $\dot{\psi}$. (b) Sensitivity factor λ_ϕ with varying bikebot velocity v_r.

Comparing the results in Figs. 5.1(a) and 5.1(b), it is interesting to note that for the same

amount of change of steering angle ϕ and upper-body roll angle φ_h, the value of λ_ϕ is about five times of that of λ_{φ_h}. This comparison result implies that the torque generated by one unit of steering angle is more than five times than that by one unit of the upper-body leaning angle. This observation partially explains the perturbation experiments reported in [20] that the rider primarily uses the steering actuation than the body movement to compensate for the disturbance for keeping balance of the bikebot platform.

5.4 Riding balance performance metrics

5.4.1 Stability analysis for EIC design

From (5.10), the closed-loop dynamics for Σ_{int} is obtained as

$$\boldsymbol{M}\left(\boldsymbol{q}\right)\ddot{\boldsymbol{q}}+\boldsymbol{C}_q\left(\boldsymbol{q},\dot{\boldsymbol{q}}\right)+\boldsymbol{G}\left(\boldsymbol{q}\right)=\boldsymbol{B}_\tau\left(\boldsymbol{q}\right)\boldsymbol{u}^{\text{int}}. \tag{5.19}$$

Meanwhile, from the BEM (5.9) and (5.4), the equilibrium point $\boldsymbol{q}_e$ relationship is obtained as

$$\boldsymbol{B}_\tau(\boldsymbol{q}_e)\begin{bmatrix}u_\psi^{\text{ext}}\\ \tau_e\end{bmatrix}-\boldsymbol{C}_q(\boldsymbol{q}_e)-\boldsymbol{G}(\boldsymbol{q}_e)=\boldsymbol{0}. \tag{5.20}$$

Combining the first equation in (5.19) and (5.20), the relationship between u_ψ^{ext} and u_ψ^{int} is

$$u_\psi^{\text{int}}=u_\psi^{\text{ext}}+p_p', \tag{5.21}$$

with the difference term

$$\begin{aligned}p_p' \;=\; & p_p(\boldsymbol{q},\dot{\boldsymbol{q}},\ddot{\boldsymbol{q}},\boldsymbol{q}_e)=\left(\boldsymbol{B}_\tau^{-1}(\boldsymbol{q}_e)\left[\boldsymbol{C}_q(\boldsymbol{q}_e)-\boldsymbol{G}(\boldsymbol{q}_e)\right]\right)_1\\ & -\left(\boldsymbol{B}_\tau^{-1}(\boldsymbol{q})\left[\boldsymbol{M}(\boldsymbol{q})\ddot{\boldsymbol{q}}+C_q(\boldsymbol{q},\dot{\boldsymbol{q}})+\boldsymbol{G}(\boldsymbol{q})\right]\right)_1.\end{aligned}$$

In the above equation, notation $(\boldsymbol{x})_i$ denotes the ith element of vector $\boldsymbol{x}$. Substituting u_ψ^{int} and u_r into the external control (5.6), (5.8) and external dynamics (5.1a), the error dynamics for Σ_{ext} is given by

$$\boldsymbol{e}_p^{(3)}+b_2\ddot{\boldsymbol{e}}_p+b_1\dot{\boldsymbol{e}}_p+b_0\boldsymbol{e}_p=\boldsymbol{R}_\psi\begin{bmatrix}p_p'\\ 0\end{bmatrix}=:\boldsymbol{p}_p. \tag{5.22}$$

Similarly, from (5.11), the closed-loop error dynamics for Σ_{int} is obtained as

$$\ddot{\boldsymbol{e}}_q + a_1\dot{\boldsymbol{e}}_q + a_2\boldsymbol{e}_q = \boldsymbol{p}_q, \tag{5.23}$$

where $\boldsymbol{p}_q = \ddot{\boldsymbol{q}}_e - \bar{L}^2_{\boldsymbol{N}_{\text{ext}}}\boldsymbol{q}_e + a_1(\dot{\boldsymbol{q}}_e - \bar{L}_{\boldsymbol{N}_{\text{ext}}}\boldsymbol{q}_e)$. Similar to that in [11], it is assumed that vector $\boldsymbol{p}_p$ and $\boldsymbol{p}_q$ are affine with errors, namely, there exist positive constants $c_i > 0$, $i = 1, \cdots, 6$, such that

$$\|\boldsymbol{p}_p\|_2 \le c_1 + c_2\|\boldsymbol{e}_1\|_2 + c_3\|\boldsymbol{e}_2\|_2, \|\boldsymbol{p}_q\|_2 \le c_4 + c_5\|\boldsymbol{e}_1\|_2 + c_6\|\boldsymbol{e}_2\|_2.$$

The error vectors $\boldsymbol{e}_1$ and $\boldsymbol{e}_2$ are defined as $\boldsymbol{e}_1 = [e_X, \dot{e}_X, \ddot{e}_X, e_Y, \dot{e}_Y, \ddot{e}_Y]^T$ and $\boldsymbol{e}_2 = [e_b, \dot{e}_b, e_h, \dot{e}_h]^T$. For error dynamics (5.22) and (5.23), the matrices $\boldsymbol{A}_p$ and $\boldsymbol{A}_q$ are

$$\boldsymbol{A}_p = \begin{bmatrix} 0 & 1 & 0 \\ 0 & 0 & 1 \\ -b_0 & -b_1 & -b_2 \end{bmatrix}, \ \boldsymbol{A}_q = \begin{bmatrix} 0 & 1 \\ -a_1 & -a_0 \end{bmatrix}. \tag{5.24}$$

For given positive definite symmetric matrices $\boldsymbol{Q}_p$ and $\boldsymbol{Q}_q$, it is straightforward to solve the following Lyapunov equations to obtain positive definite symmetric matrices $\boldsymbol{M}_p \in \mathbb{R}^{3\times3}$ and $\boldsymbol{M}_q \in \mathbb{R}^{2\times2}$ such that

$$\boldsymbol{M}_p\boldsymbol{A}_p + \boldsymbol{A}_p^T\boldsymbol{M}_p = -\boldsymbol{Q}_p, \ \boldsymbol{M}_q\boldsymbol{A}_q + \boldsymbol{A}_q^T\boldsymbol{M}_q = -\boldsymbol{Q}_q.$$

The Lyapunov function V is chosen as

$$V = \boldsymbol{e}_1^T\boldsymbol{M}_1\boldsymbol{e}_1 + \boldsymbol{e}_2^T\boldsymbol{M}_2\boldsymbol{e}_2,$$

with $\boldsymbol{M}_1 = \text{diag}(\boldsymbol{M}_p, \boldsymbol{M}_p)$ and $\boldsymbol{M}_2 = \text{diag}(\boldsymbol{M}_q, \boldsymbol{M}_q)$. With error dynamics, the time derivative of V is

$$\dot{V} = -\boldsymbol{e}_1^T\boldsymbol{Q}_1\boldsymbol{e}_1 - \boldsymbol{e}_2^T\boldsymbol{Q}_2\boldsymbol{e}_2 + 2\left(\boldsymbol{e}_1^T\boldsymbol{M}_1\boldsymbol{D}_1 + \boldsymbol{e}_2^T\boldsymbol{M}_2\boldsymbol{D}_2\right),$$

where $\boldsymbol{D}_1 = [0, 0, (\boldsymbol{p}_p)_1, 0, 0, (\boldsymbol{p}_p)_2]^T$ and $\boldsymbol{D}_2 = [0, (\boldsymbol{p}_q)_1, 0, (\boldsymbol{p}_q)_2]^T$. Let the spectrum radii for matrices $\boldsymbol{M}_p$, $\boldsymbol{M}_q$, $\boldsymbol{Q}_p$, and $\boldsymbol{Q}_q$ be α_p, α_q, β_p and β_q, respectively. The inequality of $\dot{V}$ is obtained as

$$\dot{V} \le -\eta_1\|\boldsymbol{e}_1\|_2^2 - \eta_2\|\boldsymbol{e}_2\|_2^2 + 2\alpha_p c_1\|\boldsymbol{e}_1\|_2 + 2\alpha_q c_4\|\boldsymbol{e}_2\|_2,$$

with $\eta_1 = \beta_p - 2\alpha_p c_2 - \alpha_p c_3 - \alpha_q c_5$ and $\eta_2 = \beta_q - 2\alpha_q c_6 - \alpha_p c_3 - \alpha_q c_5$. Then, for any given positive $d_1, d_2 > 0$, $\dot{V}$ is bounded as

$$\dot{V} \leq -\left(\eta_1 - \frac{\alpha_p^2 c_1^2}{d_1}\right) \|\boldsymbol{e}_1\|_2^2 - \left(\eta_2 - \frac{\alpha_q^2 c_4^2}{d_2}\right) \|\boldsymbol{e}_2\|_2^2 + d_1 + d_2.$$

For a given $c > 0$, $\Omega_V(c)$, $\Omega_V(c) = \{(\boldsymbol{e}_1, \boldsymbol{e}_2) : V(\boldsymbol{e}_1, \boldsymbol{e}_2) \leq c\}$, is a bounded closed set. The set Ω^* is also introduced as

$$\Omega^* = \left\{(\boldsymbol{e}_1, \boldsymbol{e}_2) : \left(\eta_1 - \alpha_p^2 c_1^2/d_1\right) \|\boldsymbol{e}_1\|_2^2 + \left(\eta_2 - \alpha_q^2 c_4^2/d_2\right) \|\boldsymbol{e}_2\|_2^2 = d_1 + d_2\right\}.$$

Therefore, if there exists the positive constants d_1 and d_2 such that $\eta_1 > \alpha_p^2 c_1^2/d_1$, $\eta_2 > \alpha_q^2 c_4^2/d_2$, the errors $(\boldsymbol{e}_1, \boldsymbol{e}_2)$ will converge into the bounded set $\Omega_V(b)$, with

$$b := \arg_{k>0} \sup \left\{k = V(\boldsymbol{e}_1, \boldsymbol{e}_2), (\boldsymbol{e}_1, \boldsymbol{e}_2) \in \Omega^*\right\}.$$

In other words, as $t \to \infty$, $V = \boldsymbol{e}_1^T(t)\boldsymbol{M}_1\boldsymbol{e}_1(t) + \boldsymbol{e}_2^T(t)\boldsymbol{M}_2\boldsymbol{e}_2(t) \leq b$.

5.4.2 Riding performance metrics

Based on the aforementioned stability analysis, the metrics are introduced for evaluating the subjects riding skill. The first metric is given by the BEM. From the analysis in the BEM section, the BEM indeed captures the relationship between the rider trunk roll angle and the bikebot roll angle. It captures both the cases when the rider tries to track any particular path or freely balances the platform. Since its calculation does not need $\boldsymbol{\tau}$, the first balance metric BM_1 is defined as the first component of $\boldsymbol{F}(\boldsymbol{q}, \dot{\psi}, v_r, \boldsymbol{u}, \boldsymbol{\tau})$ under control $\boldsymbol{u}$, namely,

$$BM_1 = F_1(\boldsymbol{q}, \dot{\psi}, v_r, \boldsymbol{u}, \boldsymbol{\tau}). \tag{5.25}$$

Metric BM_1 does not take the consideration of the path-following performance. Considering both the trajectory-tracking and balance tasks, based on the above stability analysis results and define the second balancing-tracking performance metric BM_2 is designed as

$$BM_2 = E_p(\boldsymbol{e}_1) + E_q(\boldsymbol{e}_2) = \boldsymbol{e}_1^T\boldsymbol{M}_1\boldsymbol{e}_1 + \boldsymbol{e}_2^T\boldsymbol{M}_2\boldsymbol{e}_2. \tag{5.26}$$

Clearly, BM_2 uses the both the path-following and the balance performance errors to quantify the riding motor skills. From BM_2, $BM_{21} = \boldsymbol{e}_1^T\boldsymbol{M}_1\boldsymbol{e}_1$ and $BM_{22} = \boldsymbol{e}_2^T\boldsymbol{M}_2\boldsymbol{e}_2$ are introduced for the position errors and balancing errors, respectively.

5.5 Experiments

In this section, under human rider control, several target paths are followed by the rider-bicycle system. According to the collected rider-bicycle system states, the proposed rider controller outputs are calculated and compared with the rider actual operations.

Five subjects (all males with ages: 26.4 ± 2.2, heights 1.75 ± 0.06 m, and weights 65.2 ± 9.6 kg) were recruited for the experiments. All of the participants were chosen from students at Rutgers University and were reported to be in a good health condition. All subjects were reported by themselves to have at least five years' bicycle riding history and were considered as experienced riders. The five target paths and following velocities were chosen as the same as those of the path following experiments in Section 4.4. The paths were marked on the ground. These five subjects were requested to follow the trajectories under the three different velocities as in Chapter 4. Before collecting the data, the riders were allowed to exercise and be familiar with the bikebot and target path. For each experiments condition, one subject repeated three times and all data were recorded.

For each trail, based on the states of the dynamics and the control operation of the riders, the BEM $(\varphi_{be}(t), \varphi_{he}(t))$ is calculated. The position error $e_p(t)$ and the balancing tracking error $(e_{\varphi_b}(t), e_{\varphi_h}(t))$ are also obtained. Combining with the rider operations $(\phi(t), \tau_h(t))$, the rider EIC-based control law $u_\psi^{\text{int}}(t)$ and $u_\tau^{\text{int}}(t)$ are estimated. The balancing metrics can also be calculated for the riding performance evaluation.

Unlike autonomous controls, under the same experimental condition, different rider has different performance. To observe the averages and ranges, the errors mean values and standard derivation of all trails are calculated. The errors of several paths are shown in Fig. 5.2. Similar to Fig. 4.2, the arc-length coordinate is used to plot the Fig. 5.2. The position errors $e_P(t)$ and balancing errors $e_{\varphi_b}(t)$ are plotted. Fig. 5.3 further illustrates the path-following performances on the horizontal plane.

Fig. 5.4 shows an example of one trail result for an '8'-figure trajectory (with 6-m radius) riding experiment. The balancing equilibrium point tracking result is plotted in

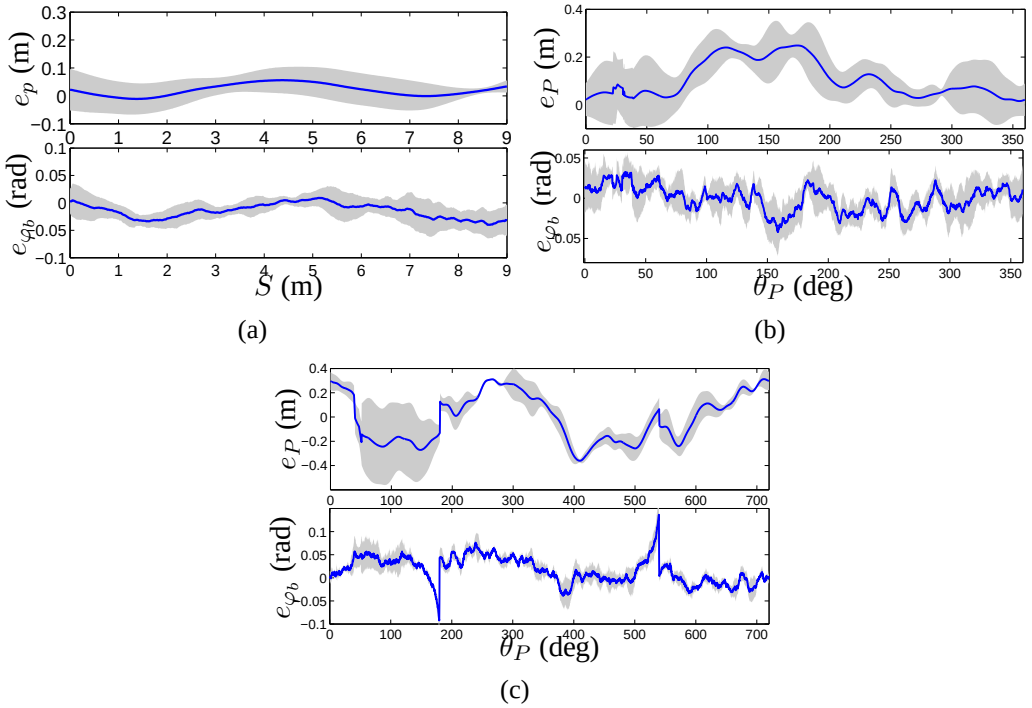

Figure 5.2: Position errors and balancing errors (means and standard derivations) for rider performance: (a) Straight line, middle speed; (b) $R = 6$ m circle, middle speed; (c) $R = 6$ m '8'-figure, middle speed.

Fig. 5.4(a), and the control outputs are shown in Fig. 5.4(b). For effective comparison, we here use the steering angle as the output of the EIC-based controller, rather than u_ψ^{int} in (5.11). The controller output steering angle is denoted as ϕ_c and also plotted in Fig. 5.4(b). ϕ_c is compared to the actual steering angle ϕ. From this figure, $\phi(t)$ follows closely with $\phi_c(t)$. The leaning torque output u_τ^{int} is also near the actual measurement τ_h. From these observations, the actual control by the riders can be considered as to regulate the balancing states near the equilibrium point. Finally, the balancing metrics BM_1 and BM_2 are calculated and plotted in Figs. 5.4(c) and 5.4(d), respectively.

Furthermore, the path-following results under rider control are also compared with the autonomous path-following results in Chapter 4. An example is shown in Fig. 5.5. From Fig. 5.5(a), the path-following performances are similar under the autonomous control and human riding experiments. The rider performance is slightly better than that under the autonomous controller. Fig. 5.5(b) shows the balancing state φ_b and the steering angles. From the figure, the autonomous control has the smoother ϕ profile, which results a smoother

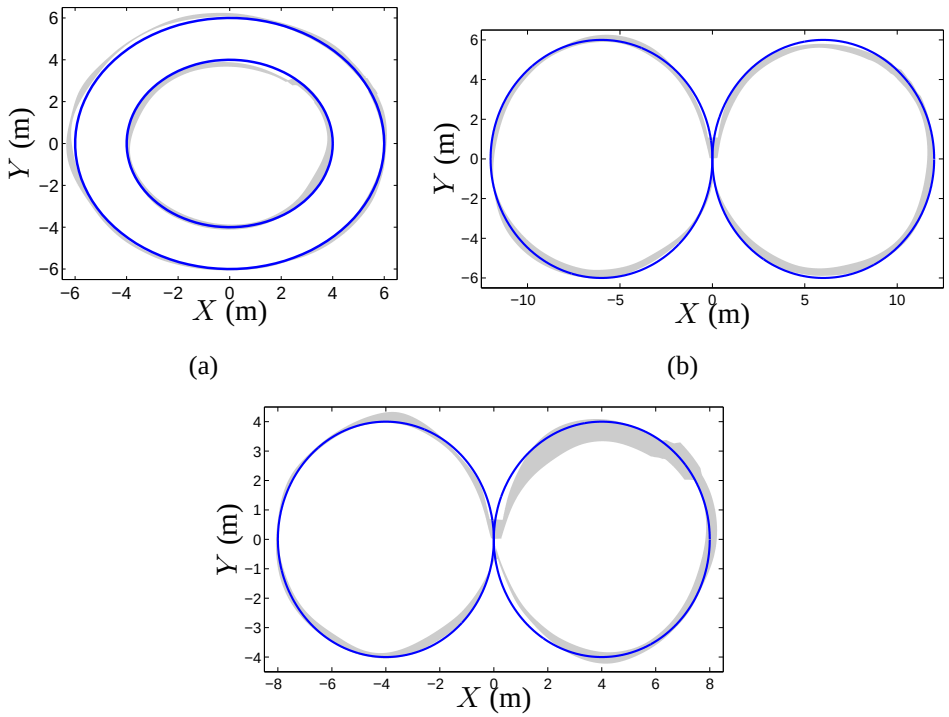

Figure 5.3: Horizontal positions (means and standard derivations) for rider performance:(a) Circle, middle speed; (b) $R = 6$m '8'-figure, middle speed; (c) $R = 4$m '8'-figure, middle speed.

roll motion than those under the human control. This has influences on the position control performance. The high frequency and large amplitude steering operation can adjust the balancing and position errors quickly.

Fig. 5.6 shows performances metrics of both autonomous control and rider control. The balancing metric $|BM_1^*|$ under autonomous control and rider control are plotted in Figs. 5.6(a) and 5.6(d), respectively. In these figures, we use the normalized $|BM_1^*|$ to represent the balance metric $|BM_1|$. $|BM_1^*|$ is obtained by using $|BM_1|$ divided by $m_b h_b$ for autonomous control, and divided by $m_b h_b + m_h(h_s + h_h)$ for rider control. Under the same condition, the mean value of $|BM_1^*|$ under bikebot control is smaller than that under the rider control. Under a given velocity, $|BM_1^*|$ for the straight line has the smallest mean values, and the $|BM_1^*|$ values for the circular trajectories are smaller than those for '8'-figure trajectories. The $|BM_1^*|$ values under larger radius trajectories are smaller than those

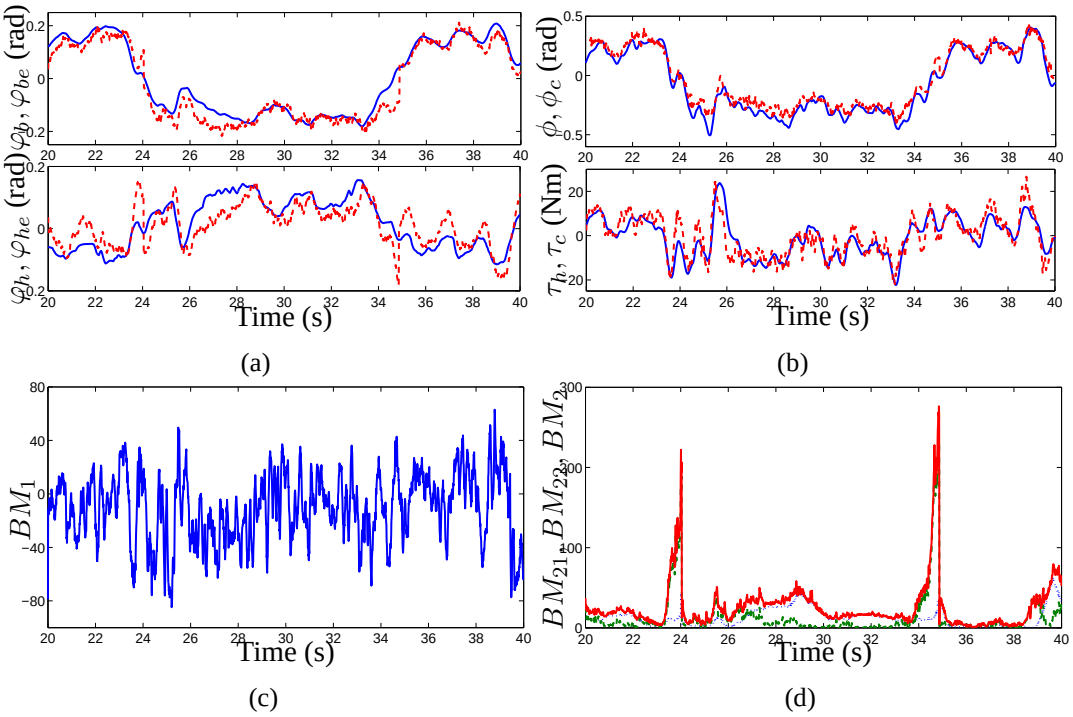

Figure 5.4: Balancing Metrics (means and standard derivations) for rider performance: (a) Balancing states φ_b and φ_h; (b) Control outputs steering angle ϕ and leaning torque τ_h; (c) BM_1; (d) BM_2. (For (a) and (b), Blue solid lines are real measurements, and Red dash lines are calculation results based on EIC-based control structure. For (d), Blue, green and red lines are BM_{21}, BM_{22} and BM_2 respectively.)

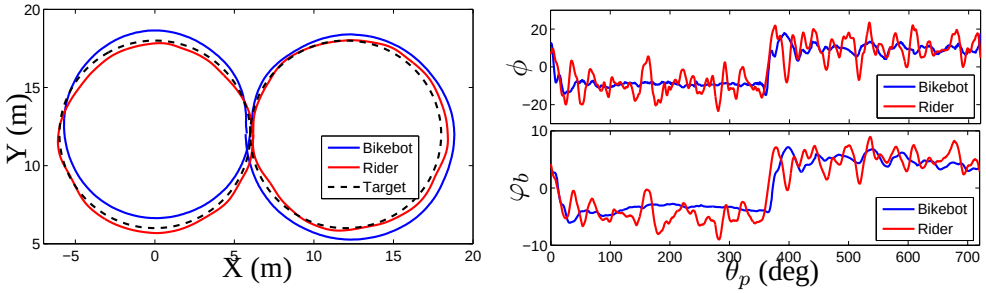

Figure 5.5: Path following comparison of bikebot and human rider (an example of '8'-figure path): (a) horizontal position, (b) steering angle ϕ and rolling angle φ_b.

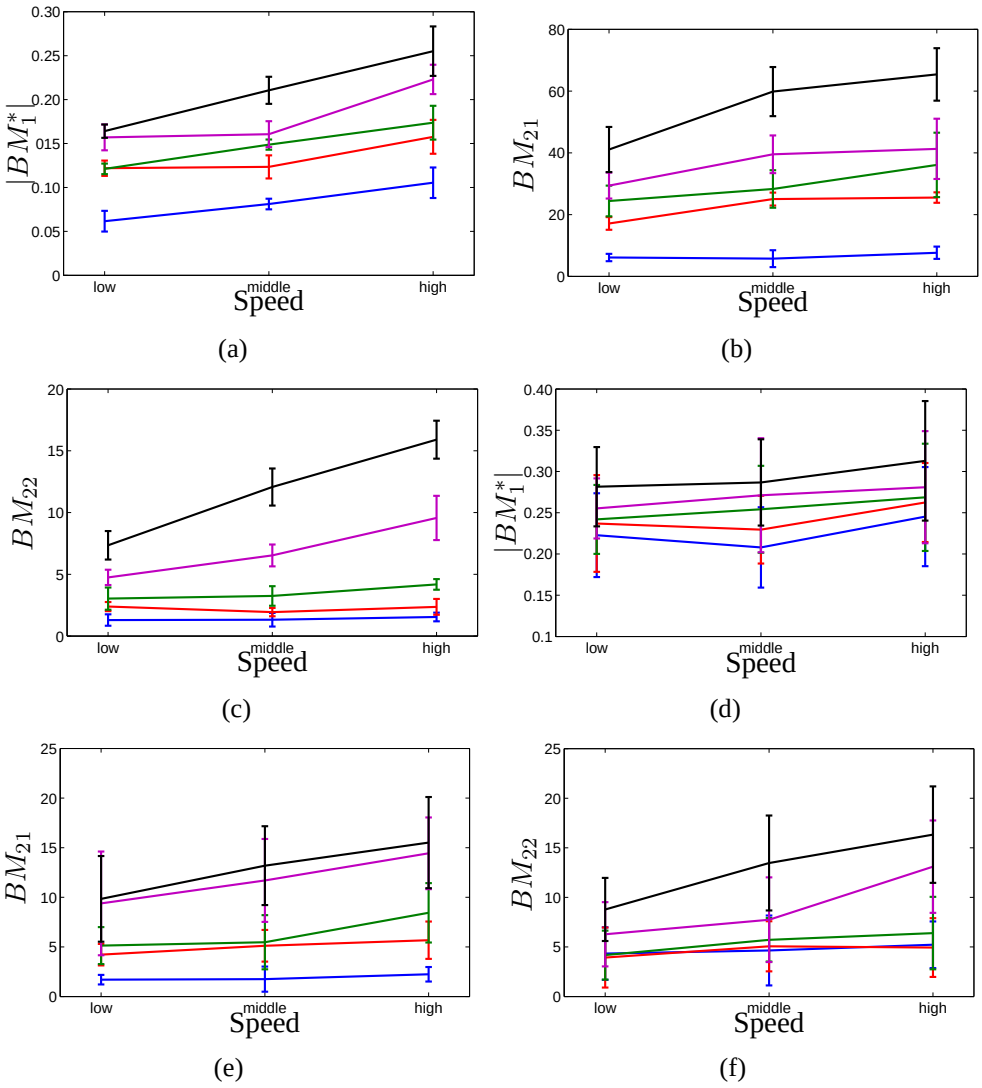

Figure 5.6: Means and standard derivations of performance metrics: (a,d) BM_1, (b,e) BM_{21} and (c,f) BM_{22}. ((a-c): bikebot autonomous riding, (d-f): human rider riding; blue: straight line; red: 6 m radius circle; green: 4 m radius circle; purple: 6 m radius '8'-figure; black: 4 m radius '8'-figure.)

with small radius. Under autonomous control, for a given target path, the metric value is large when the moving velocity is large. However, under rider control, the mean values of $|BM_1^*|$ are slightly smaller in the conditions of middle speed, the straight line, and the circular trajectory with 6-m radius than other experimental conditions.

The balancing-tracking metrics BM_2 are calculated under the same parameters for each case. BM_{21} is for the position errors (Fig. 5.6(b) and 5.6(e)), and BM_{22} is for the balancing errors (Fig. 5.6(c) and 5.6(f)). Similar to $|BM_1^*|$, the mean values of BM_{21} are increased

when the speed is increased or the path radius is reduced. This phenomenon is observed in both autonomous control and rider control conditions. Under rider control, the BM_{21} values are smaller than those under autonomous control. The rider position control results are better than those of autonomous control, especially for the '8'-figure paths with high speed. The changing trend of BM_{22} under various conditions is similar as that of BM_{21}. In these calculations, the metrics' standard derivations of human rider are much larger than those of autonomous control.

5.6 Conclusion

This chapter presented the BEM concept to capture the human balance motor skills in interactions with machines and robots. The bikebot platform was used as a paradigm to illustrate the balance skill and the BEM calculation. The BEM was built on the rider-bicycle dynamics that satisfied the nearly EIC structure. Using the dual convertible property of the EIC system, a feedback linearization controller was designed and its stability was proven. Two BEM-based performance metrics were also proposed and used to capture the balance and path-following skills. The experiments of path-following under rider control were conducted. The rider control operations were compared with the proposed EIC-based rider controller, and the riding performances were evaluated by using several metrics. Furthermore, the riders control results were compared with the autonomous control results those were presented in Chapter 4.

Chapter 6
Control Analysis for Human Balancing Riding

6.1 Introduction

Human balance capability is crucial for many motor skills, such as standing, walking and running, etc. Human physiological delays in sensorimotor feedback increases complexity in analyzing human balancing system. Although many advances have been witnessed in recent years towards understanding human balancing tasks such as stick balancing [69, 70], quiet stance [28, 71, 72], balancing board [73], etc., few studies have been reported in human-machine interactions where human full-body movements play an important role in balancing the entire systems. In this chapter, we take an example of rider-bicycle systems to present stability and control analysis of these human-in-the-loop systems.

Recent clinical studies report that some Parkinsons disease patients who cannot maintain a stance balance and walking balance are able to freely ride bicycles [39, 74]. Bicycle is also considered to be used as a potential postural balance rehabilitation device [38, 40]. Intrinsically unstable bicycles offer a unique platform to study fundamental principles of coupled physical human-machine interactions. Although bicycle dynamics and stability have been studied for a long time (e.g., [16, 75–77]), few studies and experiments are reported to quantify the human balance mechanisms and performance [78]. The goal of this work is to present the stability and control analysis and experiments of the rider-bicycle system under human steering and upper-body balance movements.

Riders balance control mechanism is a combination of perception, decision and manipulation. Neuro-balance control models are reported in literature for human quiet stance. For

example, the model in [28, 79] describes a human feedback mechanism of upper-body upright stance with the identified proprioception, vestibular and visual sensory contributions. The model captures the human sensory responses to environment as short-, medium- and long latency phasic mechanisms due to proprioception, vestibular and visual sensory, respectively. Using this neuro-control model, balance control stability analysis is conducted for riding stationary bicycles [1, 31]. Built on the work in [80], a rider steering model is presented in [81] for bicycle balancing and path-following tasks. Comparing with the human structural model [80, 81], the neuro-balance model in [28, 79] has attractive complementary features for studying rider-bicycle interactions. The model in [28, 79] captures the human neuro-musculoskeletal characteristics such as upper-body movements and time delays, which are important for bicycle riding. This model also captures various human sensorimotor properties and has been further validated through various stance balance experiments. A similar modeling structure and a simplified control mechanism are proposed in [72] for analyzing a balancing board problem. Although qualitative discussions about balance mechanism are presented in [82, 83], no detailed, quantitative stability results of the rider-bicycle system are reported and demonstrated.

The work presented in this chapter complements and extends the above-mentioned human-bicycle balance control analysis and experiments. We develop new models for the rider steering and upper-body movement control strategies. Using these models, we then analyze stability and performance of the rider-bicycle system. The rider-bicycle dynamic model in this chapter is built on and extended by the work of [84]. A PD feedback control law is proposed to describe the riders steering mechanism for balance tasks. Such a neuro-musculoskeletal model is inspired by the work of stance balance strategy in [28, 73]. For validating and understanding these control models, extensive riding experiments are designed using the newly developed bikebot platform. The bikebot is an instrumented bicycle that was designed and built primarily to help understand the human balance motor skills and study physical human-robot interactions [20].

With the above-mentioned models, the closed-loop dynamics of the rider-bicycle systems is captured by nonlinear differential equations with four time delays. We take advantages of the recent advances in analysis tools for the time-delay dynamical systems [85–89] and apply to the linearized dynamics around the equilibrium points. The quasi-polynomial mapping-based root finder (QPMR) [90] is used to compute the right most roots of the closed-loop characteristic equation. The stability results are compared and validated with the experiments.

Besides normal riding condition, we also conduct rider-bikebot riding experiments under three types of disturbances. The external torque disturbance is first introduced by the bikebot's gyro-balancer, the second type of the disturbance is the visual feedback blocking and distortion, and the last type of the disturbance is the steering actuation time delay. One of the motivations to introduce these disturbances in experiments is to excite the rider-bicycle interactions such that the human balance control model can be identified and estimated. The other goals include sensitivity analysis of the model parameters of the identified human sensorimotor balance models. We present the statistical analysis and use the bicycle balance metric developed in [22] and the previous chapter to quantify the human motor skills and performance.

The main contribution of the work are twofold. First, the new sensorimotor models for human steering and upper-body movements extend and complement the existing methods to capture human balance and control strategies. These human control models are validated through experiments and provide enabling tools to analyze human-in-the-loop dynamic systems and their performance. Second, the stability analysis of the rider-bicycle system is new and can be directly used for designing the bicycle-based rehabilitation devices. The perturbed human riding experiments provide a methodology to understand and estimate the sensitivity of the model parameters on human balance performance. The approaches can also be potentially extended to other types of physical human-machine or human-robot interactions.

The rest of the chapter is organized as follows. In Section 6.2, the human balance

control strategy is discussed and stability analysis is also included. Section 6.3 describes the experiments and the methods. Experimental results are presented in Section 6.4 and discussions of the results are included in Section 6.5. Additionally, the control model and stability in the special stationary condition is discussed in Section 6.6. Finally, we summarize the concluding remarks in Section 6.7.

6.2 Human balance control models and stability analysis

In this section, we first present mathematical models for the human steering and the upper-body movement control. These control models are used to represent the rider balance behaviors. We then analyze the stability of the rider-bicycle system using these control models.

6.2.1 Human balance control models

In [1], a human balance model is presented to capture the sensorimotor mechanisms to ride a stationary bicycle. The model was adopted and extended from human stance model in [28]. Fig. 6.1 illustrates the block diagram of the human balance control model in [1]. The model captures the body intrinsic stiffness, short-, medium- and long-term phasic mechanisms due to proprioception, vestibular and visual sensory, respectively. For example, the intrinsic stiffness mechanism provides a proportional torque (i.e., stiffness coefficient K_{in}) to the (relative) roll angle φ_h. The short-latency phasic mechanism (with coefficient B_{sl} and delay τ_{sl}) captures the upper-body tilting velocity $\dot{\varphi}_h$. The short-latency phasic mechanism is based on the proprioception sensory feedback. The medium-latency phasic mechanism (with time delay τ_{ml} and coefficient B_v) generates a torque that is proportional to the upper-body angular velocity $\dot{\varphi}_h$. Finally, the long-latency sensory integration mechanism generates the torque through a neural proportional-integral-derivative (PID) controller with long latency τ_{ll}.

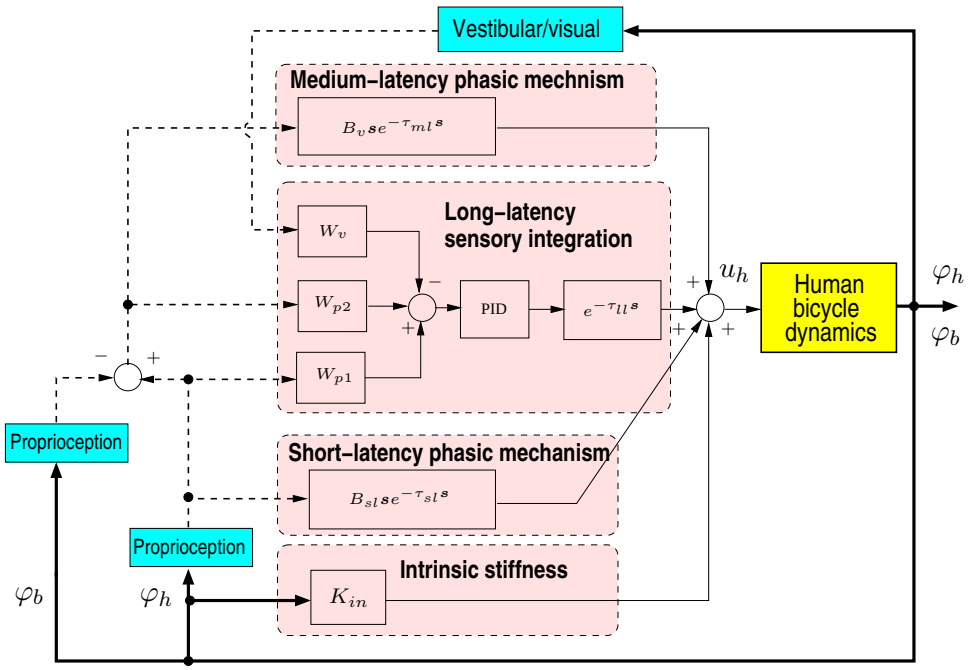

Figure 6.1: A rider's upper-body balance control model [1].

Following the above model for stationary bicycle riding [1], quiet stance [28], and unstable board standing [73], we propose the following model for the upper-body movement balance torque $u_h(t)$

$$\tau_h(t) = k_{h0}\varphi_h(t) + k_{h1}\varphi_b(t-\tau_1) + k_{h2}\dot{\varphi}_b(t-\tau_2) + k_{h3}\varphi_h(t-\tau_1) + k_{h4}\dot{\varphi}_h(t-\tau_2), \quad (6.1)$$

where k_{hi}, $i = 0, \cdots, 4$, are the control gains and $\tau_1, \tau_2 > 0$ are time-delay constants. The control model (6.1) is considered as a similar but simplified structure as the model shown in Fig. 6.1. The first term represents the passive torque proportional to $\varphi_h(t)$ with intrinsic stiffness k_{h0}. The rest four terms in model (6.1) contain the time-delay of the bikebot roll angle φ_b and the upper-body lean angle φ_h and their derivatives. These terms are considered as an alternative and simplified representation of the short-, medium- and long-term phasic mechanisms due to proprioception, vestibular and visual sensory shown in Fig. 6.1. For example, the PD control structure with gains k_{h1} and k_{h3} for position and k_{h2} and k_{h4} for velocity are used to capture the resultant effects of coefficients B_{sl}, B_v, and the PID-gain in the model described in Fig. 6.1. The model (6.1) uses only two time delays τ_1 and τ_2 rather than three in [1, 28] to simplify the analysis. The model (6.1) is validated

by the experimental results in Section 6.3.

For human steering control, we propose a similar PD structure model with two time delays as follows.

$$\phi(t) = \frac{1}{v_r^2}\Big[k_{b1}\varphi_b(t-\tau_3) + k_{b2}\dot{\varphi}_b(t-\tau_4) + k_{b3}\varphi_h(t-\tau_3) + k_{b4}\dot{\varphi}_h(t-\tau_4)\Big], \qquad (6.2)$$

where τ_3 and τ_4 are the time delays constants and k_{bi}, $i = 0, \cdots, 4$, are the constant control gains. Given the double inverted-pendulum model, the human controlled steering angle is related to both the bikebot and the upper-body roll angles. For the upright equilibria, that is, $\varphi_{be}(t) = \varphi_{he}(t) = 0$, each term in (6.2) is indeed the errors $\varphi_b - \varphi_{be}$ or $\varphi_h - \varphi_{he}$ and their derivatives with the time delays. Similar to the model (6.1), the PD feedback structure is used. In [75], the steering angle is also reported to be modeled as the PD structure of the bicycle roll angle and the angular rate for stability analysis. Similar to (6.1) and for simplicity, the time delays in the bikebot and upper-body roll angles terms are the same and also the same time delay for the roll angular velocities.

In the rider-bicycle dynamics, one dominating term is the centrifugal torque that is proportional to $v_r\dot{\psi}$. Given the steering model, the centrifugal torque is proportional to v_r^2 and therefore, the steering model in (6.2) contains the factor v_r^{-2} to compensate for it by the rolling torque. Moreover, we also observe in experiments that with faster moving speed v_r, the steering control is less aggressive and significant and this matches with the mathematical relationship in (6.2). We will also show the experimental validation of the model (6.2) in Section 6.3.

Remark 6.1. *Comparing with the model in [81] with five model parameters for both platform balancing and path-following tasks, the proposed models (6.1) and (6.2) provide additional important features. For example, the proposed models explicitly capture the upper-body leaning motion, which is important for the platform balancing task. The models also explicitly consider the sensorimotor time delays. The existence of time delays in human sensorimotor are observed and considered in various balancing systems [28, 69–73] and we shall consider these delays in bicycle riding task. The rider control models enable*

the stability analysis of the closed-loop systems. Finally, we also conduct the sensitivity study of the model parameters under various sensory feedback disturbances. These are complementary to the results in [81]. Finally, the rider control models are validated by multiple-subject experiments and the results confirm the human riding performance and the models.

Remark 6.2. *We focus on the platform balancing task in this paper and the rider control models are proposed by this consideration. Although they are not extensively validated by path-following experiments, the rider control models in this paper might be possibly modified for path-following task [78]. Indeed, we have presented a nonlinear control design (i.e., EIC-based control) for an autonomous bicycle for path-following task [22]. The rider control outputs (i.e., steering angle) are similar to the EIC-based controller outputs. Extensive validation of the rider control models for path-following performance is out of the scope of this study.*

Remark 6.3. *The steering control model (6.2) takes the steering angle, rather than steering torque, as its output for several reasons. First, due to the geometry parameters and mass distributions, the combination of the bicycle rolling motion and the forward motion generates the steering torque with self-stability property [77]. However in practical rider control scenarios, this torque is not large comparing with the steering friction and rider control torque. The steering dynamics from the rider steering torque input to the steering angle output has the fast responses. For a conventional bicycle, the steering torque due to self-stability has negligible influence for the rider control. The rider can easily control the steering close to the desired motion. Second, the experimental results in Section 6.4 of this chapter and [21] confirm that the steering angle profiles fit well with the output of the proposed steering control model. Indeed, besides our work, other reported control design and experiments such as those in [21, 42] also neglect the steering dynamics and use the steering angle (rather than the steering torque) as the input to obtain satisfactory results. Finally, inclusion of the steering dynamics would increase the complexity of the closed-loop stability analysis and might even prevent from obtaining the stability and parameter*

sensitivity results, which is one of the main goals of this work.

6.2.2 Rider-bicycle system stability

Since the rider-bicycle dynamic model is nonlinear and the human balance models (6.1) and (6.2) contain time-delay terms, the stability analysis is conducted by the linearized dynamics with time delays. The equilibria of the system states are zeros and the linearized dynamics approximately capture the nonlinear stability properties [1, 31].

After plugging (6.1) and (6.2) into the rider-bikebot physical dynamics (2.13), the linearized dynamic models around the equilibria are

$$\ddot{\boldsymbol{q}} + \boldsymbol{T}_2\ddot{\boldsymbol{q}}(t-\tau_4) + \sum_{i=1}^{4}\left[\boldsymbol{B}_i\dot{\boldsymbol{q}}(t-\tau_i) + \boldsymbol{K}_i\boldsymbol{q}(t-\tau_i)\right] + \boldsymbol{K}_0\boldsymbol{q} = \boldsymbol{0}, \tag{6.3}$$

where gain matrix $\boldsymbol{T}_2 \in \mathbb{R}^{2\times 2}$ is introduced by the derivative terms in the steering model, $\boldsymbol{B}_i, \boldsymbol{K}_i \in \mathbb{R}^{2\times 2}$, $i = 0, \cdots, 4$, are the damping and stiffness matrices, respectively. We do not list the detailed lengthy formulation for these matrices.

Defining $\boldsymbol{x} = [\boldsymbol{q}^T, \dot{\boldsymbol{q}}^T]^T \in \mathbb{R}^{4\times 1}$, the closed-loop system dynamics (6.3) becomes

$$\dot{\boldsymbol{x}} + \boldsymbol{D}_2\dot{\boldsymbol{x}}(t-\tau_4) + \boldsymbol{A}_0\boldsymbol{x} + \sum_{i=1}^{4}\boldsymbol{A}_i\boldsymbol{x}(t-\tau_i) = \boldsymbol{0}, \tag{6.4}$$

where

$$\boldsymbol{D}_2 = \begin{bmatrix} \boldsymbol{0}_2 & \boldsymbol{0}_2 \\ \boldsymbol{0}_2 & \boldsymbol{T}_2^T \end{bmatrix},\ \boldsymbol{A}_0 = \begin{bmatrix} \boldsymbol{0}_2 & -\boldsymbol{I}_2 \\ \boldsymbol{K}_0^T & \boldsymbol{0}_2 \end{bmatrix},\ \boldsymbol{A}_i = \begin{bmatrix} \boldsymbol{0}_2 & \boldsymbol{0}_2 \\ \boldsymbol{K}_i^T & \boldsymbol{B}_i^T \end{bmatrix}$$

for $i = 1, \cdots, 4$, and $\boldsymbol{I}_n$ and $\boldsymbol{0}_n$ are the $n \times n$ identity and zero matrices, respectively. Taking the Laplace transformation, the characteristic equation of (6.4) is obtained as

$$\det\left[\left(\boldsymbol{I}_4 + \boldsymbol{D}_2 e^{-\tau_4 s}\right)s + \boldsymbol{A}_0 + \sum_{i=1}^{4}\boldsymbol{A}_i e^{-\tau_i s}\right] = 0, \tag{6.5}$$

where the time delays are introduced in the exponential terms. For presentation convenience, we denote the right most root of (6.5) as λ_0 and we use λ_0 to determine the time-delayed system stability. If the value of the real part of λ_0 is negative, that is, $Re(\lambda_0) < 0$, the closed-loop system is stable. A system with smaller real part values $Re(\lambda_0)$ is considered to be more robustly stable. A quasi-polynomial mapping-based root finder [91] is

used to compute the stability region given by (6.5). We will also use $Re(\lambda_0)$ to illustrate the stability property in later sections.

6.3 Experiments

In this section, we present the experimental setup, description and performance evaluation. The experiments in this study serve for several purposes. The experiments are used to test and validate the rider-bikebot dynamic models and the human balance control models discussed in the previous two sections. Moreover, we conduct experiments to understand and reveal how the parameters of the human steering and upper-body control models change under various riding conditions. Finally, we use the experiments to quantify and evaluate the human riding performance and the stability results.

6.3.1 Riding experiments design

Five subjects were recruited for the experiments. In all tests, the subjects were required to ride the bikebot only for keeping balance on an open parking field without considering the bikebot trajectory. Therefore, path-following was not among the riding objectives. The bikebot was controlled at a constant speed (ranging from 1.7-2.3 m/s and speed variation is less than 0.2 m/s in each test).

The riding experiments were conducted by three groups, following three types of disturbances. The first group was the normal riding with perturbed rolling torques. The rolling torque disturbance was introduced by the gyro-balancer. The subjects were informed the possible rolling disturbance but they did not know when the disturbance was applied. The generated disturbance was an impulse torque by suddenly pivoting of the spinning flywheel. In the second group of experiments, the riders were visually perturbed as well as the external torque disturbances by the gyro-balancer. To generate the visual disturbances, two types of eye glasses were wore by the riders separately. Fig. 6.2(b) shows these two types of eye glasses. The viewed images of the first pair of glasses (called Glasses I) were

partially blocked by translucent tapes. The subjects cannot see the environment objects completely and the sensing images were blocked partially. The images of the second pair of glasses (called Glasses II) were distorted by a set of internal mirrors. The visual horizontal references were also distorted by Glasses II. When the subjects wore Glasses II, they felt dizzy with the distorted images and it took a few hours to get used to it but still with misjudgement sometimes. It is generally considered that Glasses II generate much more visual and perception distortion and disturbance than that of Glasses I.

The third set of experiments were conducted with time-delay disturbances in steering actuation. In these tests, the handlebar and the front wheel frame were mechanically disconnected. The rider rotated the handlebar and the actual steering angle was controlled by the steering motor to track the human input angle with a designed time delay, as shown in Fig. 6.2(a). The goal of this set of experiments is to understand how the steering disturbance and delay affect the riding performance and stability. The time-delay was set initially from 80 ms and incremental delay in each experiment was 50 ms until the subjects cannot maintain balancing properly. These time-delay values are at the same range of the human neuro-controller delays reported in [28].

We label five subjects as A to E. Each subject was asked to ride the bikebot according to the above-mentioned three groups of experiments. Before riding data was collected, each subject was asked to ride the bikebot for about 15 to 30 minutes. Under each experimental condition, the subject was asked to repeat the tests two or three times and all experimental data were recorded and processed. All subjects completed the first group of normal riding experiments and the second group of visual disturbances experiments with wearing Glasses I. However, subject E cannot ride the bikebot while wearing Glasses II. For the third group of riding experiments, subject A can ride and keep balance at time delays 80, 130, 180, and 230 ms, subjects B and C finished successfully with 80, 130, and 180 ms, and subjects D and E can only ride successfully at 80 and 130 ms.

(a) (b)

Figure 6.2: (a) Handlebar and front wheel steering angle sensors and front wheel steering actuator. (b) Visual blocking glasses and mirror glasses.

6.3.2 Riding Performance Metrics

We use the value of $Re(\lambda_0)$ of (6.5) as an indicator to quantify the system stability. To quantify the riding balance skills, we use the BEM concept that was introduced previously as a performance metric. The basic idea of the BEM is to calculate the balanced bicycle and rider upper-body roll angles under the human control.

For given rider steering and pedaling inputs, we compute the required balance torque by the upper-body motion and these torques due to the bicycle roll motion (due to mass center position changes). From the first dynamics equation (2.13), if the difference of the calculated required torque and rider-bicycle rolling torque is zero, the bicycle roll angle φ_b and the rider upper-body roll angle φ_h will maintain their equilibria. The calculation of $F(\boldsymbol{q}, \phi, \dot{\phi})$ captures the net balancing torque for the rider upper-body movement under the equilibrium conditions,

$$\begin{aligned} F\left(q, u_\phi\right) = & -m_b h_b^2 \, \mathrm{s}_{\varphi_b} \, \mathrm{c}_{\varphi_b} \, \dot{\psi}^2 - m_h h_h^2 \, \mathrm{s}_{\varphi_b+\varphi_h} \, \mathrm{c}_{\varphi_b+\varphi_h} \, \dot{\psi}^2 - m_h h_h h_s \, \mathrm{c}_{2\varphi_b+\varphi_h} \, \dot{\psi}^2 \\ & + m_b h_b l_b \, \mathrm{c}_{\varphi_b} \, \ddot{\psi} + m_h h_s l_s \, \mathrm{c}_{\varphi_b} \, \ddot{\psi} + m_h h_h l_s \, \mathrm{c}_{\varphi_b+\varphi_c} \, \ddot{\psi} + m_b h_b \, \mathrm{c}_{\varphi_b} \, v_r \dot{\psi} \\ & + m_h h_s \, \mathrm{c}_{\varphi_b} \, v_r \dot{\psi} + m_h h_h \, \mathrm{c}_{\varphi_b+\varphi_h} \, v_r \dot{\psi} - m_b g h_b \, \mathrm{s}_{\varphi_b} - m_h g h_s \, \mathrm{s}_{\varphi_b} \\ & - m_h g h_h \, \mathrm{s}_{\varphi_b+\varphi_h} - u_\phi, \end{aligned} \tag{6.6}$$

with $u_\phi = (m_b l_b + m_h l_s) \, \frac{g l_t \, \mathrm{c}_\xi}{l} \tan\phi \, \mathrm{c}_{\varphi_b}$.

The smaller value of $|F(\boldsymbol{q}, \phi, \dot{\phi})|$, the closer of the roll angles to their equilibria. Considering the metric $F(\boldsymbol{q}, \phi, \dot{\phi})$ over a time interval $[t_1, t_2]$, we use the following balance

metric (BM) index by averaging over the time duration

$$BM = \frac{1}{t_2 - t_1} \int_{t_1}^{t_2} |F(\boldsymbol{q}(t), \phi(t), \dot{\phi}(t))| dt. \tag{6.7}$$

We compute BM for each subject's experiments. A smaller BM value implies more close to the balance equilibria and therefore, more graceful and skillful in bikebot riding.

6.4 Results

6.4.1 Model validation results

Fig. 6.3 shows the experimental validation for rider-bikebot model. In the figure, we plot the comparison values of the gravitational and the other terms in both equations. Rather than comparing the sums of all the terms with zero in these equations, we here separately consider the gravitational related torque and compare them with the sums of the rest terms because the former is relatively large and therefore, it is more effective to use this comparison for model validation. Fig. 6.3(a) shows the comparison of the first equation and Fig. 6.3(b) for the second equation. The data in these figures are taken from subject A riding experiment and the human torque data τ_h are calculated from the (seat) force sensor measurements [92]. It is clear from these figures that the dynamic model captures the motion and interactions between the rider and the bikebot.

To identify the human steering and upper-body movement models (6.1) and (6.2), we use the collected sensor data in each riding experiment and then a least square method was used to fit the data. For the time delay parameters, they do not appear as the linear terms in the model and therefore, it is difficult to use the least square method to estimate and obtain their values. We first treat and fix these time delays values in their feasible ranges. For example, time delay τ_{s1} is estimated to be in the range of $[0, 500]$ ms and we then search time delay τ_{s1} at $\tau_{s1} = k\Delta T$ s, where $k = 0, \cdots, 50, k \in \mathbb{N}$, and ΔT is the sampling period (in the experiments $\Delta T = 10$ ms). We extend such searching for other time delays. With a fixed time delay in each search iteration, the least square method is

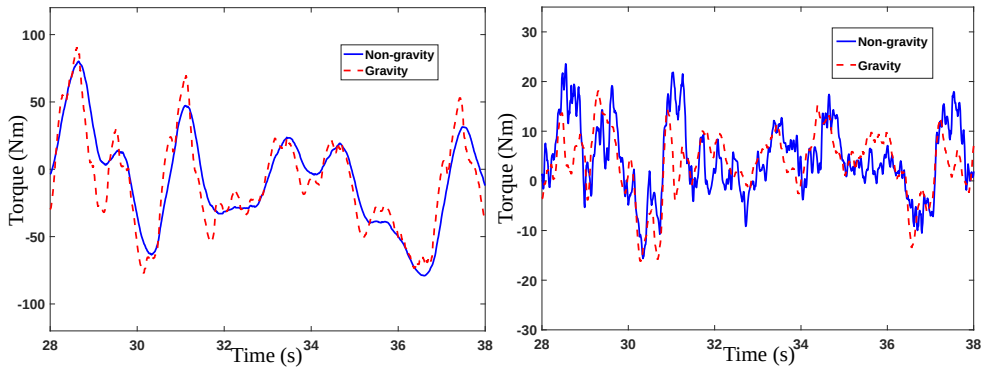

(a) (b)

Figure 6.3: Experimental results for rider-bikebot dynamics models validation. (a) Balancing torques in the first equation of rider-bikebot dynamics. (b) Balancing torques in the second equation of rider-bikebot dynamics.

then used for estimating and obtaining the values of the control gains. For each set of estimated time delays and control gains, we compute the fitting errors. Finally, the set of the parameters that gives the smallest fitting error is chosen as the estimates of the control model parameters.

Fig. 6.4 shows the validation results in one experiment test by subject A. The model parameters were obtained by using the data collected in other experimental runs. The rider operated the bikebot in a straight line like trajectory and the bikebot roll angle was within 0.1 rad; see Fig. 6.4(a). The model predictions of the steering angle ϕ and upper-body movement torque τ_h follow the sensor measurements in experiments. These results confirm the human steering and upper-body movement models. Similar to the dynamic model validation, we also calculated the aggregated relative errors between the model prediction and experiments shown in Fig. 6.4. For most of the riding experiments, the relative errors for the steering angle and upper-body leaning torque are less than 35% and 10%, respectively, for a 10 s time duration as shown in the figure.

We estimate the model parameters in (6.1) and (6.2) for each subject. The parameter values are listed in Table 6.1 for the gains and Table 6.2 for the time delays. In the tables, we include the mean values and standard deviations of each model parameter and time delay. From the magnitudes of these parameters in the tables, we obtain that for the upper-body

movement torque (6.1), the values of passive stiffness parameter k_{h0} are slightly smaller than these of active controlled k_{h3}. Both k_{h0} and k_{h3} are larger than the control gain k_{h1}. Model parameter k_{h2} is also smaller than k_{h4}. Therefore, the rider leaning torque is much more sensitive for the upper-body attitude than the bikebot attitude. The time delay of the steering control has an overall much larger value than that of the upper-body movement, similar to the previously reported results [93] in which the former and latter delays are around 200 and 100 ms, respectively.

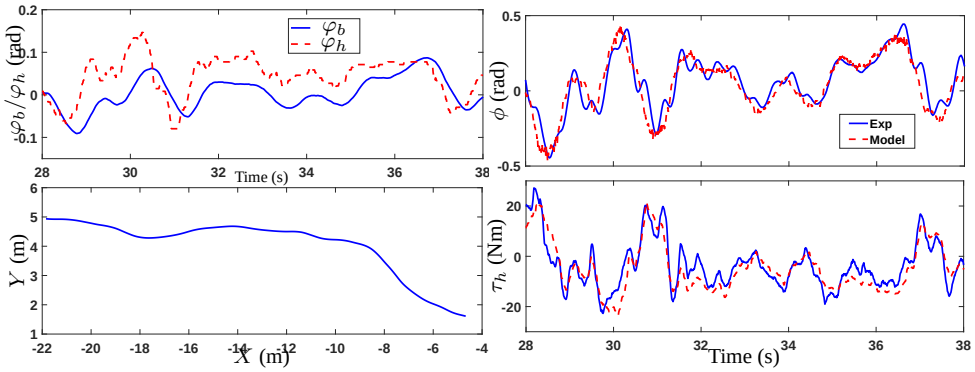

(a) (b)

Figure 6.4: Rider steering and upper-body movement model validation results. (a) Rider upper-body and bikebot roll angle profiles (top plot) and bikebot position trajectory (bottom plot). (b) Validation results for the rider steering control model ϕ in (6.2) (top plot) and the upper-body movement torque model τ_h in (6.1) (bottom plot).

Table 6.1: The mean and standard deviation of the human steering and upper-body movement model parameters.

Gains	A	B	C	D	E
k_{h0}	-96.3 ± 6.03	-97.7 ± 7.50	-99.5 ± 12.0	-81.0 ± 3.82	-80.0 ± 3.54
k_{h1}	-66.2 ± 8.37	-71.5 ± 8.03	-74.6 ± 9.88	-84.0 ± 8.78	-81.9 ± 5.51
k_{h2}	-8.23 ± 0.85	-7.13 ± 6.03	-10.3 ± 1.56	-4.2 ± 1.84	-9.0 ± 0.95
k_{h3}	-139 ± 6.55	-135 ± 3.51	-111 ± 22.6	-85.0 ± 5.66	-75.7 ± 4.96
k_{h4}	-19.6 ± 0.75	-13.0 ± 2.27	17.7 ± 5.87	-11.7 ± 2.40	-16.9 ± 1.31
k_{b1}	10.15 ± 0.54	10.53 ± 0.51	9.13 ± 0.28	10.06 ± 0.15	10.10 ± 0.64
k_{b2}	1.24 ± 0.85	1.13 ± 0.06	1.62 ± 0.269	1.07 ± 0.028	1.61 ± 0.48
k_{b3}	0.90 ± 0.20	0.83 ± 0.06	1.33 ± 0.42	0.79 ± 0.23	1.30 ± 0.28
k_{b4}	0.92 ± 0.36	1.18 ± 0.13	1.01 ± 0.25	1.00 ± 0.28	1.18 ± 0.32

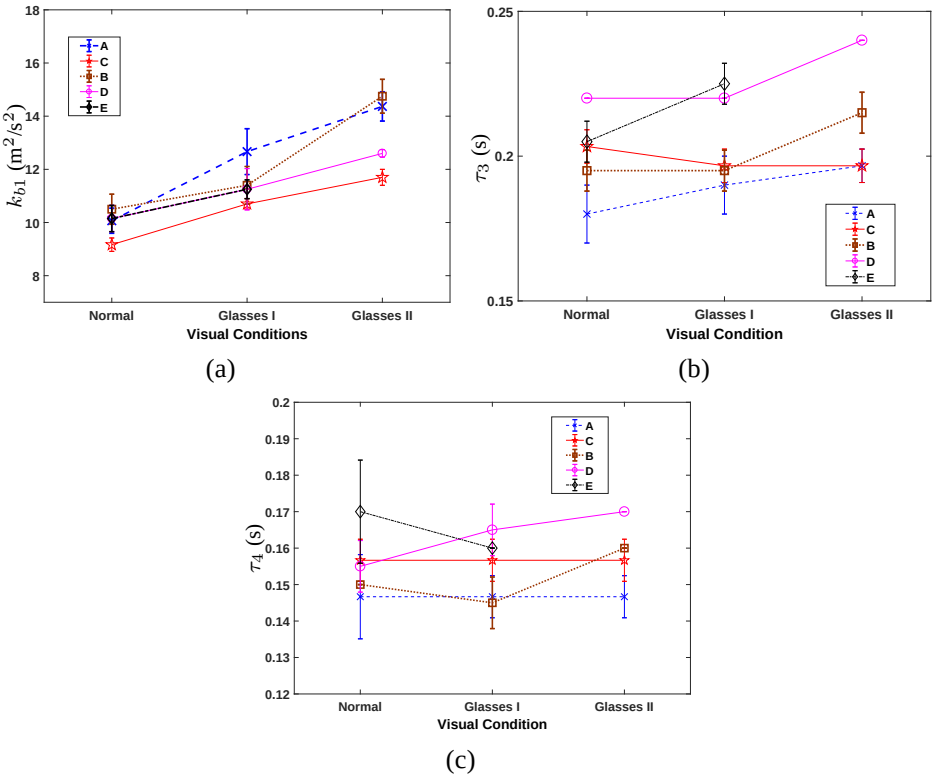

Figure 6.5: Model parameter and time delay variations in experiments with five subjects under different visual conditions. (a) Parameter k_{b1}. (c) Time delay τ_3. (c) Time delay τ_4.

Table 6.2: Identified human upper-body movement and steering control time delays.

Subject	τ_1 (ms)	τ_2 (ms)	τ_3 (ms)	τ_4 (ms)
A	163 ± 6	53 ± 12	200 ± 15	160 ± 11
B	147 ± 12	47 ± 12	190 ± 18	150 ± 13
C	140 ± 0	45 ± 7	190 ± 17	140 ± 17
D	145 ± 7	40 ± 0	170 ± 16	120 ± 12
E	135 ± 14	45 ± 7	130 ± 10	100 ± 6

6.4.2 Control models parameters analysis

The visual disturbances affect the human riding motor behaviors. Out of all control model gains listed in Table 6.1, bikebot roll angle gain k_{b1} has the most significant variation under visual disturbance. Fig. 6.5(a) shows the value change of k_{b1} under normal riding and riding with wearing Glasses I and II respectively for five subjects. It is clearly shown in

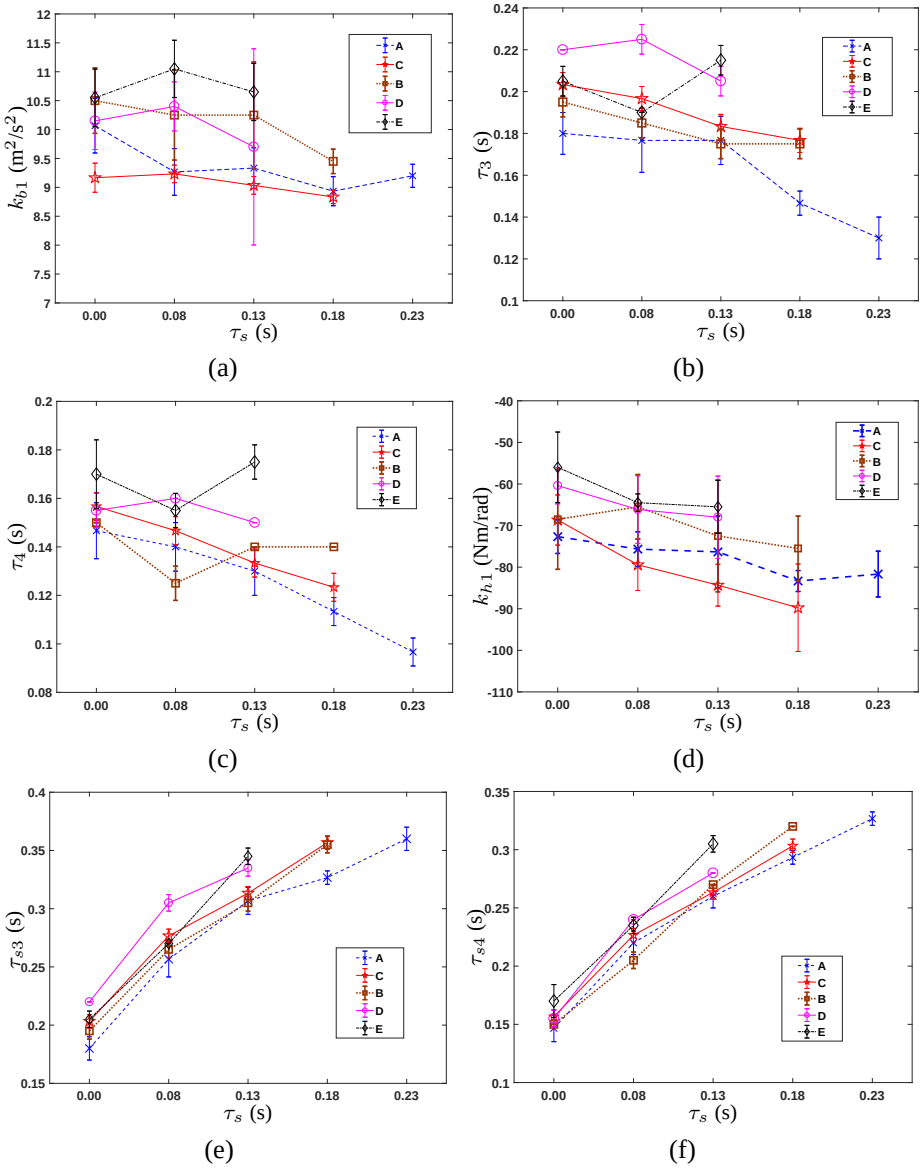

Figure 6.6: Control model parameters and human steering time delays under varying steering actuation delay τ_s. (a) Human steering control gain k_{b1}. (b) Total steering delay τ_{s3}. (c) Total steering delay τ_{s4}. (d) Human upper-body control gain k_{b1}. (e) Human steering control delay τ_3. (f) Human steering control delay τ_4.

these plots that after blocking the visual feedback, the values of gain k_{b1} increase about 0.5-2 consistently for each subject. Moreover, when the subjects wear Glasses II that distort the visual feedback information, the values of k_{b1} increase further about additional 0.5-2 for four out of five subjects. (The fifth subject E cannot ride stably.) Figs. 6.5(b) and 6.5(c) further show the values of time delays τ_3 and τ_4 under visual disturbances.

We ran the F-test (with null hypothesis rejection probability 0.05) of k_{b1} variation under visual disturbances to determine whether the visual conditions changing is the main cause for the parameters variations. The results confirm that the visual conditions significantly influence subjects A, B and C, while the effect was not clearly observed for subject D (subject E failed to ride when wearing Glasses II). We do not find statistically significant changes of other control gains or time delays under visual disturbances.

For the last group of experiments with delayed steering actuation, we denote the steering actuation time delay as τ_s. With human control delays τ_3 and τ_4 in (6.2), the total steering time delays are defined as

$$\tau_{s3} = \tau_3 + \tau_s,\ \tau_{s4} = \tau_4 + \tau_s.$$

Under varying τ_s (i.e., τ_{s3} and τ_{s4}), we have observed the changing values of steering control gain k_{b1} and leaning control gain k_{h1}, and time delays τ_3 and τ_4. These observations are illustrated in Fig. 6.6. We particularly illustrate these parameters because their changes are the most significant.

Fig. 6.6(a) shows a seemingly decreasing trend of the human steering control gain k_{b1} with increasing τ_s. This could imply that the riders enforce the dominating steering gain slightly by noticing the total time delays. However, this decreasing trend is not statistically significant. We have obtained that only subject B shows the significant decrease and all other subjects do not. The absolute values of the human control gain k_{h1} in Fig. 6.6(c) instead show an increasing trend with τ_s. Comparing with the values in normal riding case, the values of $|k_{h1}|$ at $\tau_s = 230$ ms increase about 20 percent. It seems that with an increased τ_s, the riders tried to use their upper-body movement aggressively to keep balancing the platform.

It is interesting to observe the decreasing trends of time delays τ_3 and τ_4 shown in Figs. 6.6(b) and 6.6(c), respectively. We verified this tendency hypothesis by conducting an F-test. For example, for τ_3, the F-test results for subjects A and B are positive. But the results for subjects C, D and E are negative. This result is likely due to the fact that

subjects D and E cannot even ride the bikebot once $\tau_s > 130$ ms. Similarly, for τ_4, the F-test results show that subjects A, B, and C are significant but not D and E. A large value of τ_s implies an increased difficulty of riding bikebot. Only subject A can ride on the bikebot at $\tau_s = 230$ ms. Subjects B and C can still ride the bikebot up to $\tau_s = 180$ ms and D and E at $\tau_s = 130$ ms. Although all subjects have different handling capabilities, it is interesting to note in Figs. 6.6(e) and 6.6(f) that the maximum total time delays τ_{s3} and τ_{s4} of all subjects are about the same, that is, around 350 ms and 400 ms, respectively. These limits are probably the hard capability of the longest steering delay for experienced human riders. It is also interesting to note that during the τ_s-increasing process, the values of delay τ_3 are consistently larger than those of τ_4 around 20 ms.

To analyze the trend across all subjects, Fig. 6.7 shows the mean values and standard deviations of the above-mentioned parameters under varying τ_s and visual conditions. We used the analysis of variance method to compute the mean and variance values for each variable in the figure. We clearly see a decreasing trend for gains k_{b1}, k_{h1}, and time delays τ_3 and τ_4 with increasing τ_s as shown in the top three plots in Fig. 6.7. Under increasing severity of the visual conditions, the values of gain k_{b1} also increase as shown in the bottom plot in Fig. 6.7. We conduct an F-test for the above-mentioned tendency hypotheses and statistically only gain k_{b1} and delay τ_4 show significantly changes under visual disturbance and increasing τ_s, respectively.

We calculate the balance metric BM under different riding conditions and Fig. 6.8 shows the mean and standard deviation values. Fig. 6.8(a) shows BM calculations for all subjects with increasing τ_s. The values of BM clearly increase with τ_s. The BM values are around 20 Nm for most riders (except subject E) at normal riding condition, i.e., $\tau_s = 0$. When $\tau_s = 230$ ms, the BM values increase to around 30-60 Nm. Similarly, the BM values also reach to around 35-50 Nm when the subject wears Glasses II as shown in Fig. 6.8(b). The deteriorated balance performance, that is, increased BM values, under varying riding conditions (either large delay or severe visual distortion) match the riding difficulty reported by the subjects.

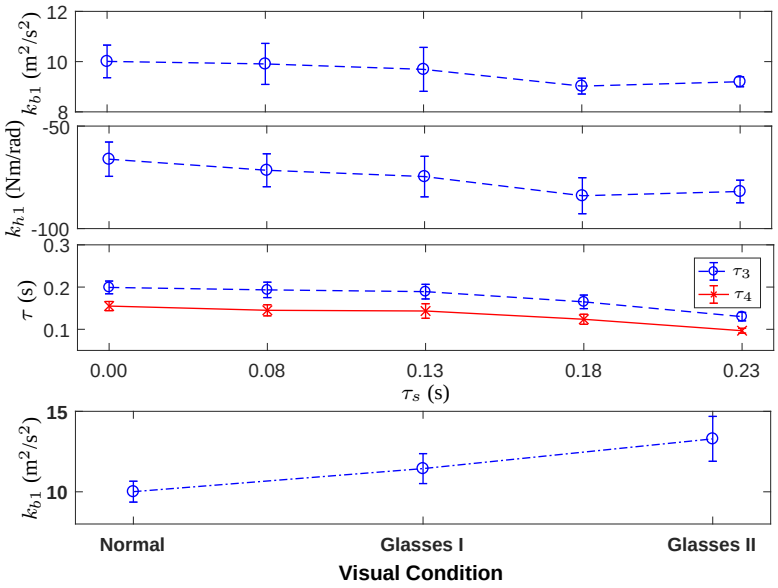

Figure 6.7: Mean values and standard deviations across all subjects with respect to experiments conditions.

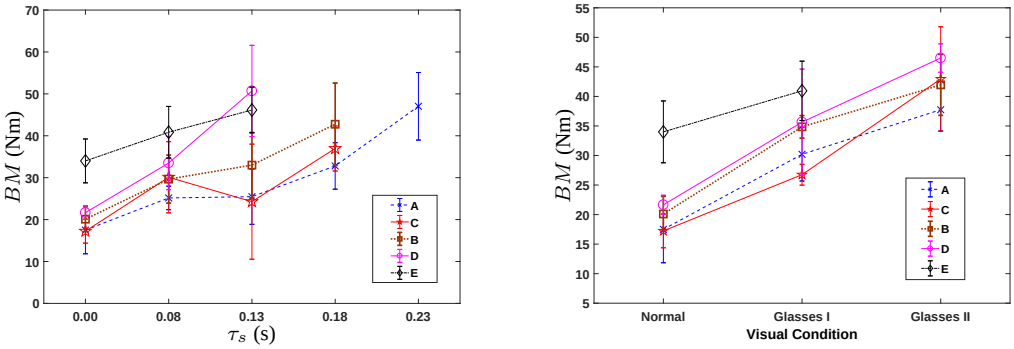

(a) (b)

Figure 6.8: Balance metric BM (mean and standard deviation) for five subjects under (a) varying steering actuation delay t_s and (b) visual conditions.

6.4.3 Stability results

From experiment observations, time delays τ_{s3} and τ_{s4} are critical to system stability. We here choose gains k_{b1} and k_{b2} of the human steering control model (6.2) as an example to illustrate the stability analysis. Fig. 6.9 shows the stability region in the k_{b1}-k_{b2} plane under delay $\tau_{s3} = 200, 300$ and 350 ms. The stability region is defined as $Re(\lambda_0) < 0$ for the roots of (6.5) under changing model parameters, in this case, k_{b1} and k_{b2}. The values of all other model parameters and delays are listed in Tables 6.1 and 6.2. From Note that by Fig. 6.6(e), the range of $\tau_{s3} \in [200, 350]$ ms corresponds to steering delay $\tau_s \in [0, 230]$

ms. Besides the plotted regions (as solid red lines) by using the mean values of all model parameters and delays, we also include the stability regions using the sets of the model parameters one standard deviation smaller (green dot lines) and larger (blue dash lines) than the mean values.

Fig. 6.9(a) shows the stability region when $\tau_{s3} = 200$ ms, that is, zero delay $\tau_s = 0$, while Figs. 6.9(b) and 6.9(c) for $\tau_{s3} = 300$ ms and $\tau_{s3} = 350$ ms, respectively. By comparing these figures, we clearly observe that: (1) with increasing τ_s, the size of the stability region reduces as shown from $\tau_s = 0$ (i.e., $\tau_{s3} = 200$ ms) in Fig. 6.9(a) to $\tau_s = 230$ ms (i.e., $\tau_{s3} = 350$ ms) in Fig. 6.9(c). This is reasonable since it is more difficult for a rider to balance a bikebot with a long steering delay than that with a short delay; (2) It is interesting to see the identified (k_{b1}, k_{b2}) locations for each individual subject are relative to the boundaries of the stability regions in the figure: with increasing delays, the subjects' balance performance became deteriorated and in the case of $\tau_s = 230$ ms in Fig. 6.9(c), all subjects performed closely around the stability region boundary. This is not surprised since as shown in Fig. 6.6(e), $\tau_{s3} = 350$ ms ($\tau_3 = 230$ ms) is the maximum total (actuation) delay that all subjects can handle without loss of balance in the riding experiments.

Similar to Fig. 6.9 to show the stable regions under different values of the control gains, Fig. 6.10 illustrates the stable region in the $\tau_{s3} - \tau_{s4}$ plane along with all the subject time delays. The plots are split into three groups according to the introduced three τ_{s3} ranges between 160 and 400 ms. The figures give an estimation of the ranges of the time delays τ_{s3} and τ_{s4} for system stability and also the observed subjects time delays. We also see that for almost all experiments, the subject time delays are located within but close to the stable region boundaries.

The values of $Re(\lambda_0)$ with varying τ_{s3} and τ_{s4} are shown in Fig. 6.11(a). From this figure, the values of $Re(\lambda_0)$ are much more sensitive with τ_{s3} (τ_3) rather than τ_{s4} (τ_4). Variable $Re(\lambda_0)$ has the minimum value at around $\tau_{s3} = 330$ ms. The stability region is plotted in Fig. 6.11(d) and from the figure, the maximal value of τ_{s3} for a stable closed-loop system is about 375-380 ms. This result is consistent with the experiment observation

shown in Fig. 6.6(d). In the experiments, no subject can control and balance the bikebot when $\tau_{s3} > 400$ ms and the maximum total delay τ_{s3} for all subjects is about 350 ms.

To clearly see the dependency of control gain k_{b1} on delay τ_{s3}, Fig. 6.11(b) shows the $Re(\lambda_0)$ values as varying k_{b1} and τ_{s3} and Fig. 6.11(e) illustrates the stability region in the k_{b1}-τ_{s3} plane. The stability region clearly confirms that the value of k_{b1} is reduced when delay τ_{s3} increases. Figs. 6.11(c) and 6.11(f) show the $Re(\lambda_0)$ and the stability regions under varying τ_1 and τ_2 with zero delay τ_s. For the pair (τ_1, τ_2) by which the system is stable as shown in Fig. 6.11(f), the values of $Re(\lambda_0)$ have no significant change. This implies that system stability is not sensitive for (τ_1, τ_2) in these ranges. The values of $Re(\lambda_0)$ and the stability regions of varying gains k_{h1} and k_{h2} are demonstrated in Figs. 6.12(a)-6.12(b) respectively for $\tau_{s3} = 200$ and 350 ms. The stability regions are highly influenced by τ_{s3} and τ_{s4}. With large time delays, the control gain k_{h1} is bounded and the absolute values of k_{h1} from the experiments in Fig. 6.6(d) show an increasing and bounded trend as well.

6.5 Discussions

The human upper-body movement model (6.1) includes only the dependency on bikebot and upper-body roll angles and their derivatives. Some other influencing factors are neglected in this model. For instance, different from the quiet stance, the moving bikebot is a non-inertial frame and thus, the Coriolis and centrifugal accelerations have influences on the applied balance torques. At low moving velocities, yaw angle ψ does not change dramatically and the term $\dot{\psi}^2$ can be neglected. We also neglect the possible influence of the steering action on the upper-body movement torque τ_h in the model.

We compare the human model parameters in bikebot riding with the stationary riding experiments in [31] and the stance experiments in [28]. First, the observed time delays are not the same values as these in [28, 31]. In [28, 31], three time delays, i.e., short-, medium- and long-latency processes, are introduced in the model with the mean values around 21, 131 and 288 ms, respectively. The short- and medium-latency processes are

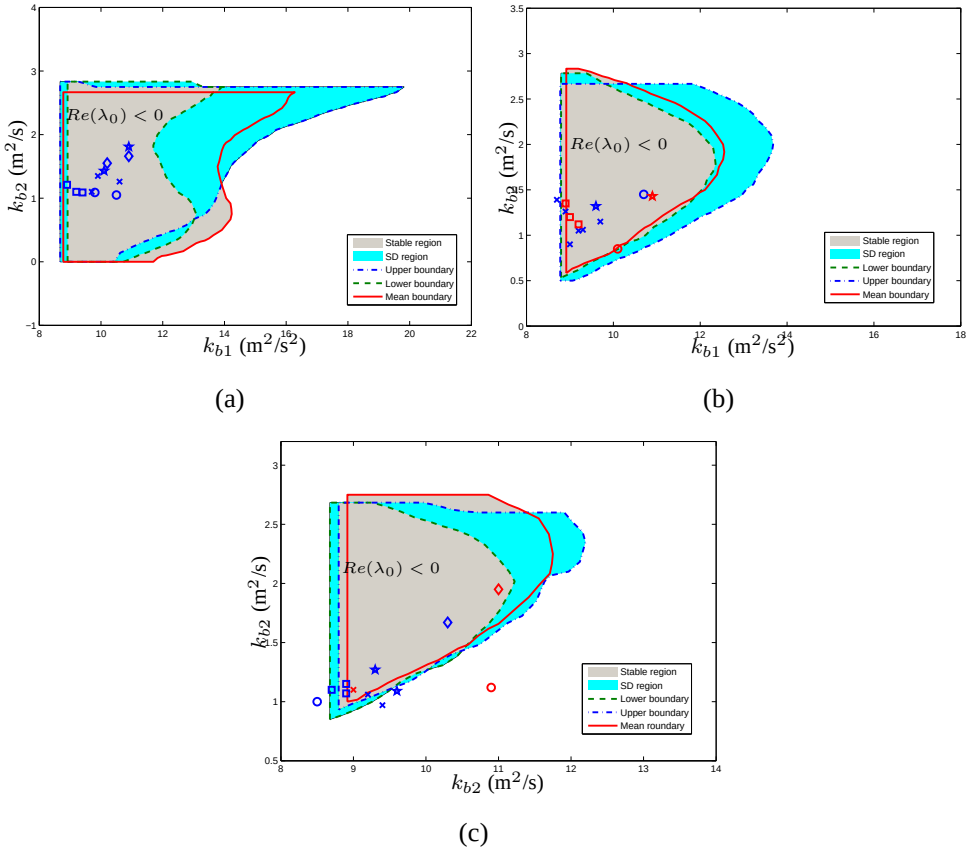

Figure 6.9: Stable region in the k_{b1}-k_{b2} plane at different steering actuation delays. (a) $\tau_{s3} = 200$ ms. (b) $\tau_{s3} = 300$ ms. (c) $\tau_{s3} = 350$ ms. Red solid curve indicates the stable region calculated by the mean values of the control model parameters, green dot and blue dash curves indicate the stable regions calculated by the one standard deviation below and above the mean values of all model parameters, respectively. The different area generated by lower and upper boundary are the bright green region. The point in grey region belongs to one of the areas generated by mean, lower and upper boundaries. Individual dot represents each subject experiment test. "$\times$", "$\square$","$\star$", "$\circ$" and "$\diamond$" marks indicate subjects A to E, respectively. Blue and red marks indicate the stable and unstable parameters point respectively.

based on the angular velocity feedback, while the long-latency process combines the PID feedbacks. In the model given by (6.1), only two time delays τ_1 and τ_2 are used. The feedback signals with τ_2 can be considered as the combination of the short- and medium-latency and the derivative part of the long-latency process. The estimated value of τ_2 is around 40 ms, which is between the short- and medium-latency time delays values in [28]. The estimated value of τ_1, as the long-latency proportional part, is about 160 ms, which is

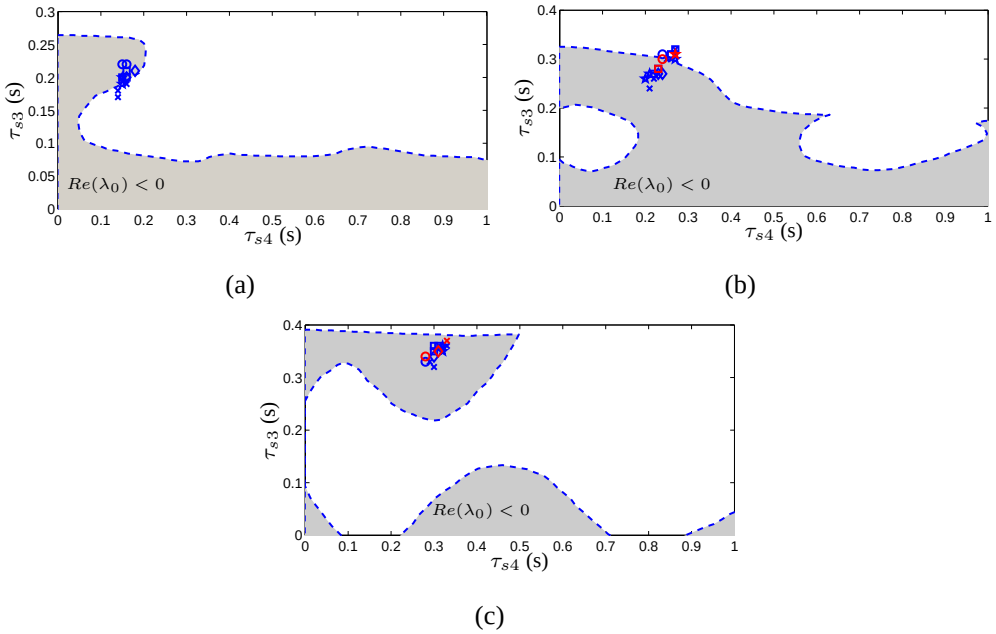

Figure 6.10: Stable region in the τ_{s4}-τ_{s3} plane at different steering actuation delays. (a) $\tau_{s3} \in [160, 240)$ ms. (b) $\tau_{s3} \in [240, 320)$ ms. (c) $\tau_{s3} \in [320, 400]$ ms. Grey area indicates the stable region calculated by the mean values of the control model parameters. (All experiments trails are divided into 3 sets corresponding these τ_{s3} intervals. In every group, the average value of the upper-body time delays and all the control gains generate the grey areas.) In the figures, individual dot represents each subject experiment test. "$\times$", "$\square$","$\star$", "$\circ$" and "$\diamond$" marks indicate subjects A to E, respectively. Blue and red marks indicate the stable and unstable parameters point respectively.

smaller than that of long-latency time 288 ms in [28]. The estimated value of the upper-body passive stiffness k_{h0} (see Table 6.1) in the bikebot riding experiments is larger than that of $K_{in} = 73.5$ Nm/rad in [28], where the proportional control gain k_{h3} is close to the value of $K_{in} = 149$ Nm/rad in [28]. The value of the upper-body angular velocity control gain k_{h4} is smaller than that of $B_{sl} + B_v = 45.6$ Nm/rad in the stance model.

From Table 6.1, the value of gain k_{b1} for bikebot roll angle φ_b is much larger than that of gain k_{b3} for the upper-body roll angle φ_h. The angular velocity gains k_{b2} and k_{b4} are within a similar range. Considering the magnitudes of φ_b, φ_h and their derivatives, the dominating term of (6.2) is the first one, that is, $k_{b1}\varphi_b$. This implies that the roll angle φ_b plays a more important role for balancing the platform than φ_h does. From Table 6.2, the values of time delays τ_3 (angular feedback) and τ_4 (angular velocity feedback) in the human steering control are about (around 50 and 100 ms) larger respectively than those

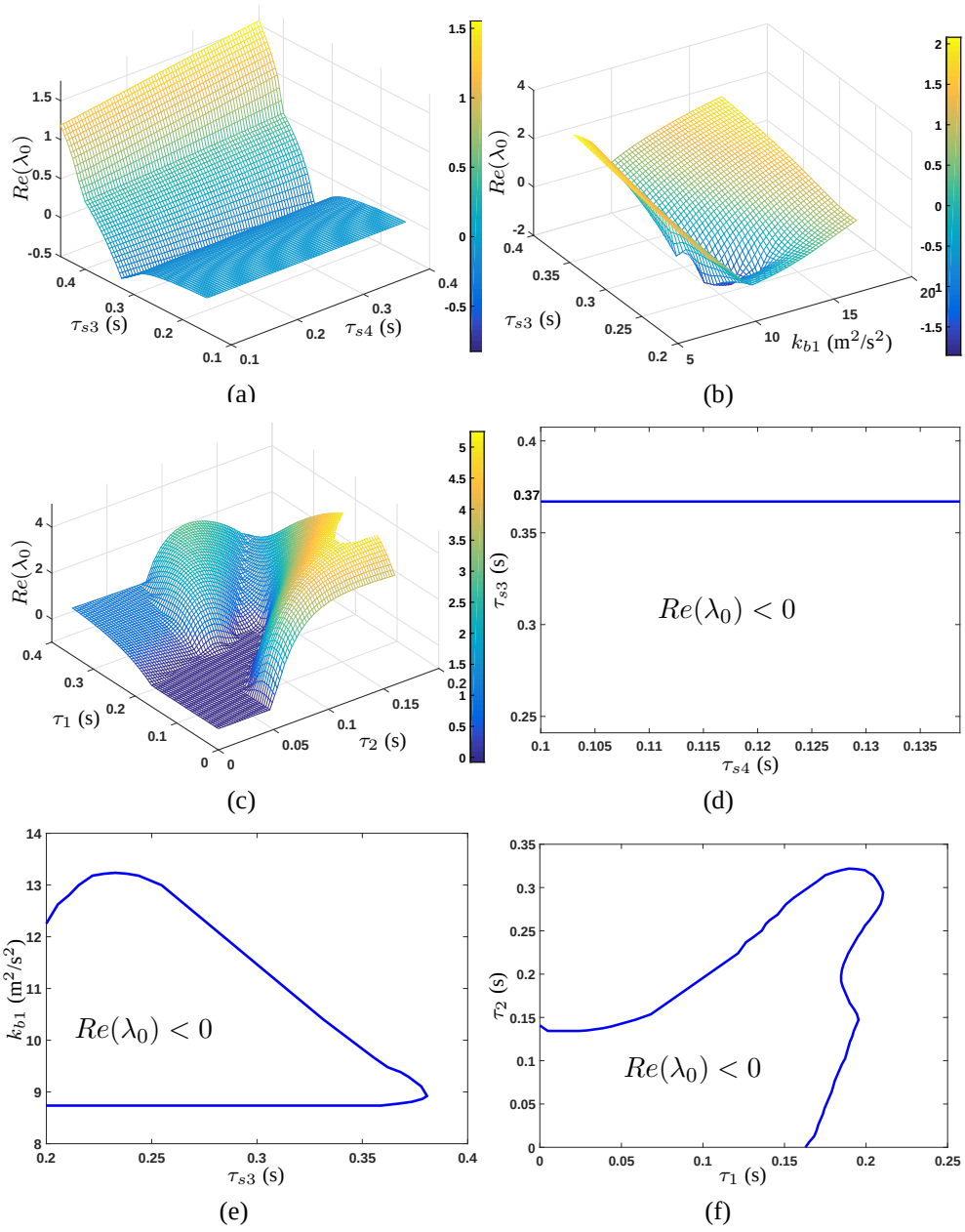

Figure 6.11: Stability regions under different model parameters and delays. $Re(\lambda_0)$ values under varying (a) τ_{s3} and τ_{s4}. (b) k_{b1} and t_{s3}. (c) τ_1 and τ_2. Stability regions under varying (d) τ_{s3} and τ_{s4}. (e) k_{b1} and τ_{s3}. (f) τ_1 and τ_2. In (d)-(f), stable regions are marked with $Re(\lambda_0) < 0$.

of τ_1 and τ_2 in the human upper-body movement model. A possible explanation of these differences is that the human sensorimotor mechanism for steering actuation has a slower response than that of the upper-body movement. This is reasonable since the upper-body movement is directly controlled by the neuromuscular system (i.e., controlled torques) and

the steering actuation is through the limb movements (i.e., controlled angles) with possible longer time delays.

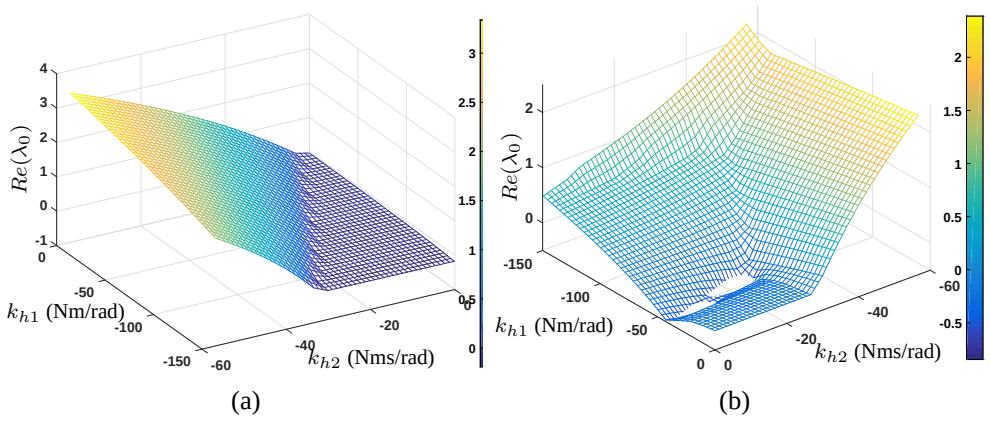

Figure 6.12: $Re(\lambda_0)$ values under varying k_{h1} and k_{h2} with (a) $\tau_{s3} = 200$ ms and $\tau_{s4} = 160$ ms and (b) $\tau_{s3} = 350$ ms and $\tau_{s4} = 310$ ms.

To observe the influence of steering delays on τ_1 and τ_2, Fig. 6.13 illustrates the stability regions in the τ_1-τ_2 plane under four different pairs of (τ_{s3}, τ_{s4}): $(200, 160)$, $(250, 210)$, $(300, 260)$, and $(350, 310)$ ms, respectively. We choose these pairs of (τ_{s3}, τ_{s4}) values because the adjacent pairs are 50-ms incremental each other and the starting pair is around $\tau_s = 0$. From the figure, the stability region is enlarged for the large values of (τ_{s3}, τ_{s4}). The maximum value of τ_1 has increased almost around 50 ms for each incremental pair of (τ_{s3}, τ_{s4}) but the maximum values of τ_2 do not change significantly under varying (τ_{s3}, τ_{s4}). The identified values for τ_1 and τ_2 listed in Table 6.2 all fall into the stability regions and indeed these values do not change much when the steering delay τ_s was introduced in experiments. This could imply that the human riders prefer to use and adopt faster steering actions, rather than upper-body movement, to respond the time delays produced by the actuator. This observation is consistent with the sensitivity analysis reported in [22].

Comparing with other sensing modality, the visual feedback is important for bikebot balance control. The visual sensing is critical for the rider to obtain the bikebot roll angle φ_b estimation. Proprioception sensing is used by the rider to detect the body joints angles and then to estimate the upper-body roll angle φ_h. The vestibular feedback allows subjects to obtain the absolute roll movements. It is possible that other human sensing capabilities

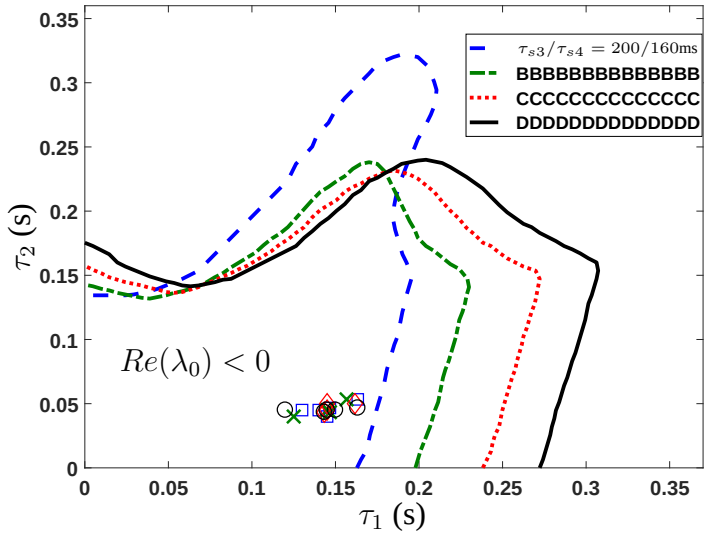

Figure 6.13: Stability regions under under varying τ_1 and τ_2 with different delays τ_{s3} and τ_{s4}. The stable region is marked with $Re(\lambda_0) < 0$. Blue "□", green "×", red "◇", and black "○" marks indicate the estimated mean values of (τ_1, τ_2) for each subject under these four pairs of time delay combinations τ_{s3}/τ_{s4}, respectively.

(e.g., force) can also provide indirect attitude or pose estimation [92]. However, these perceptions sensory feedbacks cannot be used to completely replace the visual feedback. As shown in Fig. 6.5, one subject cannot ride the bikebot after wearing Glasses II. This observation confirms that visual feedback plays a critical role in bikebot riding. On the other hand, all five subjects can balance the bikebot even with partially visual blocking or distortion and four of them can ride with wearing Glasses II. This implies that other perceptions capabilities aforementioned can partially substitute the visual feedback to achieve balance motor skills. Meanwhile, as an evidence, the value of upper-body movement control gain k_{b1} increases when the visual feedback information is partially lost (by Glasses I) and then further grows when wearing Glasses II. The trend of the increased upper-body movement control gain complements the visual feedback loss. This is similar to the experiments observation reported in [28].

The work in this study has several limitations. First, we only recruited experienced bicycle riders as the subjects and it is not clear whether the presented results can be extended and applied to other types of bicycle riders. Second, the results do not include detailed stability analysis of the influence of bikebot velocity v_r. Finally, this paper does

not consider and discuss how to tune and adapt the human motor skills through the physical rider-bikebot interactions. Indeed, all these limitations are among the ongoing research directions and we will report the new developments in future publications.

6.6 Balancing stability under zero speed

For the stationary balancing, the upper-body leaning torque control model τ_h is same as (6.1) in the moving case. Modified from (6.2), the steering model is considered as

$$\phi(t) = k_{b1}\varphi_b(t-\tau_3) + k_{b2}\dot{\varphi}_b(t-\tau_4) + k_{b3}\varphi_h(t-\tau_3) + k_{b4}\dot{\varphi}_h(t-\tau_4). \tag{6.8}$$

Plugging (6.1) and (6.8) into the rider-bicycle balance dynamics, we have the linearized closed-loop dynamic models around the equilibria as

$$\ddot{\boldsymbol{q}} + \sum_{i=1}^{4} \left[\boldsymbol{B}_i^* \dot{\boldsymbol{q}}\left(t-\tau_i\right) + \boldsymbol{K}_i^* \boldsymbol{q}\left(t-\tau_i\right)\right] + \boldsymbol{K}_0^* \boldsymbol{q} = \boldsymbol{0}. \tag{6.9}$$

$\boldsymbol{B}_i^*, \boldsymbol{K}_i^*, \boldsymbol{K}_0^* \in \mathbb{R}^{2\times 2}$, $i = 1, \cdots, 4$, are the damping and stiffness matrices, respectively. Introducing $\boldsymbol{x} = [\boldsymbol{q}^T, \dot{\boldsymbol{q}}^T]^T$, (6.9) becomes

$$\dot{\boldsymbol{x}} + \boldsymbol{A}_0^* \boldsymbol{x} + \sum_{i=1}^{4} \boldsymbol{A}_i^* \boldsymbol{x}(t-\tau_i) = \boldsymbol{0}, \tag{6.10}$$

where

$$\boldsymbol{A}_0^* = \begin{bmatrix} \boldsymbol{0}_2 & -\boldsymbol{I}_2 \\ (\boldsymbol{K}_0^*)^T & \boldsymbol{0}_2 \end{bmatrix}, \boldsymbol{A}_i^* = \begin{bmatrix} \boldsymbol{0}_2 & \boldsymbol{0}_2 \\ (\boldsymbol{K}_i^*)^T & (\boldsymbol{B}_i^*)^T \end{bmatrix}$$

for $i = 1, \cdots, 4$. Taking the Laplace transformation, the characteristic equation of (6.10) is obtained as

$$\det\left(\boldsymbol{I}_4 s + \boldsymbol{A}_0^* + \sum_{i=1}^{4} \boldsymbol{A}_i^* e^{-\tau_i s}\right) = 0. \tag{6.11}$$

The QPMR tool is also used to compute the stability region. The control gains and time delays of the control models (6.8) and (6.1) are estimated and listed in the following: $k_{h0} = -228.6$ N/rad, $k_{h1} = -2482.1$ N/rad, $k_{h2} = -305.5$ Ns/rad, $k_{h3} = -2253.5$ N/rad, $k_{h4} = -108.7$ Ns/rad, $k_{b1} = -523.0$, $k_{b2} = -81.5$ s, $k_{b3} = -202.6$, $k_{b4} = -24.4$ s, $\tau_1 = 60$ ms, $\tau_2 = 10$ ms, $\tau_3 = 180$ ms, and $\tau_4 = 90$ ms.

We here briefly analyze the system stability around these parameter values. First, under zero time delays $\tau_i = 0$, $i = 1, \cdots, 4$, the closed-loop system is controllable under (6.8) and (6.1) with these gains values listed above. By using the QPMR method, the stable regions for time delays parameters are calculated. We also compute $Re(\lambda_0)$ under varying model parameters. Moreover, under the given control gains and time delays, the closed-loop system is stable at the upright position. Comparing with the moving bicycle experiments, the control gain values are much larger and the time delays are smaller. This could be explained by several factors. Without yaw motion, the balancing torque generated by steering motion is given only by u_ϕ. For a given steering angle, the value of u_ϕ is much smaller than the balancing torque generated by yaw motion of the under moving platform. For the stationary case, the upper-body movement contributes more for balancing the platform than the steering actuation. Therefore, the control gain values of the steering and upper-body movement torque models have large values in stationary case. Moreover, the system is much more sensitive for the time delays in stationary case than the moving platform because the balance response needs to be faster than that under the moving platform.

Fig. 6.14 illustrates the control parameters sensitivity for stability and stable regions. Figs. 6.14(a) and 6.14(b) show the changes of $Re(\lambda_0)$ values with time delay pairs (τ_3, τ_4) and (τ_1, τ_2), respectively, while Figs. 6.14(e) and 6.14(f) illustrate the stable regions over time delays in models (6.8) and (6.1), respectively. Clearly, these figures show that $Re(\lambda_0)$ values change dramatically near the stable boundaries shown in Figs. 6.14(e) and 6.14(f). This implies that the system stability is sensitive with the time delays near the boundaries. Comparing with the regions in the moving bicycle case, the stable regions are smaller in size. For example, the maximum value of τ_1 is less than 10 ms. For the steering control, under a given τ_3 the stable interval of τ_4 values is small. Figs. 6.14(c) and 6.14(d) show the $Re(\lambda_0)$ values under pairs (k_{b1}, k_{b2}) and (k_{h1}, k_{h2}), respectively, and their stable regions are demonstrated in Figs. 6.14(g) and 6.14(h) accordingly. Near the boundaries, the $Re(\lambda_0)$ value does not change significantly rapid with these control gains as those for time delays in Figs. 6.14(a) and 6.14(b).

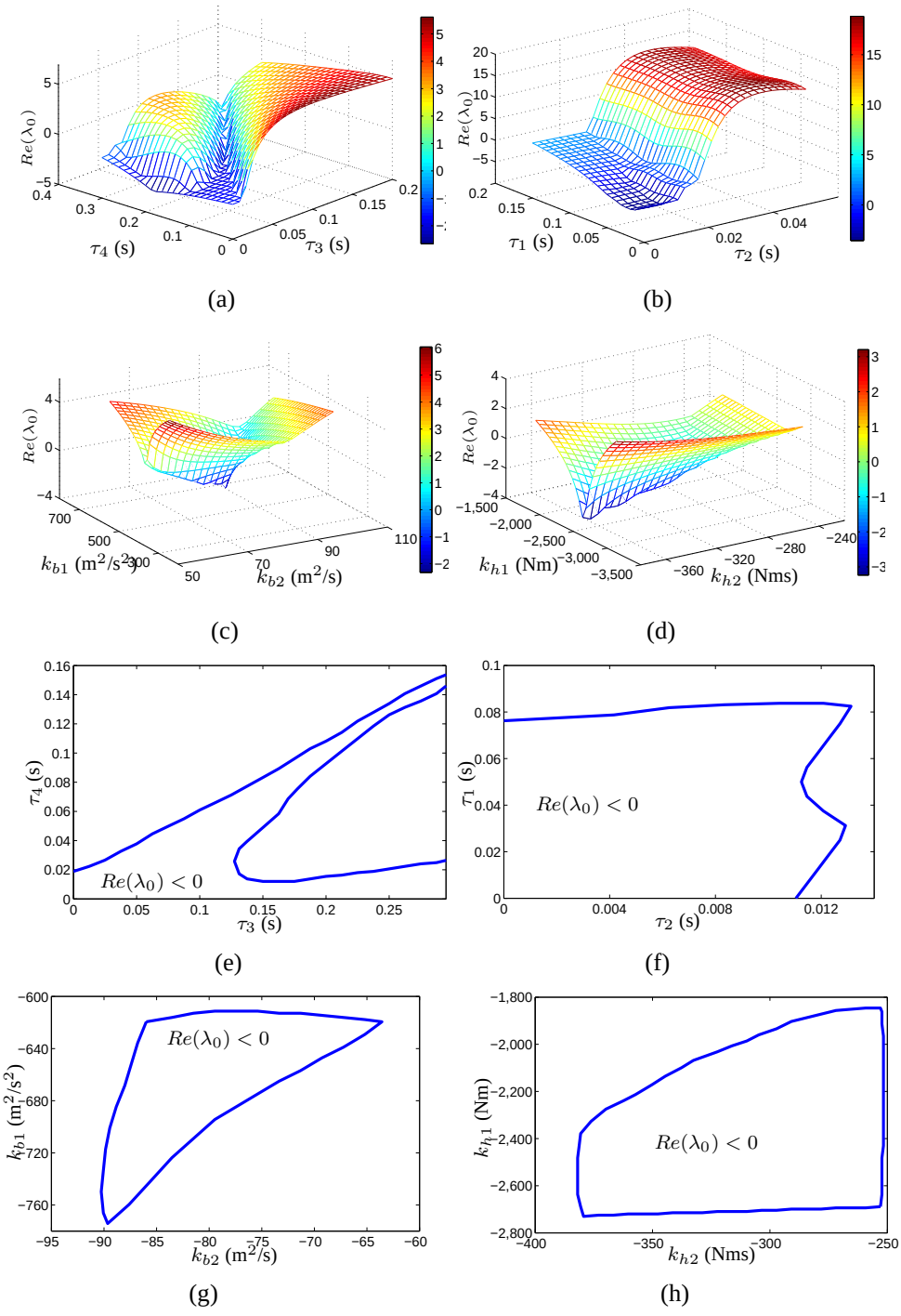

Figure 6.14: Stability regions under different model parameters in zero speed case. $Re(\lambda_0)$ values under varying (a) τ_3 and τ_4. (b) τ_1 and τ_2. (c) k_{b1} and k_{b2}. (d) k_{h1} and k_{h2}. In (e)-(h), stable regions are marked with $Re(\lambda_0) < 0$.

6.7 Conclusion

This chapter presented the human balance control and stability analysis of the rider-bicycle systems. We first presented a rider-bikebot dynamic model. Inspired by the experimental observation and the postural stance balance model, we proposed new PD feedback feedback models with time delays for the human upper-body movement and steering control for bicycle riding. The riding experiments with visual feedback and actuation disturbances were then conducted. We discussed the stability analysis of the rider-bicycle system and presented the influence of the model parameters, including the physical parameters, control gains and time delays, on the system stability. The results were also used to interpret the human balance capability and to compare with stance balance and balancing stationary bicycles that were reported previously. Additionally, the rider-bikebot system balancing stability in stationary case was also discussed.

Chapter 7

Balance Performance Tuning of Rider-Bikebot Interactions

7.1 Introduction

Human balance control plays a central role not only in human motor skills, such as standing or walking, but also in other human-machine or human-robot interactions. In recent years, bicycle was used as a diagnosis and treatment tool for clinic applications [63]. This motivates us to use the bicycle-based platform as a tool to study human-machine interactions. Human motor skill tuning or adaptation is another motivation for studying physical rider-bikebot interactions [66].

Rider motor skills analysis and bicycle self-balance control are two important tasks for designing balance tuning of rider-bikebot interactions. Bicycle dynamic models are extensively studied (e.g., [16]), and the rider-bicycle dynamic models and balance analysis are also reported in [12, 29, 30]. Several researchers focus on the quantitative modeling and analysis of riding motor skills. In [21], the rider balance control is modeled as the time delayed PD feedback for steering and upper-body leaning motion. The work in Chapter 6 extends these control models with sensory and actuation perturbation to analyze the influence of the models parameters on systems stability. The works in [22] and Chapter 5 propose a rider path-following control strategy using the EIC structure of the rider-bicycle dynamics [11]. From the EIC structure and BEM concepts, the balancing-tracking metrics are designed for the riding performances evaluation. Human behavioral models are also developed for both balance riding and path following behaviors [80, 81].

Tuning rider motor skills or controlling rider-bikebot interaction is a different process

comparing with the above-mentioned works. The actuations such as steering and pedaling are not controlled by only human rider or onboard computer but by their interactions. Few researches are reported about the interaction tuning and adaptation. Balance tuning of rider-bikebot interactions is also challenging for several reasons. First, the range of balanceable bicycle roll angle is limited and precise control is required for the unstable platform [57], particularly under low velocity or stationary [37]. Second, the torque control of the unstable rider-bikebot interactions is challenging due to their highly dynamic interactions and complex human multi-sensory, multiple time delay sensorimotor feedback [94]. Additional complication comes from adaptation of human motor control under external interference [95].

We present a balance performance tuning of rider-bikebot interactions. Unlike a typical bicycle, the bikebot front wheel is not rigidly connected to handlebar and is controlled by an onboard computer. Based on the rider handlebar steering, the onboard computer regulates the actual steering angle to achieve desired rider-bikebot interaction dynamics. To reach the design goal, we first convert the rider-bikebot dynamic model [21] into a new strict feedback form. In this form, the rider steering and upper-body leaning balancing effects become clear. A steering reshaping algorithm is designed for changing the control gains, stiffness and damping ratio coefficients. The rider-bikebot system is guaranteed to be balanced autonomously even without knowing rider steering information. Extensive human subject experiments are conducted under only human steering riding (as the benchmark), the interaction tuning riding and autonomous steering control. Rider control models and stability analysis techniques in [21, 22] are used to illustrate the motor skills changing and performance comparison. The main contribution of the work lies in the design and demonstration of the steering balance control of the rider-bikebot interactions. The outcome of this work enables the use of the bikebot control to change and train human motor skills through the human-robot interactions.

The remainder of the chapter is organized as follows. Section 7.2 presents the dynamic

model of rider-bikebot interactions. We discuss and analyze the control design and evaluation of the rider-bikebot interactions in Section 7.3. Experimental results are presented in Section 7.4. Concluding summary is presented in Section 7.5.

7.2 Rider-bikebot interactions model

As shown in Chapter 2. Defining $\boldsymbol{q} = [\varphi_b, \varphi_h]^T$, we obtain the rider-bikebot dynamics by the Lagrangian equations

$$\boldsymbol{M}(\boldsymbol{q})\ddot{\boldsymbol{q}} + \boldsymbol{C}(\boldsymbol{q}, \dot{\boldsymbol{q}}) + \boldsymbol{G}(\boldsymbol{q}) = \boldsymbol{u}, \tag{7.1}$$

where $\boldsymbol{u} = [0, \tau_h]^T$, τ_h is the rider leaning torque. We write the motion equation (7.1) into a different form. We introduce two state variables

$$q_r = \varphi_b + \gamma\left(\varphi_h\right),\ p_r = m_{11}(\varphi_h)\dot{\varphi}_b + m_{12}(\varphi_h)\dot{\varphi}_h, \tag{7.2}$$

where terms $m_{11}(\varphi_h)$ and $m_{12}(\varphi_h)$ are given as $m_{11}(\varphi_h) = m_b h_b^2 + m_h(h_s^2 + h_h^2 + 2h_s h_h \,\mathrm{c}_{\varphi_h}) + J_b + J_h$ and $m_{12}(\varphi_h) = m_h(h_h^2 + h_s h_h \,\mathrm{c}_{\varphi_h})$, respectively. State variable q_r is the combination of the cyclic coordinate φ_b and the shape coordinate φ_h, while p_r is the weighted angular momentum. In (7.2), variable $\gamma(\varphi_h)$ is given as

$$\gamma(\varphi_h) \;=\; \int_0^{\varphi_h} \frac{m_{12}(s)}{m_{11}(s)} ds. \tag{7.3}$$

Using the state variables, under the control inputs $\dot{\psi}$, $\ddot{\psi}$ and u_a, the dynamic model (7.1) is rewritten as

$$\dot{q}_r = m_{12}^{-1}(\varphi_h) p_r, \tag{7.4a}$$

$$\dot{p}_r = k_{p1}\dot{\psi} + k_{p2}\dot{\psi}^2 + k_d\ddot{\psi} + k_g g, \tag{7.4b}$$

$$\ddot{\varphi}_h = u_a, \tag{7.4c}$$

where the terms in (7.4b) are given as

$$
\begin{aligned}
k_d &= -m_b h_b l_b \,\mathrm{c}_{\varphi_b} - m_h h_s l_s \,\mathrm{c}_{\varphi_b} - m_h h_h l_h \,\mathrm{c}_{\varphi_b+\varphi_h}, \\
k_{p1} &= -(m_b h_b \,\mathrm{c}_{\varphi_b} + m_h h_s \,\mathrm{c}_{\varphi_b} + m_h h_h \,\mathrm{c}_{\varphi_b+\varphi_h}) v_r + (m_b l_b \,\mathrm{c}_{\varphi_b} + m_h l_s \,\mathrm{c}_{\varphi_b}) \tfrac{g l_t \,\mathrm{c}_\xi}{v_r}, \\
k_{p2} &= m_b h_b^2 \,\mathrm{s}_{\varphi_b} \,\mathrm{c}_{\varphi_b} + m_h h_h^2 \,\mathrm{s}_{\varphi_b+\varphi_h} \,\mathrm{c}_{\varphi_b+\varphi_h} + m_h h_s h_h \,\mathrm{c}_{2\varphi_b+\varphi_h}, \\
k_g &= m_b h_b \,\mathrm{s}_{\varphi_b} + m_h h_s \,\mathrm{s}_{\varphi_b} + m_h h_h \,\mathrm{s}_{\varphi_b+\varphi_h} .
\end{aligned}
$$

The relationship between the control inputs u_a and $\boldsymbol{u}$ in (7.1) is obtained as

$$
u_a = \boldsymbol{e}_2^T \boldsymbol{M}^{-1}(\boldsymbol{q}) \left[\boldsymbol{u} - \boldsymbol{C}(\boldsymbol{q}, \dot{\boldsymbol{q}}) - \boldsymbol{G}(\boldsymbol{q})\right]
$$

with $\boldsymbol{e}_2 = [0, 1]^T$.

The bikebot yaw rate and yaw acceleration are approximately calculated as [22]

$$
\dot{\psi} = \frac{v_r \tan\phi \,\mathrm{c}_\xi}{l \,\mathrm{c}_{\varphi_b}}, \;\; \ddot{\psi} \approx \frac{v_r \dot{\phi} \,\mathrm{c}_\xi}{l \,\mathrm{c}_\phi^2}. \tag{7.5}
$$

It is clear from (7.5) that the yaw rate and acceleration are directly related to the steering angle ϕ and angular rate $\dot{\phi}$, and those are considered as the inputs to (7.4). The rider control is considered as balancing a two-link acrobot system. The control inputs are not only the upper link (body) swing motion but also the steering motion. The introduction of the new states (q_r, p_r) puts the system into a strict feedback form (7.4). It becomes clear to see the direct influences by different control inputs, and the stability analysis is also conveniently obtained by this form. Based on the strict feedback form, the sub-dynamics of (q_r, p_r) is not directly influenced by the upper-body swing angular velocity $\dot{\varphi}_h$, angular acceleration $\ddot{\varphi}_h$ and the leaning torque τ_h.

7.3 Control of rider-bikebot interactions

7.3.1 Controller design

We consider the control design of the rider-bikebot interactions given by (7.4). The rider steering angle and actually controlled steering angle are denoted as $\phi_h(t)$ and $\phi(t)$, respectively. For given $\phi_h(t)$, the control goal is to design $\phi(t)$ to tune the interaction model from

$\phi_h(t)$ to (q_r, p_r). From (7.4b), the desired interaction model is

$$\dot{p}_r = k^a_{p1}\dot{\psi}_h + k^a_{p2}\dot{\psi}^2_h + k^a_d\ddot{\psi}_h + k^a_s p_r + k^a_g g^a, \tag{7.6}$$

where virtual yaw angle ψ_h, angular rate $\dot{\psi}_h$ and acceleration $\ddot{\psi}_h$ are calculated by (7.5) with ϕ_h. In order to obtain the same $\dot{p}_r$ profile in (7.4b) and (7.6), the controlled yaw rate $\dot{\psi}(t)$ must satisfy the following differential equation

$$\mathcal{C}: \ddot{\psi} + \frac{k_{p1}}{k_d}\dot{\psi} + \frac{k_{p2}}{k_d}\dot{\psi}^2 = \frac{k^a_{p1}}{k_d}\dot{\psi}_h + \frac{k^a_{p2}}{k_d}\dot{\psi}^2_h + \frac{k^a_d}{k_d}\ddot{\psi}_h + \frac{k^a_s}{k_d}p_r + \frac{k^a_g g^a - k_g g}{k_d}. \tag{7.7}$$

The above calculation is denoted as controller $\mathcal{C}$.

It is possible to show that the solution of (7.7) would generate a bounded steering angle $\phi(t)$ for a given bounded human rider roll angle $\phi_h(t)$. In (7.7), the term $k^a_s p_r$ adds damping-like effect to the interaction. The term k^a_{p1} can be considered as the control gain of the rider steering input. Control gain k^a_d is concerned with the steering velocity $\dot{\phi}_h(t)$. Term $k^a_g g^a$ acts similarly to the gravitational effect on balancing the platform.

When $\varphi_b(t)$ and $\varphi_h(t)$ are near zero, $\phi_h(t)$ is also small, and parameters k^a_{p1}, k^a_{p2} and k^a_d share the same functional forms as k_{p1}, k_{p2} and k_d. Controller $\mathcal{C}$ in (7.7) is linearized and has the relationship in Laplace domain as

$$\Omega_\psi(s) = \frac{k^{a*}_{p1} + k^{a*}_d s}{k^*_{p1} + k^*_d s}\Omega_{\psi_h}(s) + \frac{k^a_s p^*_r + k^{a*}_g g^a - k^*_g g}{k^*_{p1} + k^*_d s}, \tag{7.8}$$

where $\Omega_\psi(s) = \mathcal{L}(\dot{\psi})$ and $\Omega_{\psi_h}(s) = \mathcal{L}(\dot{\psi}_h)$ are the Laplace transformations of $\dot{\phi}$ and $\dot{\phi}_h$, respectively. The superscript "*" is used in (7.8) to indicate the linearized constants. It is clear from (7.8) that the steering output $\dot{\psi}(t)$ is a combination of the filtered $\dot{\psi}_h(t)$, roll angle and roll angular velocity.

In Chapter 6, the human rider steering control is modeled as a PD feedback structure with time delays. The tuning controller (7.8) shares the similar PD structure. Therefore, the interaction tuning can be viewed similarly to the human neuro-steering mechanism. Indeed, this observation is confirmed by the experimental results presented in Section 7.4.

We now consider a special case when control gains $k^a_{p1} = k^a_{p2} = k^a_d = 0$. In this case, the acutual steering angle is not a function of the rider steering input. The goal of the tuning

design is to maintain balancing under any feasible $\varphi_h(t)$. We denote this control design as autonomous steering $\mathcal{C}_a$.

Controller $\mathcal{C}_a$ can be considered as a special case by setting gains k^a_{p1}, k^a_{p2} and k^a_d to zero in (7.7). Therefore, we obtain

$$\Sigma^a:\ \dot{q}_r = m_{12}^{-1}(\varphi_h)p_r,\ \dot{p}_r = k^a_s p_r + k_g(q_r,\varphi_h)g^a, \tag{7.9}$$

where we choose constants $k^a_s < 0$, $g^a < 0$, and $k^a_g(q_r,\varphi_h) = k_q(q_r,\varphi_h)$. Defining state variable $\boldsymbol{x} = [q_r, p_r]^T$, we introduce the following property. Given (7.9) with the above parameters, $\boldsymbol{x}_{e0} = \mathbf{0} \in \mathbb{R}^2$ is an exponentially stable equilibrium for the system

$$\Sigma^a_0:\ \dot{q}_r = m_{12}^{-1}(0)p_r,\ \dot{p}_r = k^a_s p_r + k^a_g(q_r,0)g^a. \tag{7.10}$$

Note that Σ^a_0 in (7.10) is obtained from Σ^a in (7.9) under zero disturbance $\varphi_h(t) = 0$. The right-hand function of Σ^a_0 in (7.10) is continuously differentiable and its Jacobian matrix is

$$\boldsymbol{A} = \begin{bmatrix} 0 & m_{12}^{-1}(0) \\ \frac{\partial g^a k^a_g(q_r,0)}{\partial q_r} & k^a_s \end{bmatrix}_{q_r=0},$$

which is bounded and Lipschitz for $q_r \in (-\pi/2, \pi/2)$. Therefore, the origin is an exponentially stable equilibrium of the linearized system $\dot{\boldsymbol{x}} = \boldsymbol{A}\boldsymbol{x}$. By the linearization stability theorem [58], nonlinear system Σ^a_0 has the exponentially stable equilibrium $\boldsymbol{x}_{e0} = \mathbf{0}$.

From the above property and converse Lyapunov function theorem, we obtain the following input-state stability relationship: for Σ^a_0, there exist a disturbance bound $\|\varphi_h(t)\|_\infty$ and an initial bound $\|\boldsymbol{x}(0)\|_\infty$ to guarantee that $\Sigma^a_0 \in \mathcal{L}_\infty$, namely,

$$\|\boldsymbol{x}(t)\|_\infty \le \gamma_b \|\varphi_h(t)\|_\infty + \beta_b \tag{7.11}$$

for non-negative constants $\gamma_b \ge 0$ and $\beta_b \ge 0$.

From the definition of $\gamma(\varphi_h)$ and q_r in (7.3) and (7.2), the bounded $\varphi_h(t)$ and $q_r(t)$ result in a bounded $\varphi_b(t)$. The above analysis implies that if the rider roll angle $\varphi_h(t)$ is bounded and relatively small, the rider-bikebot interactions can be stabilized by autonomous steering $\mathcal{C}_a$. Note that controller $\mathcal{C}_a$ has an attractive property with few parameters and does not need the measurement of rider upper-body leaning torque.

7.3.2 Performance metrics and evaluation

Tuning interaction model affects the rider behavior, balancing performance and systems stability, and we ought to analyze these effects.

The rider steering $\phi_h(t)$ and upper-body $\tau_h(t)$ control models in Chapter 6 are introduced as

$$\tau_h(t) = k_{h0}\varphi_h(t) + k_{h1}\varphi_b(t-\tau_1) + k_{h2}\dot{\varphi}_b(t-\tau_2) + k_{h3}\varphi_h(t-\tau_1) + k_{h4}\dot{\varphi}_h(t-\tau_2) \quad (7.12)$$

and

$$\phi_h(t) = \frac{1}{v_r^2}[k_{b1}\varphi_b(t-\tau_3) + k_{b2}\dot{\varphi}_b(t-\tau_4) + k_{b3}\varphi_h(t-\tau_3) + k_{b4}\dot{\varphi}_h(t-\tau_4)], \quad (7.13)$$

where constants k_{hi}, $i = 0, \cdots, 4$, and k_{bj}, $j = 1, \cdots, 4$, are the control gains. $\tau_i > 0$, $i = 1, \cdots, 4$, are the constant time delays of human sensorimotor system. For convenience of stability analysis, we assume that the actual steering input $\phi(t)$ shares the same structure as $\phi_h(t)$ but with additional delay $\tau_s > 0$, namely,

$$\phi_h(t) = \frac{1}{v_r^2}[k_{t1}\varphi_b(t-\tau_3-\tau_s) + k_{t2}\dot{\varphi}_b(t-\tau_4-\tau_s) + k_{t3}\varphi_h(t-\tau_3-\tau_s) + k_{t4}\dot{\varphi}_h(t-\tau_4-\tau_s)], \quad (7.14)$$

where control gains k_{tl}, $l = 1, \cdots, 4$, are constants. Note that under human control, gains $k_{tl} = k_{bj}$, $l, j = 1, \cdots, 4$ and difference between $\phi(t)$ and $\phi_h(t)$ is the additional time delay τ_s of the steering mechanism. As shown in Chapter 6, with control models $\phi(t)$ and $\tau_h(t)$, the real part of right most roots of the closed-loop characteristic equation, denoted as $Re(\lambda_0)$, is used as an index for the system stability. To quantify the balance performance, the average absolute balancing torque, denoted as B_1^M, is introduced as a metric index [22]. The second metric B_2^M is the average gravity torque in the riding time interval $[t_1, t_2]$, that is,

$$B_2^M = \frac{1}{t_2 - t_1}\int_{t_1}^{t_2} |k_g(\varphi_b, \varphi_h)\, g| dt. \quad (7.15)$$

7.4 Experimental results

7.4.1 Experiment setup

The bikebot system is shown in Fig. 2.1(a). The bikebot roll angle φ_b and upper-body leaning φ_h are measured by the onboard IMU and a rolling arm, respectively. The bicycle velocity v_r, front wheel steering ϕ and handlebar steering ϕ_h are measured by the encoders. An onboard computer is connected to sensors and actuation systems. The system details are included in Chapter 2. The linkage between the bikebot handlebar and the front steering frame can be reconfigured and disconnected. The handlebar steering $\phi_h(t)$ is controlled by the rider. The front wheel steering $\phi(t)$ is controlled by the onboard computer and driven by the steering motor.

Three subjects were recruited for the bikebot riding and tuning experiments. All of the participants were reported to be in a good health condition and they were considered as experienced riders (i.e., at least five-year bicycle riding history). Three sets of riding experiments were conducted in this study. The first set of experiments was the normal bikebot (bicycle) riding. The subjects ride the bikebot as a regular bicycle and steering angle $\phi(t) = \phi_h(t)$. In the second and third sets of experiments, the handlebar was not rigidly connected to the front wheel frame and the steering angle was regulated by the onboard controllers $\mathcal{C}$ and $\mathcal{C}_a$ as described in the previous section.

The subjects were asked to ride the bikebot for only keeping balance (about 10-12 s) at an open parking lot. Disturbed torques were generated by the gyro-balancer to perturb the riding for about two to four times (each time lasts for about 0.5 s with a peak torque around 35 Nm) in each run. The subjects were not informed when the perturbation torques were applied so that the collected data can be used to identify the natural human responses. In each set of experiments, the subjects were requested to repeat the riding for three times. Before the formal experiments, each subject was asked to ride the bikebot for 10 to 15 mins to get familiar with the platform. The subjects were asked to control the bikebot at a fixed velocity around $v_r = 1.8$-2.2 m/s.

7.4.2 Experimental results

The values of the control parameters of three sets of controllers are listed in Table 7.1. The human riding is considered as the benchmark for the other two controllers. For controllers $\mathcal{C}$ and $\mathcal{C}_a$, from several tests, the damping and the stiffness coefficients are chosen respectively as $k_s^a = -1.2, g^a = 0.5g$ and $k_s^a = -2.5, g^a = -0.5g$, $g = 9.8\ \mathrm{m/s^2}$ is the gravitational constant.

Table 7.1: Parameters configuration of interaction model

Parameters	k_{p1}^a/k_{p1}	k_{p2}^a/k_{p2}	k_d^a/k_d	k_s^a	g^a/g	k_g^a
Human	1.0	1.0	1.0	0.0	1.0	k_g
$\mathcal{C}$	1.0	1.0	1.0	-1.2	0.5	k_g
$\mathcal{C}_a$	0.0	0.0	0.0	-2.5	-0.5	k_g

Fig. 7.1 shows the comparison results of various performance under rider normal riding, controllers $\mathcal{C}$ and $\mathcal{C}_a$ from one subject. For the benchmark results shown in Fig. 7.1(d), the gyro-balancer generates disturbance peak torques at two time instances. Right after the disturbance torques, φ_b and φ_h profiles show clear reactive responses. Looking into ϕ and τ_h profiles shown in Fig. 7.1(a), the rider does not seemingly show the consistent responses. For the first disturbance, the rider seems to response with a large steering angle ϕ but for the second one, it is not obvious to see a large steering angle profile change. One reason for such results comes from that for the second disturbance, steering angle ϕ is in a negative value range, which already provides correction response to the disturbance. We also observe a large leaning torque τ_h profile at the time of these disturbances.

Under controller $\mathcal{C}$, Figs. 7.1(b) and 7.1(e) show the experimental performance from the same subject. Under the same disturbance torques as those in normal riding experiments, the human responses, both the steering angle ϕ_h and leaning torques τ_h, show different responses; see Fig. 7.1(b). Rider responses show oscillating profiles of ϕ_h and τ_h, while both the bikebot and human roll angles show more oscillation but less significant (in magnitude)

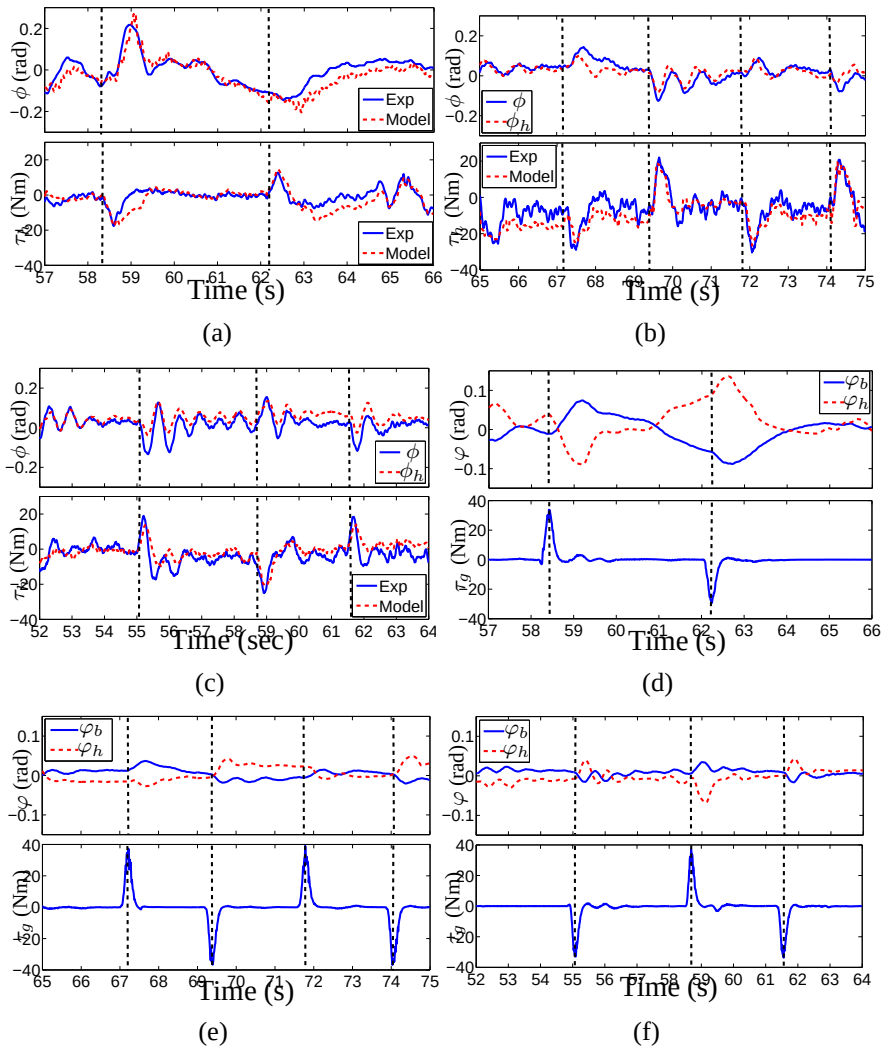

Figure 7.1: Comparison of experimental results under three controllers for one subject. The first column is under normal riding control, the second and the third column plots are under $\mathcal{C}$ and $\mathcal{C}_a$, respectively. In (a)-(c), the top plots are the handlebar steering angle ϕ_h and actual steering angle ϕ. The bottom plots are the human upper-body torque τ_h. In (d)-(f), the top plots are the bikebot roll angle φ_b and rider upper-body roll angle φ_h. The bottom plots are the applied disturbance torque τ_g.

than these in normal riding; see Fig. 7.1(d). Comparing with $\mathcal{C}$, controller $\mathcal{C}_a$ generates even more extremely responses as illustrated in Figs. 7.1(c) and 7.1(f). For example, both φ_b and φ_h profiles occur fast and small magnitude oscillations; see Fig. 7.1(e). It is not surprising to notice that steering angles ϕ and ϕ_h also show the faster oscillations than these under $\mathcal{C}$.

It is interesting to observe that under $\mathcal{C}$ and $\mathcal{C}_a$, the actual steering angle (ϕ) profile shares a similar trend as the rider steering angle profile ϕ_h. This observation can also be

confirmed by the models in (7.13) and (7.14) and the comparison results of the model prediction and actual profiles in Figs. 7.1(b) and 7.1(c). The input differences of $\mathcal{C}$ and $\mathcal{C}_a$ lie in their magnitudes. One of the main reasons for such results is that the calculated steering angle ϕ by controller (7.7) is highly related to the human steering input and this observation is also validated by the approximation given in (7.8). Even for $\mathcal{C}_a$, the influence of human steering control still exists because of the damping-effect feedback term $k_s^a p_r$.

To evaluate the control performance, Fig. 7.2(a) shows the values of the mean and standard derivations of metrics B_1^M and B_2^M for three subjects under various runs. It is clear that under $\mathcal{C}$, the mean value of B_1^M is smallest among three controllers. If we consider metric B_2^M, controller $\mathcal{C}_a$ demonstrates the smallest value. However, from Figs. 7.1(d)-7.1(f), under $\mathcal{C}_a$, the rolling angles $\varphi_b(t)$ and $\varphi_h(t)$ change fastest, that is, the fast response needs large torques and results in large B_1^M. As listed in Table 7.2, the F-test results show that both the B_1^M and B_2^M values under $\mathcal{C}$ are significantly different from the human riding. The difference of B_2^M under $\mathcal{C}$ and $\mathcal{C}_a$ is statistically significant. These results imply that the proposed control designs enhance the closed-loop balance performance significantly.

Table 7.2: F-test for the balancing metrics under controllers $\mathcal{C}$ and $\mathcal{C}_a$ ($F_{0.05(1,4)} = 7.71$)

Subject	A	B	C
B_1^M under $\mathcal{C}$	10.73	14.46	25.78
B_1^M under $\mathcal{C}_a$	3.01	0.31	0.01
B_2^M under $\mathcal{C}$	20.91	8.07	10.57
B_2^M under $\mathcal{C}_a$	36.45	25.57	19.97

Using the experimental data, we also identify and estimate the steering and human upper-body leaning torque models given by (7.12) and (7.13) and controller $\mathcal{C}$ by (7.14). As demonstrated in Figs. 7.1(a)-7.1(c) for one subject, these identified models fit the experimental data closely and therefore, the PD structure with time delays captures the actual human motor skills. We also look into the changes of the parameters values for controllers

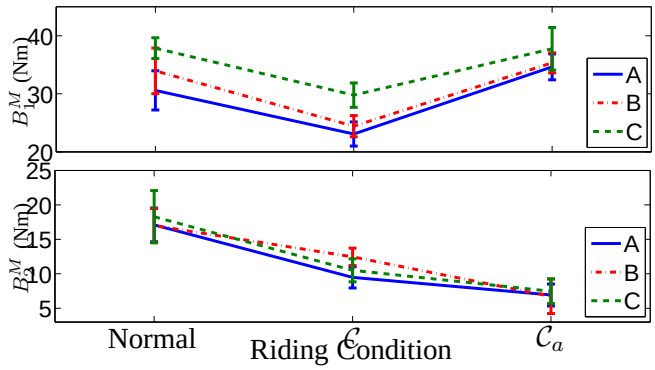

(a)

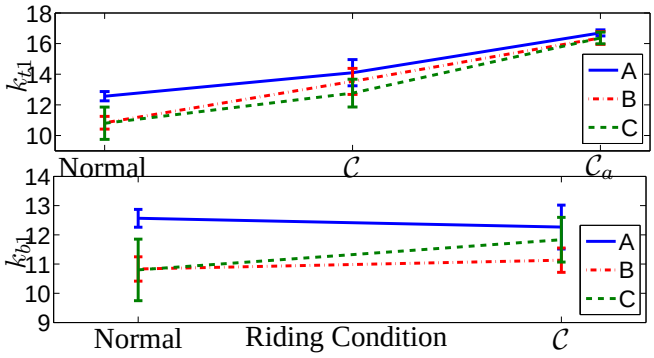

(b)

Figure 7.2: Mean values and standard variance across all subjects with respect to experiments conditions: (a). Balancing metric BM_1 and BM_2. (b). Control gains k_{t1} and k_{b1}.

$\mathcal{C}$ and $\mathcal{C}_a$. For each subject, the model parameters values of the leaning torque $\tau_h(t)$, including control gains and time delays, do not show significant change under $\mathcal{C}$ or $\mathcal{C}_a$. This implies that, even with the changing rider-bikebot interactions, the riders' leaning balance mechanism has no significant change. For steering control $\phi(t)$ and $\phi_h(t)$, the control model gains vary as shown in Fig. 7.2(b) with estimated time delay $\tau_s = 8$-10 ms. The values of the most influential control gains k_{t1} and k_{b1} are changed under controller $\mathcal{C}$. With the increasing rider-bikebot interaction stiffness coefficient, the steering control gain k_{t1} grows as well and under $\mathcal{C}_a$, it has the largest value. On the other hand, the values of the human steering control gain k_{b1} do not change much between human riding and under $\mathcal{C}$.

Finally, we consider the stability index $Re(\lambda_0)$ changes under different control gains. Fig. 7.3 shows the values of $Re(\lambda_0)$ with gains k_{t1} and k_{t2}. From this figure, under a typical derivative control gain $k_{t2} \in [1.0, 3.0]$, the values of $Re(\lambda_0)$ reduce with the increasing

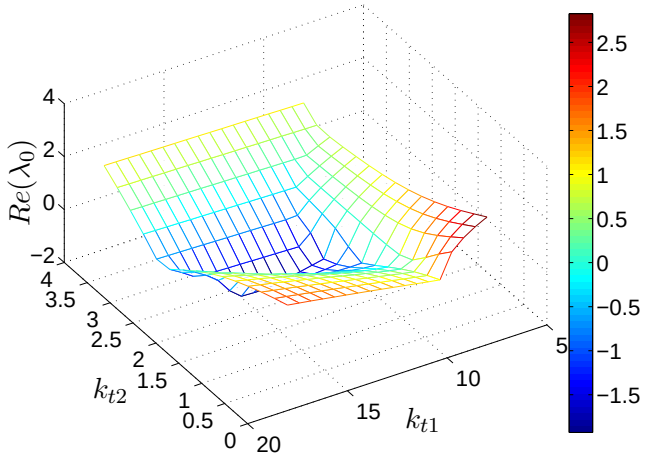

Figure 7.3: Values of $Re(\lambda_0)$ with different gains k_{t1} and k_{t2} under controllers $\mathcal{C}$.

value of k_{t1}. Combining the results in Fig. 7.2(b), if the value of the stiffness coefficient is reduced, say k_{t1}, from 10 to 16.5, the values of $Re(\lambda_0)$ reduce as well. This implies enhanced stability performance, and the result is consistent with the balance performance in experiments.

7.5 Conclusion

This chapter presented the tuning control of rider-bikebot interactions to enhance the balance performance. The design was built on the strict feedback form of the rider-bikebot interactions model. The control of the rider-bikebot interactions was designed to tune the model stiffness and damping effects. We presented two types of tuning control design. One design used the rider steering information and balancing states, and second one used only balancing states. We conducted extensive multi-subject experiments to demonstrate the control performance. Performance comparisons were also presented among the human normal riding and the proposed rider-bikebot interactions controllers. It has been demonstrated that the balance performance and the stability of the controlled rider-bikebot interactions were significantly improved than that with only human control.

Chapter 8
Conclusions and Future Work

8.1 Conclusions

This dissertation contains three different works: control system design for the autonomous bikebot system, human riding motor skills and mechanism analysis for balancing and path tracking, and the tuning control of rider-bikebot interactions. Additionally, rider-bicycle systems dynamics and bikebot experimental system are also included.

The balancing control problems for the autonomous bikebot systems were solved. For the stationary balancing task, a gyro-balancer pivoting control law was designed. The balancing torque generated by the flywheel pivoting motion was used to both balance a stationary bicycle and drive the system onto periodical orbits. The desired periodical orbits of bicycle rolling motion and flywheel pivoting were achieved via energy shaping and the introduction of virtual constraints. For this under-actuated system, a Lyapunov-based nonlinear control law was designed to regulate both the bikebot rolling and flywheel pivoting motion onto their desired orbits. For the task of balancing during motion, a steering balancing control law design was introduced using the feedback linearization. The control capabilities of these two control laws were analyzed. Considering the closed-loop dynamics with parameters and the actuators' motion limitations, DOAs of these two control laws were estimated. Furthermore, the largest DOAs were also estimated and these DOAs depended on only the motion limitation, but not on the control law structures. Based on these control capabilities analyses, a switching control strategy was proposed for the transition from stationary balancing to balancing during motion. Experimental results demonstrated the performances of the aforementioned control methods.

The position tracking tasks were implemented by several EIC-based controllers. An EIC-based bikebot position trajectory tracking controller was introduced, and a gyro-balancer auxiliary control law was proposed. The gyro-balancer was used for generating the auxiliary balancing torque for the equilibrium roll angle trajectory tracking. In the control process, this gyro-balancer motion could partly replace the role of steering for balancing. In the theoretical analysis, for this under-actuated system output tracking problem, the gyro-balancer and steering combination control could reduce the position tracking errors. The path following performance of the regular EIC-based control law was tested experimentally. Five types of paths were followed by the bikebot system. The moving point tracking function was implemented by the regular EIC-based control and the enhanced EIC-based control with integrated velocity vector field design. By the performance comparison, the latter control strategy was determined to have superior position tracking result than the former one. Finally, the gyro-balancer auxiliary control law was implemented for the path-following task. Comparing with the typical EIC-based control, the performance under the gyro-balancer assistant was enhanced.

For the rider-bikebot system, rider position tracking and balancing control were modeled, analyzed and discussed. In the position tracking analysis, the BEM concept was introduced to capture the rider balance motor skills in interactions with the bicycle. The BEM was built on the rider-bicycle dynamics that satisfied the nearly EIC structure. Using the dual convertible property of the EIC system, a feedback linearization controller was designed and its stability was proven. Two BEM-based performance metrics were also proposed and used to capture the balance and path-following skills. Extensive experiments were conducted with several riders riding the bikebot to follow different paths at different velocities. Based on the collected rider-bikebot system states, the proposed rider control structure output was compared with the actual rider operations. The recorded rider control processes also illustrated the proposed BEM concept and were used to compare the balance performance between the rider control and the bikebot autonomous control.

For the rider balancing control, inspired by other human balancing models, a new PD

feedback feedback structure with time delays for the upper-body movement and steering control models was proposed for depicting the rider balancing maneuvers. Several kinds of experiments with riders were conducted. Besides the normal riding conditions, visual feedback disturbances, external torque disturbance and steering operation time delays were injected into the system to vary the rider motor skills. The proposed control models were verified by the experiments. Changes to the control parameters under different disturbances were observed. A time-delayed linear system stability calculation tool was introduced for the closed-loop stability analysis. According to this theoretical stability analysis and experimental observations, the influence of the physical and control models parameters on stability and balancing performances were presented and discussed.

For the final problem of actively tuning the rider-bikebot interactions, the interaction model was rewritten in strict feedback form. For the steering to rolling motion relationship, the stiffness and damping effect were analyzed. The control of the rider-bikebot interactions was designed to tune the stiffness and damping effects by reshaping the rider handlebar steering angle. Several rider were asked to ride the bikebot under different changed interaction models. Performance comparisons were also presented for the human normal riding and the proposed rider-bikebot interactions controllers. It had been demonstrated that the balance performance and the stability of the controlled rider-bikebot interactions were significantly improved than those with only human control. Furthermore, based on theoretical analysis, under special tuned stiffness and damping effect conditions, the rider-bicycle system could be balanced autonomously without rider control. This property was also verified experimentally.

The dynamics models of the autonomous bikebot system and rider-bikebot system play a central role for the aforementioned analysis and design. These dynamics models were constructed and verified experimentally. For implementing all these mentioned experiments, the bikebot system mechanics, hardware and software were constructed and modified throughout the whole research process.

8.2 Future work

Although the autonomous control system design, the rider riding mechanism analysis and the interaction dynamics tuning for the rider-bikebot system are discussed systematically in this dissertation, a lot of open problems still exist to solve and a lot of functions still have to implement in the future.

Enhancing the autonomous balancing capability of the bikebot in the stationary and low-velocity regions is still an open problem. Due to the gyro-balancer limited balancing torque, it is necessary to design the combination control law to use the gyro-balancer and steering motion for balancing at same time. As a fundamental work, the front wheel and rear wheel contact points motion mechanism under low velocity and different steering motion have to be modeled precisely. In the tracking task, the tracking performance still has room for improvement. As an non-minimum phase under-actuated system, the output tracking laws can be modified and implemented. In the tracking process, the gyro-balancer auxiliary capability can be enlarged by other control laws. Also, the dynamics under the large rolling angle and steering angle condition has to be modeled precisely for the agile motion control.

In terms of the human rider control mechanism analysis, the rider tracking behavior and control principle can be analyzed in depth. The upper-body motion function in the bicycle/motorcycle riding maneuver can be discussed quantitatively. The balancing control models also can be modified and extended to depict the rider path-following operation.

For the active interaction control and tuning, the author considers this dissertation serves as a cornerstone to further explore more topics. The current rider-bikebot interaction tuning methods are preliminary. Many control strategies and training methodologies still remain to be developed or implemented for rider training or assistance. The proposed method changes the stability and balancing states speed of convergency of the interaction model. With the tuned interaction model, the rider motor skills and control behaviors are also changed passively. How to tune the rider operation effectively and actively is still an

open and challenging question.

References

[1] J. Yi, D. Soudbakhsh, Y. Zhang, and Y. Zhang, “Why some Parkinson’s disease patients cannot stand or walk but can ride a bicycle – A control system-based analysis,” in *Proc. ASME Dyn. Syst. Control Conf.*, Ft. Lauderdale, FL, 2012, Paper # DSCC2012-8735.

[2] J. Meijaard and J. Papadopoulos and A. Ruina and A. Schwab, “Linearized dynamics equations for the balance and steer of a bicycle: A benchmark and review,” *Proc. Royal Soc. A*, vol. 463, pp. 1955–1982, 2007.

[3] J. Yi, Y. Zhang, and D. Song, “Autonomous motorcycles for agile maneuvers: Part I: Dynamic modeling,” in *Proc. IEEE Conf. Decision Control*, Shanghai, China, 2009, pp. 4613–4618.

[4] M. Defoort and T. Murakami, “Sliding-mode control scheme for an intelligent bicycle,” *IEEE Trans. Ind. Electron.*, vol. 56, no. 9, pp. 3357–3368, 2009.

[5] R. Sharp, “The stability and control of motorcycles,” *J. Mech. Eng. Sci.*, vol. 13, no. 5, pp. 316–329, 1971.

[6] ——, “Stability, control and steering responses of motorcycles,” *Veh. Syst. Dyn.*, vol. 35, no. 4-5, pp. 291–318, 2001.

[7] V. Cossalter and R. Lot, “A motorcycle multi-body model for real time simulations based on the natural coordinates approach,” *Veh. Syst. Dyn.*, vol. 37, no. 6, pp. 423–447, 2002.

[8] V. Cossalter, A. Doria, R. Lot, N. Ruffo, and M. Salvador, “Dynamic properties of motorcycle and scooter tires: Measurement and comparison,” *Veh. Syst. Dyn.*, vol. 39, no. 5, pp. 329–352, 2003.

[9] V. Cossalter and A. Doria, “The relation between contact patch geometry and the mechanical properties of motorcycle tyres,” *Veh. Syst. Dyn.*, vol. 43, no. Suppl., pp. 156–167, 2005.

[10] J. Grizzle, M. Di Benedetto, and F. Lamnabhi-Lagarrigue, “Necessary conditions for asymptotic tracking in nonlinear systems,” *IEEE Trans. Automat. Contr.*, vol. 39, no. 9, pp. 1782–1794, 1994.

[11] N. Getz, “Dynamic inversion of nonlinear maps with applications to nonlinear control and robotics,” Ph.D. dissertation, Dept. Electr. Eng. and Comp. Sci., Univ. Calif., Berkeley, CA, 1995.

[12] Y. Zhang, "Modeling and control of single track vehicles: A human/machine/environment interactions perspective," Ph.D. dissertation, Dept. Mech. Aero. Eng., Rutgers Univ., Piscataway, NJ, 2014.

[13] A. Levandowski, A. Schultz, C. Smart, A. Krasnov, H. Chau, B. Majusiak, F. Wang, D. Song, J. Yi, H. Lee, and A. Parish, "Ghostrider: Autonomous motorcycle," in *Proc. IEEE Int. Conf. Robot. Autom. (Video)*, Orlando, FL, 2006.

[14] P. Wang, J. Yi, T. Liu, and Y. Zhang, "Trajectory tracking and Balancing Control of an Autonomous Bike," in *Proc. IEEE Int. Conf. Robot. Autom.*, Singapore, 2017, pp. 2414–2419.

[15] http://www.honda.com/mobility/riding-assist.

[16] K. Åström, R. Klein, and A. Lennartsson, "Bicycle dynamics and control," *IEEE Control Syst. Mag.*, vol. 25, no. 4, pp. 26–47, 2005.

[17] A. Beznos, A. Formal'sky, E. Gurfinkel, D. Jicharev, A. Lensky, K. Savitsky, and L. Tchesalin, "Control of autonomous motion of two-wheel bicycle with gyroscopic stabilisation," in *Proc. IEEE Int. Conf. Robot. Autom.*, Leuven, Belgium, 1998, pp. 2670–2675.

[18] B. T. Thanh and M. Parnichkun, "Balancing control of bicyrobo by particle swarm optimization-based structure-specified mixed H_2/H_∞ control," *Int. J. Adv. Robotic Syst.*, vol. 5, no. 4, pp. 395 – 402, 2008.

[19] S. C. Spry and A. R. Girard, "Gyroscopic stabilization of unstable vehicles: Configurations, dynamics, and control," *Veh. Syst. Dyn.*, vol. 46, no. Supp., pp. 247–260, 2008.

[20] Y. Zhang, P. Wang, J. Yi, D. Song, and T. Liu, "Stationary balance control of a bikebot," in *Proc. IEEE Int. Conf. Robot. Autom.*, Hong Kong, China, 2014, pp. 6706–6711.

[21] P. Wang and J. Yi, "Dynamic stability of a rider-bicycle system: Analysis and experiments," in *Proc. Amer. Control Conf.*, Chicago, IL, 2015, pp. 1161–1166.

[22] ——, "Balance equilibrium manifold and control of rider-bikebot systems," in *Proc. Amer. Control Conf.*, Boston, MA, 2016, pp. 2168–2174.

[23] K. Chen, Y. Zhang, and J. Yi, "An integrated physical-learning model of physical human-robot interactions: A bikebot riding example," in *Proc. ASME Dyn. Syst. Control Conf.*, San Antonio, TX, 2014, Paper DSCC2014-6007.

[24] H. Han, Y. Liu, T. Liu, Y. Inoue, and K. Shibata, "A novel velocity sensor based on electromagnetic induction," in *Proc. IEEE Sensors Conf.*, Limerick, Ireland, 2011, pp. 1701–1704.

[25] A. M. Sabatini, C. Martelloni, S. Scapellato, and F. Cavallo, “Assessment of walking features from foot inertial sensing,” *IEEE Trans. Biomed. Eng.*, vol. 52, no. 3, pp. 486–494, 2005.

[26] Y. Zhang, K. Chen, and J. Yi, “Rider trunk and bicycle pose estimation with fusion of force/inertial sensors,” *IEEE Trans. Biomed. Eng.*, vol. 60, no. 9, pp. 2541–2551, 2013.

[27] X. Lu, K. Yu, Y. Zhang, J. Yi, and J. Liu, “Whole-body pose estimation in physical rider-bicycle interactions with a monocular camera and wearable gyroscopes,” in *Proc. IEEE/RSJ Int. Conf. Intell. Robot. Syst.*, Chicago, IL, 2014, pp. 4124–4129.

[28] A. D. Goodworth and R. J. Peterka, “Influence of bilateral vestibular loss on spinal stabilization in humans,” *J. Neurophysiol.*, vol. 103, pp. 1978–1987, 2010.

[29] J. K. Moore, “Human control of a bicycle,” Ph.D. dissertation, Dept. Mech. Aero. Eng., Univ. Calif. Davis, Davis, CA, 2012.

[30] S. M. Cain, “An experimental investigation of human/bicycle dynamics and rider skill in children and adults,” Ph.D. dissertation, Dept. Biomed. Eng., Univ. Michigan, Ann Arbor, MI, 2013.

[31] D. Soudbakhsh, Y. Zhang, and J. Yi, “Stability analysis of human balance control of stationary bicycles,” in *Proc. Amer. Control Conf.*, Montreal, Canada, 2012, pp. 2755–2760.

[32] I. Havoutis and S. Ramamoorthy, “Motion planning and reactive control on learnt skill manifolds,” *Int. J. Robot. Res.*, vol. 32, no. 9-10, pp. 1120–1150, 2013.

[33] T. Feix, J. Romero, C. H. Ek, H.-B. Schmiedmayer, and D. Kragic, “A metric for comparing the anthropomorphic motion capability of artificial hands,” *IEEE Trans. Robotics*, vol. 29, no. 1, pp. 82–93, 2013.

[34] J. Romero, T. Feix, C. H. Ek, H. Kjellström, and D. Kragic, “Extracting postural synergies for robotic grasping,” *IEEE Trans. Robotics*, vol. 29, no. 6, pp. 1342–1352, 2013.

[35] S. Mousavi, X. Zhang, T. Seigler, and J. Hoagg, “Characteristics that Make Dynamic Systems Difficult for a Human to Conrol,” in *Proc. Amer. Control Conf.*, Boston, MA, 2016, pp. 4391–4396.

[36] J. D. G. Kooijman, J. Merjaard, J. M. Papadopoulos, A. Ruina, and A. Schwab, “A bicycle can be self-stable without gyroscopic or caster effects,” *Science*, vol. 332, pp. 339–342, 2011.

[37] Y. Zhang, J. Li, J. Yi, and D. Song, “Balance control and analysis of stationary riderless motorcycles,” in *Proc. IEEE Int. Conf. Robot. Autom.*, Shanghai, China, 2011, pp. 3018–3023.

[38] C.-G. Song, J.-Y. Kim, and N.-G. Kim, “A new postural balance control system for rehabilitation training based on virtual cycling,” *IEEE Trans. Inform. Technol. Biomed.*, vol. 8, no. 2, pp. 200–207, 2004.

[39] A. H. Snijders and B. R. Bloem, “Cycling for freezing of gait,” *New Engl. J. Med.*, vol. 362, p. e46, 2010.

[40] A. H. Snijders, I. Toni, E. Růžička, and B. R. Bloem, “Bicycling breaks the ice for freezers of gait,” *Mov. Disord.*, vol. 26, no. 3, pp. 367–371, 2011.

[41] J. Yi, D. Song, A. Levandowski, and S. Jayasuriya, “Trajectory tracking and balance stabilization control of autonomous motorcycles,” in *Proc. IEEE Int. Conf. Robot. Autom.*, Orlando, FL, 2006, pp. 2583–2589.

[42] Y. Tanaka and T. Murakami, “A study on straight-line tracking and posture control in electric bicycle,” *IEEE Trans. Ind. Electron.*, vol. 56, no. 1, pp. 159–168, 2009.

[43] J. Yi, Y. Zhang, and D. Song, “Autonomous motorcycles for agile maneuvers: Part II: Control systems design,” in *Proc. IEEE Conf. Decision Control*, Shanghai, China, 2009, pp. 4619–4624.

[44] A. Levandowski, A. Schultz, C. Smart, A. Krasnov, D. Song, H. Lee, H. Chau, B. Majusiak, and F. Wang, “Autonomous motorcycle platform and navigation – Blue Team,” DARPA Grand Challenge 2005, Tech. Rep., 2005, Also http://www.ghostriderrobot.com/.

[45] C. Yang and T. Murakami, “Full-speed range self-balancing electric motorcycles without the handlebar,” *IEEE Trans. Ind. Electron.*, vol. 63, no. 3, pp. 1911–1922, 2016.

[46] I. Fantoni and R. Lozano and M. W. Spong, “Energy based control of pendubot,” *IEEE Trans. Automat. Contr.*, vol. 45, no. 4, pp. 725–729, 2000.

[47] S. Nair and N. E. Leonard, “A normal form for energy shaping: application to the furuta pendulum,” in *Proc. IEEE Conf. Decision Control*, Las Vegas, NV.

[48] A. Bloch, N. E. Leonard and J. E. Marsden, “Controlled Lagrangians and the stailization of mechanical system I: the first matching theorem,” *IEEE Trans. Automat. Contr.*, vol. 45, no. 12, pp. 2253 – 2270, 2000.

[49] ——, “Controlled Lagrangians and the stailization of mechanical system II: potential shaping,” *IEEE Trans. Automat. Contr.*, vol. 46, no. 10, pp. 1556 – 1571, 2001.

[50] R. Orgeta, M. W. Spong, F. Gomez-Estern, and G. Blankenstein, “Stailization of a class of underactuated mechanical system via interconnection and damping assignment,” *IEEE Trans. Automat. Contr.*, vol. 47, no. 8, pp. 1218 – 1233, 2002.

[51] ——, “Interconnection and damping assignment passivity-based control of mechanical system with underactuation degree one,” *IEEE Trans. Automat. Contr.*, vol. 50, no. 12, pp. 1936 – 1955, 2005.

[52] A. S. Shiriaev, L. B. Freidovich, and I. R. Manchester, "Can we make a robot ballerina perform a pirouette? Orbital stabilization of periodic motions of underactuated mechanical systems," *Ann. Rev. Contr.*, vol. 32, pp. 200–211, 2008.

[53] A. S. Shiriaev, J. W. Perram, and C. Canudas-de-Wit, "Constructive tool for orbital stabilization of underactuated nonlinear systems: Virtual constraints approach," *IEEE Trans. Automat. Contr.*, vol. 50, no. 8, pp. 1164–1176, 2005.

[54] C. C. de Wit, B. Espiau, and U. C, "Orbital stabilization of underactuated mechanical systems," Barcelona, Spain.

[55] A. S. Shiriaev, L. B. Freidovich, and S. V. Gusev, "Transverse linearization for controlled mechanical systems with several passive degrees of freedom," *IEEE Trans. Automat. Contr.*, vol. 55, no. 4, pp. 893–906, 2010.

[56] A. S. Shiriaev, L. B. Freidovich, A. Robertsson, R. Johansson, and A. Sandberg, "Virtual-holonomic-constraints-based design of stable oscillations of Furuta pendulum: Theory and experiments," *IEEE Trans. Robotics*, vol. 23, no. 4, pp. 827–832, 2007.

[57] V. Cerone, D. Andreo, M. Larsson, and D. Regruto, "Stabilization of a riderless bicycle: A linear-parameter-varying approach," *IEEE Control Syst. Mag.*, vol. 30, no. 5, pp. 23–32, 2010.

[58] H. K. Khalil, *Nonlinear Systems*, 3rd ed. Upper Saddle River, NJ: Prentice Hall, 2002.

[59] T. L. Burt, D. L. Porretta, and R. E. Klein, "Use of adapted bicycles on the learning of conventional cycling by children with mental retardation," *Edu. and Training in Develop. Disabilities*, vol. 42, no. 3, pp. 364–379, 2007.

[60] S. Lee and W. Ham, "Self-stabilzing strategy in tracking control of unmanned electric bicycle with mass balance," in *Proc. IEEE/RSJ Int. Conf. Intell. Robot. Syst.*, Lausanne, Switzerland, 2002, pp. 2200–2205.

[61] K. Chen, Y. Zhang, J. Yi, and T. Liu, "An integrated physical-learning model of physical human-robot interactions with application to pose estimation in bikebot riding," *Int. J. Robot. Res.*, vol. 35, no. 12, pp. 1459–1476, 2016.

[62] J. He and M. Zhao and S. Stasinopoulos, "Constant-velocity steering control design for unmanned bicycles," in *Proc. IEEE Int. Conf. Robot. Biomimet.*, Zhuhai, China, 2015, pp. 428–433.

[63] M. B. Aerts, W. F. Abdo, and B. R. Bloem, "The "bicycle sign" for atypical parkinsonism," *Lancet*, vol. 377, pp. 125–126, 2011.

[64] D. Limebeer and R. S. Sharp, "Bicycles, motorcycles, and models," *IEEE Control Syst. Mag.*, vol. 26, no. 5, pp. 34–61, 2006.

[65] A. D. Goodworth and R. J. Peterka, “Influence of stance width on frontal plane postural dynamics and coordination in human balance control,” *J. Neurophysiol.*, vol. 104, pp. 1103–1118, 2010.

[66] D. J. Reinkensmeyer and J. L. Patton, “Can robots help the learning of skilled actions?” *Exerc. Sport Sci. Rev.*, vol. 37, no. 1, pp. 43–51, 2008.

[67] J. Yi, D. Song, A. Levandowski, and S. Jayasuriya, “Trajectory tracking and balance stabilization control of autonomous motorcycles,” in *Proc. IEEE Int. Conf. Robot. Autom.*, Orlando, FL, 2006, pp. 2583–2589.

[68] S. Sastry, *Nonlinear Systems: Analysis, Stability, and Control*. New York, NY: Springer, 1999.

[69] P. Paoletti and L. Mahadevan, “Balancing on tightropes and slacklines,” *J. R. Soc. Interface*, vol. 9, 2012.

[70] T. Insperger and J. Milton, “Sensory uncertainty and stick balancing at the fingertip,” *Biol. Cybern*, vol. 108, 2014.

[71] J. T. Bingham and L. H. Ting, “Stability radius as a method for comparing the dynamics of neuromechanical systems,” *IEEE Trans. Biomed. Eng.*, vol. 21, no. 5, pp. 840–848, 2013.

[72] J. M. D. Hajdu and T. Insperger, “Extension of stability radius to neuromechanical systems with structured real perturbations,” *IEEE Trans. Biomed. Eng.*, vol. 24, no. 11, pp. 1235–1242, 2016.

[73] J. R. Chagdes, S. Rietdyk, J. M. Haddad, H. N. Zelaznik, and A. Raman, “Dynamic stability of a human standing on a balance board,” *J. Biomech.*, vol. 46, pp. 2593–2602, 2013.

[74] M. Stamelou, M. Kojovic, M. J. Edwards, and K. P. Bhatia, “Ability to cycle despite severe freezing of gait in atypical Parkinsonism in Fahr’s syndrome,” *Mov. Disord.*, vol. 26, no. 11, pp. 2141–2142, 2011.

[75] J. Meijaard, J. Papadopoulos, A. Ruina, and A. Schwab, “Linearized dynamics equations for the balance and steer of a bicycle: A benchmark and review,” *Proc. Royal Soc. A*, vol. 463, pp. 1955–1982, 2007.

[76] J. Moore and M. Hubbard, “Parametric study of bicycle stability (P207),” in *The Engineering of Sport 7*, M. Estivalet and P. Brisson, Eds. Springer-Verlag, 2008, vol. 2, pp. 311–318.

[77] J. Kooijman, J. Merjaard, J. Papadopoulos, A. Ruina, and A. Schwab, “A bicycle can be self-stable without gyroscopic or caster effects,” *Science*, vol. 322, pp. 339–342, 2011.

[78] J. Kooijman and A. Schwab, "A review on bicycle and motorcycle rider control with a perspective on handling qualities," *Veh. Syst. Dyn.*, vol. 51, no. 11, pp. 1722–1764, 2013.

[79] A. D. Goodworth and R. J. Peterka, "Contribution of sensorimotor integration to spinal stabilization in humans," *J. Neurophysiol.*, vol. 102, pp. 496–512, 2009.

[80] R. A. Hess, "Simplified approach for modelling pilot pursuit control behaviour in multi-loop flight control tasks," *Proc. IMechE Part G: J. Aero. Eng.*, vol. 220, no. G2, pp. 85–102, 2006.

[81] R. A. Hess, J. K. Moore, and M. Hubbard, "Modeling the manually controlled bicycle," *IEEE Trans. Syst., Man, Cybern. A*, vol. 42, no. 3, pp. 545–557, 2012.

[82] J. K. Moore, "Human control of a bicycle," Ph.D. dissertation, Dept. Mech. Aero. Eng., Univ. Calif. Davis, Davis, CA, 2012.

[83] S. M. Cain, "Human control of a bicycle," Ph.D. dissertation, Dept. Biomed. Eng., Univ. Michigan, Ann Arbor, MI, 2013.

[84] Y. Zhang, F. Liu, M. Trkov, and J. Yi, "Rider/bicycle pose estimation with integrated IMU/seat force sensor measurements," in *Proc. IEEE/ASME Int. Conf. Adv. Intelli. Mechatronics*, Kaohsiung, Taiwan, 2012, pp. 604–609.

[85] R. Sipahi and N. Olgac, "Complete stability robustness of third-order LTI multiple time-delay systems," *Automatica*, vol. 41, no. 8, pp. 1413–1422, 2005.

[86] K. Gu, S. I. Niculescu, and J. Chen, "On stability crossing curves for general systems with two delays," *J. Math. Analy. App.*, vol. 311, no. 1, pp. 231–253, 2005.

[87] R. Sipahi and I. I. Delice, "Advanced clustering with frequency sweeping methodology for the stability analysis of multiple time-delay systems," *IEEE Trans. Automat. Contr*, vol. 56, no. 2, pp. 467–472, 2011.

[88] R. Sipahi, S. Niculescu, C. Abdallah, W. Michiels, and K. Gu, "Stability and stabilization of systems with time delay," *IEEE Control Syst. Mag.*, vol. 31, no. 1, pp. 38–65, 2011.

[89] Q. Gao and N. Olgac, "Stability analysis for LTI systems with multiple time delays using the bounds of its imaginary spectra," *Syst. Contr. Lett.*, vol. 102, 2017.

[90] T. Vyhlidal and P. Zitek, "Quasipolynomial mapping based rootfinder for analysis of time delay systems," *IFAC Proc.*, vol. 36, no. 19, pp. 227–232, 2003.

[91] http://www.cak.fs.cvut.cz/algorithms/qpmr.

[92] Y. Zhang, K. Chen, and J. Yi, "Rider trunk and bicycle pose estimation with fusion of force/inertial sensors," *IEEE Trans. Biomed. Eng.*, vol. 60, no. 9, pp. 2541–2551, 2013.

[93] A. van Lunteren and H. G. Stassen, “On the influence of drugs on the behavior of a bicycle rider,” in *Proc. 6th Ann. Conf. Manual Control*, Wright-Patterson AFB, OH, 1970, pp. 419–437.

[94] C. Yang, G. Ganesh, S. Haddadin, S. Parusel, A. Albu-Schäeffer, and E. Burdet, “Human-like adaptation of force and impedance in stable and unstable interactions,” *IEEE Trans. Robotics*, vol. 27, no. 5, pp. 918–930, 2011.

[95] S. Ikemoto, H. B. Amor, T. Minato, B. Jung, and H. Ishiguro, “Physical human-robot ineraction: Mutual learning and adaptation,” *IEEE Robot. Automat. Mag.*, vol. 19, no. 4, pp. 24–35, 2012.